

University of South Dakota

USD RED

Dissertations and Theses

Theses, Dissertations, and Student Projects

2022

DEVELOPMENT AND CHARACTERIZATION OF GERMANIUM DETECTORS FOR SEARCHING RARE-EVENT PHYSICS

Rajendra Panth

Follow this and additional works at: <https://red.library.usd.edu/diss-thesis>



Part of the [Condensed Matter Physics Commons](#), [Nuclear Commons](#), and the [Other Physics Commons](#)

DEVELOPMENT AND CHARACTERIZATION OF GERMANIUM
DETECTORS FOR SEARCHING RARE-EVENT PHYSICS

By

Rajendra Panth

M.S., The University of South Dakota, 2019

A Dissertation Submitted in Partial Fulfillment of
the Requirements for the Degree of
Doctor of Philosophy

Department of Physics

Physics Program
In the Graduate School
The University of South Dakota
August 2022

Copyright by
RAJENDRA PANTH
2022
All Rights Reserved

The members of the Committee appointed to examine
the Dissertation of Rajendra Panth
find it satisfactory and recommend that it be accepted.

DocuSigned by:
Mei, Dongming
31A24A6D89824AD...

Chairperson

DocuSigned by:
Ji
D7C37880D26F476...

DocuSigned by:
Wengjin Xu
7D92DFABC72045A...

DocuSigned by:
Andrew Sykes
44F978C51100490...

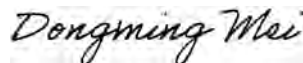
DocuSigned by:
Jürgen Reichenbacher
3F1D000494E7472...

ABSTRACT

High-purity germanium (HPGe) detector has an excellent energy resolution and low energy detection threshold ideal for searching rare-event physics such as dark matter and neutrinoless double beta decay searches. Understanding the electrical contact properties and the Ge detector properties is key to enhancing the use of Ge detectors for a wide range of applications. Amorphous Ge (a-Ge) is one of the passivation materials used to passivate Ge detectors, which also provides the barrier height to the charge injection. Several a-Ge contact Ge detectors were fabricated and tested at the University of South Dakota (USD) and Max-Planck-Institut (MPI) für Physik in Munich in a different setup. It was also found that a-Ge contacts can survive multiple thermal cycling without any sign of deterioration in the detector performance when directly immersed in cryogenic liquids.

The Gaussian distribution model developed by Werner and Guttler is used to characterize the inhomogeneity of the interface made by a-Ge and crystalline Ge. The inhomogeneity leads to the fluctuation in the barrier height with respect to the temperature. Further work is done on characterizing the Ge detector at the temperature range $\sim 5 - 80$ K. It was found that the free charge carriers in a Ge detector remain constant on average for the temperature range 11 - 80 K, further lowering the temperature below 11 K, impurities in the Ge start to freeze-out and the detector behaves like an ideal capacitor at less than ~ 6.4 K. It was also found that the holes (electrons) in p-type (n-type) Ge are more severely trapped than the electrons (holes) in p-type (n-type) Ge detector at around liquid helium temperature.

Dissertation Advisor



Dongming Mei

Acknowledgements

It was a great experience working under the mentorship and assistance of my supervisor, Dr. Mei. I would like to thank him for his constant guidance and feedback throughout my research years. I also thank him for giving me opportunities to participate in many conferences including PIRE-GEMADARC and APS conferences, each of them helped me expand my knowledge and motivated me in my scientific pursuits.

I thank all the members of our USD group who have supported me throughout my research years. I also thank Dr. Jing Liu for his constant guidance and motivation throughout my graduate research. It was an excellent opportunity to work with him who helped me understand physics and the techniques of detector fabrication and characterization.

I thank Dr. Sagar Sharma Poudel who has been an inspiration to me. I have had numerous physics discussions with him over the years. I am grateful to Dr. Wenzhao Wei, Dr. Xinughia Meng, Dr. Gang Yang, and Mitch Wagner for their guidance on the fabrication and characterization of the germanium detector. I would like to thank Kyler Kooi, with whom I worked together on the establishment of the Pulse Tube Refrigerator and characterizing the Ge detector in it. I would also like to thank Tupendra Oli, Laxman Sharma Poudel, Pramod Acharya, Bhubnesh Lama, Mathbar Singh Raut, Sanjay Bhattarai, Dr. Sudip Poudel, Dr. Ashok Tiwari, Dr. Pramod Dhungana, Ganesh Sigdel, Thakur Bhatta, and Dr. Hao Mei for their constant support and motivation.

I would also like to thank all the faculty members and staff of the Physics department at USD. Special thanks to my dissertation committee. I have received a lot of feedback from them which has been very valuable throughout my research.

No words are enough to express my indebtedness and gratitude to my family: my father and

mother, brothers, and sister-in-law. I thank my wife for her love and support and my little daughter, Samanta, whose addition to our family has brought a lot of happiness.

I dedicate this dissertation to my late mother, Menakala Panth, her unconditional love I remain forever indebted. She has been a constant source of inspiration in my life and remains so in my memories.

Table of Contents

Committee Signature page	i
Abstract	ii
Acknowledgements	iii
Table of Contents	v
List of Tables	ix
List of Figures	x
1 Introduction	1
1.1 Properties of Ge and its applications	1
1.2 The Fermi Level and Energy Band Gap of Ge	2
1.3 Overview of Contacts Formation on a Ge Detector	4
1.4 Applications of Ge Detectors	6
1.4.1 Gamma-ray Spectroscopy	7
1.4.2 Medical Imaging	7
1.4.3 Nuclear Security and Environmental Safety	8
1.4.4 Rare-event Searches	8
1.5 Limitations of HPGe detector	9
2 Rare-event Searches Using Germanium Detector Technologies	10
2.1 Neutrino Oscillation and Neutrinoless Double Beta Decay	11
2.1.1 Neutrinoless Double Beta Decay Searches Using Ge Detector Technologies . .	13
2.2 Dark Matter	16

2.2.1	WIMP Detection Principle	17
3	Germanium Detector Fabrication with Amorphous Germanium Contacts	22
3.1	HPGe Single Crystal	22
3.1.1	Zone Refining	23
3.1.2	Crystal Growth	23
3.1.3	Crystal Characterization	24
3.2	Ge Detector Fabrication and Challenges	26
3.2.1	Mechanical Processing	26
3.2.2	Chemical Processing	28
3.2.3	Contact Formation	29
3.2.4	Contact Geometries	32
3.3	Conclusions	35
4	Characterization of Germanium Detector in Cryogenic Liquids	38
4.1	Detector Characterization in a Vacuum Cryostat at 77 K	38
4.1.1	Detector Characterization Setup at USD	38
4.1.2	Electrical Characterization	40
4.1.3	Spectroscopy Measurements	43
4.2	Characterization of a-Ge Contacts Ge Detector Directly Immersed in Cryogenic Liquids	45
4.2.1	Detector Characterization Setup at MPI	46
4.2.2	Detector Operation in Liquid Nitrogen	49
4.2.3	Detector Operation in Liquid Argon	52
4.2.4	Characterization in Vacuum Again	54
4.3	Cross Comparison	55
4.3.1	Different Detectors in Same Environment	55
4.3.2	Same Detector in Different Environments	56
4.4	Detector Characterization at Liquid Helium Temperature	60

4.4.1	Detector Characterization Setup for Liquid Helium Temperature	60
4.4.2	I-V Characteristics	61
4.4.3	C-V Characteristics	62
4.4.4	Energy Spectroscopy	63
4.5	Conclusion and Outlook	63
5	Charge Barrier Height of Amorphous Germanium Contacts	66
5.1	Introduction	67
5.2	Experimental Methods	67
5.3	Charge Blocking Contacts	68
5.4	I-V-T Characteristics	69
5.4.1	Barrier Height Calculation	71
5.4.2	Barrier Inhomogeneity	73
5.4.3	The Relation Between the Inhomogeneity of Interface and CBH	77
5.5	Conclusions	79
6	Charge Trapping in Germanium Detectors	81
6.1	Charge Carrier Transport in Ge Detector	81
6.1.1	Electric Field Calculation in a Planar Detector	81
6.1.2	Schokley-Ramo Theorem	83
6.1.3	Charge Collection Efficiency	84
6.2	Charge Trapping and Capture in a Ge Detector at LHe Temperature	86
6.2.1	Impurities Freeze-out Phenomena	86
6.2.2	Cluster-dipole Formation	88
6.2.3	Spectral Analysis	90
6.2.4	Trapping Length of the Charge Carriers	94
6.2.5	Impact Ionization in Ge at Low-temperature	97
6.3	Charge Carrier Capture Cross-Section	99

6.4 Conclusions	101
7 Summary and Perspectives	103
Bibliography	106

List of Tables

1.1	Shown are selected semiconductor crystals that have potential applications for rare-event searches. The band gaps shown are for 300 K.	4
4.1	Shown is the summary of USD detector properties used for the characterization in MPI setup.	47
4.2	Shown is the set temperature and actual temperature of the crystal.	62
5.1	Barrier height extrapolated from a linear fit of $\psi_{0,b}$ versus temperature.	76
5.2	Summary of three USD detector properties used for the study of inhomogeneity of the interface.	79
6.1	Shown are the properties of three detectors used for the study of charge trapping and C-V characteristics.	92

List of Figures

1.1	Shown is the Fermi function as a function of electron energy at various temperatures. 0 eV, 0.35 eV, and 0.7 eV denote the valence band, intrinsic Fermi level, and conduction band of the Ge, respectively.	3
2.1	Shown is the Feynman diagram of the nuclear decay process. Left: two neutrino double beta decay; Right: neutrinoless double beta decay.	12
2.2	Shown is the comparison between a normal and a thin-contact PPC HPGe detector (not to scale).	14
2.3	Shown is the spin-independent interaction limit as a function of WIMP mass set by various experiments. The black line represents the 90 % confidence limit, green and yellow bands represent the 1 σ and 2 σ sensitivity bands respectively for the LUX-ZEPLIN (LZ) experiment. The figure is taken from [113].	20
2.4	Left: shown are the detector materials used or under consideration for detecting sub-GeV dark matter. A solid line represents that the detector is currently in use for that mass sensitivity range. A long-dashed line represent the detector shown under consideration for the near term and a short-dashed line under consideration for the long term. The mass-sensitivity range is shown on the horizontal axis [114]; Right: shown is the relative event rate as a function of recoil energy for light dark matter searches [35].	20
3.1	Left: shown is the schematic of the zone-refining process. Heater, molten zone, and impurities move from left to right through the solid charge during the zone refining process. The segregation of impurities occurs in the molten zone; Right: single crystal growth of Ge by the Czochralski process (taken from Hao Mei's thesis). . . .	24
3.2	Shown is the setup for cutting and grinding the crystal to turn it into the desired geometry.	28
3.3	Shown is the germanium crystal that has gone through different process. Left: crystal after mechanical lapping; Middle: crystal after long-term chemical etching; Right: crystal loaded on the jigs with Al mask after short term chemical etching.	29

3.4	Shown are the equipments used to carry out the contact formation on the high-purity germanium crystal. Left: Perkin Elmer (2400 model) Sputtering machine at USD used for the a-Ge and Al deposition; Right: Electron-Beam machine at USD used for the Al deposition on top of a-Ge contacts.	30
3.5	Shown in the contact formation process for a planar detector geometry. Left: acid resistant tape placed on top and bottom surface of the detector; Middle: schematic representation of a Ge detector with a planar structure (not to scale); Right: a planar Ge detector fabricated at USD.	33
3.6	Shown is the guard-ring structure formed on a planar geometry detector. Left: acid resistant tape placed on top and bottom surfaces of the detector, Middle: schematic representation of a Ge detector with a guard-ring structure (not to scale); Right: a guard-ring Ge detector fabricated at USD.	34
3.7	Shown is the contact formation process for a point-contact detector. Left: acid resistant tape placed on bottom and side surfaces, and xylene and piscine mixture to make a point contact; Middle: schematic representation of a point-contact detector (not to scale); Right: a p-type point contact Ge detector fabricated at USD.	35
3.8	Left: comparison between a normal and a thin-contact PPC germanium detector (not to scale); Right: inverted-coaxial germanium detector (not to scale).	36
4.1	Shown is the detector characterization setup at USD. Left: internal structure of vacuum cryostat; Right: schematic representation of electronic circuit for detector characterization.	39
4.2	Shown is the electrical characterization plots obtained at 77 K. Left: the plot of leakage current versus bias voltage for the USD-R03 detector at different temperatures; Right: relative capacitance as a function of bias voltage for three detectors. All three detectors has different net impurity concentrations and thickness.	41
4.3	Shown is the measured detector capacitance for a USD-RL detector as a function of bias voltage. Absolute capacitance of the detector was measured at 1000 V and then the relative capacitance data was normalized to obtain the absolute capacitance for the lower bias voltages.	44
4.4	Shown are the energy spectra obtained for a USD-R08 detector. Top and bottom spectra are obtained from ^{137}Cs and ^{241}Am source, respectively. Both the sources were placed outside of the LBNL cryostat. Pulser determines the electronic noise level.	46
4.5	Left: technical drawing of the MPI cryostat; Middle: schematics of its internal wiring; Right: schematics of electronic circuit for the detector characterization.	48
4.6	Left: detector to be lowered into the MPI cryostat; Right: two different contact schemes of the guard-ring detector USD-R02 in the MPI cryostat.	48

4.7	Shown is the leakage current of detector USD-RL as a function of its bias voltage in LN ₂ , except for the “Before” and “After” data sets, which were measured in vacuum at USD before and after the MPI deployment, respectively. The numbers denote thermal cycles in LN ₂	49
4.8	Shown is the leakage current of detector USD-8-4-15 as a function of its bias voltage in various environments. The numbers in the legend denote thermal cycles in LN ₂ . The scale for the first cycle in LN ₂ and the LAr measurement is on the right.	51
4.9	Leakage currents of detector USD-R02 versus its bias voltage in LN ₂ , except for the data sets marked with “before” and ”after”, which were measured in the vacuum cryostat at USD before and after the MPI deployment. The bulk leakage currents were measured through the central contact. The surface leakage currents were measured through the guard contact.	51
4.10	Energy spectra of ¹³⁷ Cs taken in LN ₂ . No spectrum was taken with USD-R02 since the source was temporarily unavailable for the measurement.	52
4.11	Leakage currents of detector USD-RL versus its bias voltage in LAr. The numbers denote individual thermal cycles. Also plotted are the highest leakage current measured with the same detector in LN ₂ and the one measured in the vacuum cryostat at USD after its deployment at MPI.	53
4.12	Leakage currents of detector USD-R02 versus its bias voltages in LAr, except for the ones labeled “before” and “after”, which were measured in the USD vacuum cryostat at 90 K. The numbers denote the thermal cycles in LAr. Bulk leakage currents were measured through the central contact, surface ones were through the guard contact.	54
4.13	Energy spectra of ¹³⁷ Cs taken in LAr.	55
4.14	Energy spectra obtained with the LBNL vacuum cryostat and a ¹³⁷ Cs source outside of the cryostat. Pulser determines the electronic noise level.	56
4.15	Highest leakage currents of the three detectors measured in LN ₂	57
4.16	Highest leakage currents of the three detectors measured in LAr.	57
4.17	Largest leakage currents of detector USD-R02 in various environments through its central contact.	58
4.18	Energy spectra taken with detector USD-8-4-15 in various environments.	59
4.19	Shown is the experimental setup for detector characterization at LHe temperature. Left: Enclosed PTR; Middle: detector enclosed with the radiation shield; Right: detector loaded inside the cryostat and ²⁴¹ Am source into the PTFE bar.	61

4.20	Shown is the energy spectra obtained for a USD-R09-02 detector. Top and bottom spectra were obtained from ^{241}Am source in a LBNL and PTR, respectively. ^{241}Am source was placed inside the cryostat on both setups. FWHM of pulser in each setup determines the electronic noise level of that setup.	64
5.1	Left: schematic representation showing the depletion direction, charge injection in a p-type germanium detector with positive bias voltage applied on the bottom electrode of the detector; Right: shown is the variation of logarithmic of bulk leakage current density versus the applied bias voltage for USD-R03 detector at 90 K and 95 K.	69
5.2	Shown is the plot of logarithmic of BLC density as a function of its bias voltage for a USD-R03 detector at 90 K and 95 K. Left: shown is the plot for $V_a < V_d$; Right: shown is the plot for $V_a > V_d$	72
5.3	Shown is the schematic representation of energy band diagram for a p-type germanium detector. The Fermi level in the amorphous germanium lies in middle of the conduction and valence band. A small negative bias is applied to the bottom contact of the detector, hence the detector starts to deplete from its top surface [24]. (not to scale)	75
5.4	Left: the variation of the current density versus the square root of bias voltage for USD-R03 detector at 90 K. The plot shows that there are two distinguishable regions, which correspond to two different ranges of the applied bias voltage, 10- 20 volts and 30-70 volts; Right: shown is the variation of the leakage current density versus the square root of bias voltage for USD-R03 detector at different temperatures.	75
5.5	Left: shown is the variation of the $\psi_{0,b}$ versus temperature. The CBH at 0 K was extracted from the first-order polynomial fit; Right: shown is the variation of $\psi_{0,b}$ with respect to $1/2kT$	78
6.1	Shown is the electric field distribution in two detectors, USD-RL and USD-R09-02. The V_d for these detectors is 400 V and 1200 V, respectively.	83
6.2	Left: shown is a schematic diagram of the charge drifting process in a planar detector. A positive bias voltage is applied from the bottom electrode of the detector and top contact is grounded. Interaction shown here represents the interaction point that occurs somewhere middle of the detector and charge carriers are drifted towards the oppositely biased electrode; Right: shown is the plot of Onsager radius as a function of temperature.	85
6.3	Shown is the C-V characteristics obtained for a USD-R11 detector at various temperatures. The V_d of this detector is 500 V. It has a $ N_A - N_D $ of $5.81 \times 10^{10} / \text{cm}^3$ and a thickness of 3.9 mm.	87

6.4	The schematic representation of the excited states of the dipole and cluster dipole formation in a p-type and n-type impurity atom in a Ge crystal. This process comes into play at temperatures below ~ 11 K. \vec{p} and \vec{q} represent the corresponding dipole moments [156].	89
6.5	Shown is the energy deposited from the 5.3 MeV α s in an n-type detector, R09-02. The plots shown on the left and right are for the detector operated at 5.2 K and 77.8 K respectively. The top plot on both sides was taken when negative bias was applied at the bottom surface whereas the bottom plots on both sides were taken when positive bias was applied at the bottom surface.	93
6.6	Shown is the energy deposited from the 5.3 MeV α s in a p-type detector, RL. The plots shown on the left and right are for the detector operated at 5.2 K and 77.8 K, respectively. The top plot on both sides was taken when negative bias was applied at the bottom surface whereas the bottom plots on both sides were taken when positive bias was applied at the bottom surface.	94
6.7	Shown is the normalized charge collection efficiency (CCE) as a function of bias voltage at temperatures 5.2 K and 77.8 K using an alpha source. Left: normalized CCE for a n-type detector; Right: normalized CCE for a p-type detector.	94
6.8	Shown is the energy deposited from the 661.7 keV γ -rays in a n-type detector, R09-02. Plots shown on the left and right are for the detector operated at 5.2 K and 77.8 K respectively. The top plot on both sides were taken when negative bias was applied at the bottom surface whereas the bottom plots on both sides were taken when positive bias was applied at the bottom surface.	95
6.9	Shown is the energy deposited from the 661.7 keV γ -rays in a p-type detector, RL. The plots shown on the left and right are for the detector operated at 5.2 K and 77.8 K respectively. The top plots on both sides was taken when negative bias was applied at the bottom surface whereas the bottom plots on both sides was taken when positive bias was applied at the bottom surface.	95
6.10	Shown is the normalized charge collection efficiency (CCE) as a function of bias voltage using a gamma source at temperatures 5.2 K and 77.8 K. Left: normalized CCE for a n-type detector; Right: normalized CCE for a p-type detector.	96
6.11	Left: shown is the relation between charge collection efficiency and trapping length of charge carriers for two detectors. The detector thickness of R09-02 and RL detector is 1.07 cm and 0.55 cm respectively; Right: shown is the plot of charge collection efficiency as a function of interaction position of γ . The trapping length for this plot was obtained from the alpha data.	97
6.12	Left: time-dependent charge collection efficiency for a R09-02 detector at 5.2 K as a function of bias voltage; Right: time-dependent charge collection efficiency for a R09-02 detector at positive 300 V as a function of temperature.	98

- 6.13 Shown is the time-dependent charge collection efficiency for a R09-02 detector. Left: positive 30 V at 7.6 K; Right: positive 300 V at 5.2 K 99
- 6.14 Left: shown is the mean scattering length as a function of electric field; Right: shown is the effective charge carrier capture cross-section as a function of electric field. . . . 102

1

Introduction

This chapter gives an overview of the Germanium (Ge) material properties, a historical overview of contact formation on high-purity germanium (HPGe) detectors, and the working principle of Ge radiation detectors. Lastly, the applications of Ge-based radiation detectors and our motivation for exploring Ge detector properties for a wide range of temperatures are discussed.

1.1 Properties of Ge and its applications

Ge is a semiconductor material having an atomic number (Z) 32, and a band gap (0.67 eV at room temperature). Its density at room temperature is 5.323 gm/cm³. The melting point of Ge is 938.2 °C. Ge has 5 stable isotopes: ⁷⁰Ge (20.5%), ⁷²Ge (27.4%), ⁷³Ge(7.8%), ⁷⁴Ge (36.5%) and ⁷⁶Ge (7.8%) [1]. HPGe single crystals of impurity concentration less than 10¹⁰ atoms/cm³ are available after the zone-refining [2] and crystal growing process [3–5]. The major p-type impurities in a Ge are boron (B), aluminum (Al), and gallium (Ga) whereas the major n-type impurities are nitrogen (N), phosphorous (P), arsenic (As), antimony (Sb), and tin (Sn) [2]. Some promising features (primarily low band gap, high atomic number, and high refractive index) and relatively easy availability in the form of an alloy make Ge enticing in solid-state electronics, semiconductors, fiber optical systems, etc [6]. The enrichment of Ge isotopes provide a unique opportunity to study rare event physics. ⁷⁶Ge is present in the isotopic abundance of $\sim 7.8\%$, which is a candidate isotope

for much-sought neutrinoless double beta ($0\nu\beta\beta$) decays. With ^{76}Ge -enriched Ge, it is possible to enhance the probability and increase the sensitivity of ^{76}Ge -based $0\nu\beta\beta$ decay searches.

1.2 The Fermi Level and Energy Band Gap of Ge

Elementary particles in the standard model (SM) are primarily of two kinds: Fermions and Bosons. Electron, muon, tauon, and their associated neutrinos are in the fermionic group, whereas, quarks, gluons, photon, Z, W, and Higgs boson are in the bosonic group. Electrons being in a fermionic group obeys the Pauli exclusion principle which states that no two fermions can occupy the same quantum states [7]. The occupancy of quantum states is described by the Fermi-Dirac statistics. The Fermi energy is the maximum kinetic energy that an electron can possess at 0 K. The energy of the highest filled state corresponding to the energy of electrons at absolute zero temperature is called the Fermi level. The Fermi energy (μ) of Ge lies in the middle of conduction and the valence band for an intrinsic Ge. For a doped crystal the Fermi level shifts toward the conduction band or valence band depending on the dopant and other impurities. The Fermi function is a probability distribution function that depends on the temperature (T), the energy of the electron (E), and the intrinsic Fermi energy level (E_f). The Fermi function can be used in equilibrium conditions to find the probability of an electron can occupying the given energy state (E) as;

$$f = \frac{1}{e^{\frac{(E-E_f)}{k_B T}} + 1} \quad (1.1)$$

The plot shown in Figure 1.1 shows the probability distribution of electrons at various temperatures. At temperatures above absolute zero, there is a finite probability that a certain number of electrons can occupy states above the Fermi level as shown in Figure 1.1. The Fermi level is particularly important in understanding the thermal and electrical properties of the material. The implication of the Fermi function is discussed in later chapters.

An energy band gap is the measure of spacing between the lowest band of the valence band and the highest point of the conduction band. For semiconductors, there exists a small forbidden gap between those bands. A forbidden band gap is characterized as the region where no wavelike electron

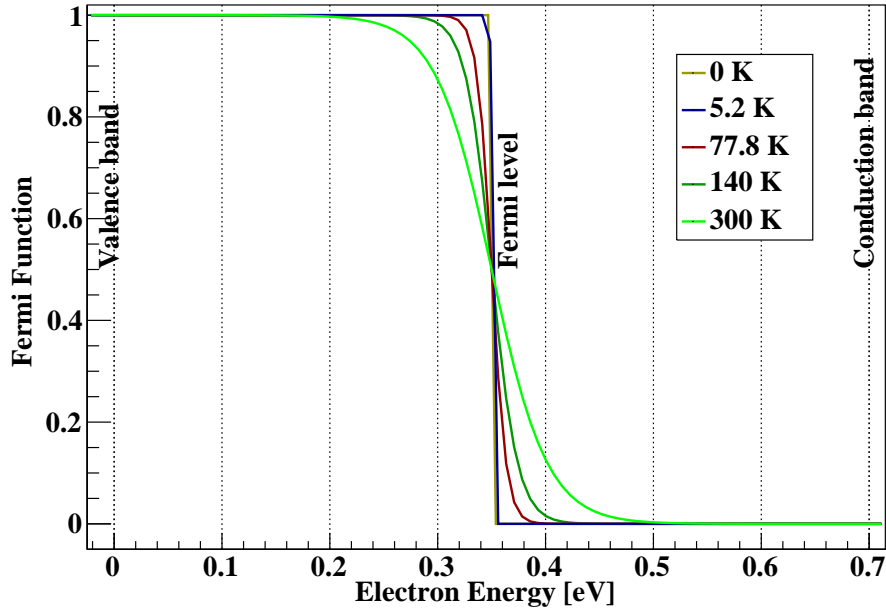


FIGURE 1.1: Shown is the Fermi function as a function of electron energy at various temperatures. 0 eV, 0.35 eV, and 0.7 eV denote the valence band, intrinsic Fermi level, and conduction band of the Ge, respectively.

orbitals exist. If the electrons in the valence band and below the Fermi level get a small amount of kinetic energy then some of the electrons can move to the conduction band. For temperature other than absolute zero there is a probability of excitation of electrons from the valence band to the conduction band due to thermal energy. The number of electrons that can reach the conduction band depends on the Fermi function and the electron density of states. Since Ge has a small band gap, conduction is possible at room temperature without supplying external energy. Table 1.1 summarizes the several semiconductor crystal properties at 300 K which provides some unique properties to crystal semiconductors [8]. Thermal energy at room temperature is sufficient to excite some electrons from the valence band to the conduction band. As a result, the operation of Ge as a radiation detector at room temperature is limited by the presence of large thermal noise. The silicon (Si) crystal has a relatively higher band gap than Ge, which makes it possible for the Si detector to operate at room temperature. A small band gap has also several advantages. Importantly, a relatively large number of charge carriers can be generated with the same energy deposition in the crystal as that of the crystal with a wide band gap. Primarily, the atomic number

Table 1.1: Shown are selected semiconductor crystals that have potential applications for rare-event searches. The band gaps shown are for 300 K.

Crystal	Atomic number (Z)	Density ($\frac{gm}{cm^3}$)	Dielectric constant (ϵ)	Band gap (eV)
Ge	32	5.32	16.2	0.66
Si	14	2.32	11.7	1.12
InSb	49+51	5.77	16.8	0.17
GaSb	31+51	5.61	15.7	0.726
GaAs	31+33	5.32	12.9	1.424
GaP	31+15	4.14	11.1	2.26
InAs	49+33	5.68	15.15	0.354
InP	49+15	4.81	12.5	1.344

(Z), density, and energy band gap of the semiconductor material determine the choice of a detector material for a given purpose. However, there may be a trade-off in the choices of semiconductor material. This will be discussed in later chapters.

1.3 Overview of Contacts Formation on a Ge Detector

Contact formation on the crystal is an important step in the detector fabrication process. For over 60 years, Ge-based detectors are used for radiation detection. The first use of lithium-drifted Ge detectors Ge(Li) was in the 1960's for the γ -spectroscopy [9, 10]. There was a limitation on the net impurity concentration ($|N_A - N_D|$) and the size of the crystal that was achievable. The purpose of Li-drifting was to produce a compensated detector so that the $|N_A - N_D|$ of the Ge detector is nearly zero and the detector could be fully depleted with a small bias voltage. The typical process for making Li-drifted detectors is as follows. First, Li is coated on one side of the Ge crystal, and then it is heated to diffuse the Li through the Ge. Li (donors) are then drifted using the appropriate bias voltage to fill the acceptors in the Ge crystal, canceling the p-type property of the crystal and giving rise to a nearly net-zero impurity concentration. This type of detector has several drawbacks. First, cooling down the detector during and following the detector fabrication is necessary for the operation, and also the storage of the Li-drifted detector at room temperature alters the compensated region of the detector. Second, the Li-drifting process is a slow process hence it takes a long time to entirely compensate the Ge crystal. Third, only p-type crystals can be

used since the Li acts as a donor. Li is good for blocking hole injection, however, to block electron injection another contact material is needed. In addition, the mobility of charge carriers is low and it increases the probability of charge carrier trapping during the movement of charge carriers to the electrodes.

The development of HPGe crystals in the 1970's gave new possibilities for detector fabrication [11]. Further refinement in the crystal growth process came from growing Ge crystals using Czochralski pullers after the purification of raw materials using the zone refining technique. Currently, large size (~ 10 inch diameter) Ge single crystals can be grown as low as of $|N_A - N_D|$ of the order of $10^9 / \text{cm}^3$ [3]. These detectors have a few advantages over the traditional lithium-drifted detectors. First, both p-type and n-type detectors can be used. Second, it gives flexibility in choosing the contact material for making the contacts. Also, these detectors demonstrate better energy resolution. There are several ways to make p^+ contacts on a Li-diffused Ge detector. The typical process for contact formation is described as follows. n^+ contacts are formed by Li diffusion and p^+ contacts by boron ion implantation. The use of n^+ contact is to block the hole injection whereas p^+ contact is to block the electron injection. Some of the drawbacks of these contacts are: These contacts are not stable at room temperatures due to the high diffusion of Li in the Ge detector. Further, partial charge collection from the transient layer between Li and Ge surface takes place. In addition, Li-diffusion creates dead layers which are insensitive to charge carriers. Also, the active volume of the detector is less than the crystal size. Thin n^+ contacts can also be made using phosphorus ion implantation [12]. However, the fabrication process is complicated for these types of contacts and cannot withstand high electric fields. The process for the Li diffusion and boron ion implantation is described as follows: Initially, dopant material (Li) is coated on the surface of the crystal. At high temperatures, Li atoms are made to diffuse into the crystal. The diffusion is from the high-concentration region to the low-concentration region. Boron ion implantation does not require very high temperatures as in the diffusion process. However, the implantation changes the physical, chemical, and electrical properties of the target. In ion implantation, an ion beam is bombarded into the semiconductor substrate, implanting dopants into the material. This process damages the substrate, thus requiring a post-implantation anneal.

An alternative way of contact formation is the use of amorphous Ge (a-Ge) which typically overcomes the drawbacks of traditional contacts. Grigorovici et al. reported the first experimental study of a-Ge contacts on crystalline Ge in 1964 [13]. England and Hammer investigated the charge blocking property of a-Ge contacts on silicon and Ge detectors in 1971 [14]. Later in 1977, Hansen and Hall investigated the bipolar blocking behavior of a-Ge contacts on HPGe detectors [15]. The results published by Hansen and Hall showed a large variation in leakage current. To overcome this instability, a-Ge contacts were produced using a radio-frequency (RF) sputtering system by Luke et al. in 1992 [16]. Advancement in the fabrication process has led to the enhancement of a-Ge passivated HPGe detectors that can be used in various applications. In addition, there are several advantages of a-Ge contact over traditional contacts. First, unlike Li-diffusion, there is a significant reduction of the dead layer on the Ge detector, and the active volume of the detector increases. Second, a-Ge contacts can block both electrons and holes. Bi-polar blocking behavior of a-Ge makes the formation of rectifying contacts much easier. Third, a-Ge contacts can be easily segmented. Segmented detectors are used as position-sensitive detectors. It eliminates the need of passivation between the contact elements which is required when using traditional contacts as studied by Luke [16–18] and Amman [19] in 1994 and 2000. Easy segmentation of a-Ge contacts is also the reason why the use of a-Ge coated Ge detector is favored in X-ray and gamma-ray imaging. Also, a-Ge coated Ge detectors are suitable for field shaping [20] and proximity electrode signal readout [21, 22]. Detailed analysis of the process parameters in the fabrication process is discussed in detail in recent papers by Looker and Amman [23–25]. Large size detectors are preferable for next-generation experiments searching for rare-event physics. The development of large-size crystal detectors requires extensive study of a-Ge contacts and Ge detector properties at a wide temperature range.

1.4 Applications of Ge Detectors

The ability to make a large-size single crystal of Ge [3, 4] adds to the potential applications of Ge-based detectors. High mobility of charge carriers in Ge and a large production of charge carriers during particle energy deposition results in good detection efficiency and excellent energy

resolution for particle detection. This makes the Ge detector superior to the other radiation detectors. Ge detectors have a wide range of applications. Ge detectors are extensively used for γ -ray spectroscopy [19, 24, 26–28], rare-event physics searches such as $0\nu\beta\beta$ decay [29–31] and dark matter [32–35], as well as astroparticle physics [36], medical imaging [37], environmental research [38] and nuclear security [39].

1.4.1 *Gamma-ray Spectroscopy*

Gamma-ray spectroscopy strives to detect gamma lines with an excellent resolution. For the detection of the γ -rays of energy higher than the 100 keV, NaI scintillation detectors, and semiconductors detectors are preferred. The energy resolution of scintillation detectors is $\sim 7\%$ full width half maximum (FWHM) [40], CdZnTe detectors is $\sim 1\text{-}2\%$ FWHM [41], Ge detectors is $\sim 0.2\%$ FWHM [42] for the 661.7 keV γ line of ^{137}Cs source. Ge is the preferred semiconductor detector for high-energy γ -ray spectroscopy. Bolometers detector technologies provide better energy resolution than the Ge detector, however, they cannot fulfill the large detector volume needed for large-scale experiments. The higher the atomic number of the detector material, the greater the cross-section for γ -rays interaction. A segmented Ge detector provides the position information of the γ -ray interaction which makes it possible to reconstruct the position coordinates of the particle interaction. γ -ray spectroscopy is also used to investigate the nuclear structure. GRETA (Gamma Ray Energy Tracking Array) [43], and AGATA (Advanced GAMMA Tracking Array) [44] are some of the experiments closely working on understanding the exotic behavior of excited nuclear states using a Ge detector array.

1.4.2 *Medical Imaging*

The mobility of charge carriers in Ge is relatively higher than other semiconductors allowing fast count rate capabilities for the x-ray imaging system. A detector capable of differentiating the interaction position is crucial for imaging devices. Some instances where Position-tracking becomes important are positron emission tomography (PET) and single-photon emission computed tomography (SPECT). Ge is also a good material choice to estimate the photon depth of interaction

and to correct the parallax error since the charge collection time is different between the opposite sides of the double striped detector [20]. It also allows for multi-isotope imaging since the energy resolution is better and cross-talk is minimum in a double-sided strip Ge detector [45]. Recent developments in mechanical cooling systems have further enhanced the scope of Ge detectors for biomedical imaging.

1.4.3 Nuclear Security and Environmental Safety

Ge detectors can be used for non-nuclear proliferation and security applications. These applications are often based on neutron and gamma-ray detection. The Multisensor Aerial Radiation Survey (MARS) detector array has been tested on transporting vehicles to screen and monitor the items [39]. The MARS detector has survived multiple thermal cycles and long-distance transportation. These detectors have been operated at high altitudes, one application is cosmic ray measurements as a function of the altitude. The high energy resolution of the HPGe detector makes it applicable for identifying radioactive materials. Other applications are in nuclear safety and nuclear power plant. A lot of work is ongoing in this field to design an array of detectors since the large size Ge crystals are limited.

HPGe detectors have applications in monitoring atmospheric radiations. They can also be used to test the radio purity of the material. For example, the presence of radioactive materials and radio levels in the air, soil, water, etc can be identified. Ge detector can detect radio-purity of the materials with concentrations down to 0.1–1 Bq/kg in solids and 0.1 Bq/L in water [46]. Particularly Ge detectors are of interest in this field since they have excellent energy and time resolution.

1.4.4 Rare-event Searches

A radiation detector with an excellent energy resolution and fine segmentation of contacts is preferred for rare-event searches. The atomic number and mass number of Ge crystal are ideal for the search for dark matter interactions. ^{76}Ge isotope undergoes a double beta decay and is a candidate isotope for $0\nu\beta\beta$ decay. The applications of the Ge detector for rare-event searches are discussed

in Chapter 2.

1.5 Limitations of HPGe detector

The discrimination between the signal and the noise becomes difficult when the Ge detector is operated at room temperature. Cooling for most experiments is through a continuous supply of cryogenic liquids, which limits the operation time and the location of the operation. Recent development in the cryo-cooling system doesn't limit the cooling by liquids and expands the uses of Ge detector for space exploration also [47]. Advancements in read-out detector technologies are necessary to address the shortcoming of spatial resolution, improvement in detector energy resolution, low threshold detector, etc. Several challenges exist in detector fabrication and its reproducibility. Like other semiconductor detectors, the performance of the Ge detector degrades over time from irradiation. Also, HPGe crystals are required for the detector fabrication, which requires zone refining of raw Ge ingots and single crystal growth of Ge which is time-consuming and expensive.

Thick contacts, such as Li-diffused contacts absorb the low-energy photons which limits the detection efficiency of the Ge detector for low-energy photons. Alternative to the thick contacts is the thin contacts such as a-Ge contacts. a-Ge contacts allow easy pass of low-energy signals and these contacts can be segmented easily. Entire passivation of the large-size Ge crystal with thin a-Ge contacts creates challenges for the handling since a small scratch can potentially deteriorate the performance of the detector. If the Ge detector can be fabricated with a combination of thick contacts and thin contacts, it increases the detection efficiency for low-energy photons. This work is focused on further analyzing the a-Ge contact properties at a wide temperature range. The Ge detector properties are understood very well at milliKelvin (mK) and around liquid nitrogen (LN₂) temperature but little is known around liquid helium (LHe) temperature. In addition to characterizing the a-Ge contacts, this work is based on characterizing the Ge detector properties at around LHe temperature using the Ge detectors fabricated from the home-grown crystals at the University of South Dakota (USD).

Rare-event Searches Using Germanium Detector Technologies

The Standard Model (SM) of particle physics is highly successful in explaining particle properties and is consistent with observations. The SM particles are primarily of two kinds: Fermions and Bosons. Quarks and leptons are fundamental Fermions in the SM. Bosons in the SM are the force carriers and mediators of interaction between particles. Despite the overwhelming success of the SM, there are still a few fundamental questions that may require physics beyond the SM. One is the origin of the neutrino's mass. Neutrino oscillation measurements have established that a given flavor of a lepton neutrino (say muon neutrino) can transform into an electron neutrino (say electron neutrino). This flavor oscillation demands that the neutrinos have some tiny mass. This observed behavior also raises the question of whether the neutrino is a Dirac or Majorana particle. Ge detectors that have been used in $0\nu\beta\beta$ beta decay searches as in the Large Enriched Germanium Experiment for Neutrinoless Double beta decay (LEGEND) [48] can help answer some of these questions. Further, experiments like Super Cryogenic Dark Matter Search (SuperCDMS) [49], China Dark Matter Experiment (CDEX) [50], Expérience pour DETecter Les WIMPs En Site Souterrain (EDELWEISS) [51], and CoGeNT [32] have also used Ge as a target material and detector in dark matter searches. This chapter will give a brief overview of the use of Ge detector technology in $0\nu\beta\beta$ decay and dark matter searches.

2.1 Neutrino Oscillation and Neutrinoless Double Beta Decay

Neutrinos are fermions that belong to the lepton family in the SM and they interact weakly through the exchange of W and Z bosons (W^+ , W^- , and Z^0). Neutrino and its anti-particle are assigned separate lepton numbers in the framework of the SM. Properties of neutrinos, especially neutrino oscillations, that are not directly predicted by the SM, indicate extension of the SM may be necessary. Neutrino oscillation is a flavor-change phenomenon where the neutrino changes its flavor (ν_e , ν_μ , ν_τ) across macroscopic distances. Neutrino oscillations indicate that neutrinos have non-zero mass and the mass eigenstates of neutrinos may not be the same as neutrino flavor eigenstates.

The Pontecorvo-Maki-Nakawaga-Sakata [PMNS] matrix, U , relates the flavor eigenstate to the mass eigenstate by [52];

$$\nu_\alpha = \sum_i U_{\alpha i} \nu_i \quad (2.1)$$

where $\alpha \in \{e, \mu, \tau\}$, and $i \in \{1, 2, 3\}$ denote the flavor eigenstates and mass eigenstates respectively.

The PMNS matrix in term of mixing angle and phases is given as,

$$U = \begin{bmatrix} c_{12}c_{13}e^{i\alpha_1/2} & s_{12}c_{13}e^{i\alpha_2/2} & s_{13}e^{i\delta} \\ (-s_{12}c_{23} - c_{12}s_{23}s_{13})e^{i\delta}e^{i\alpha_1/2} & (c_{12}c_{23} - s_{12}s_{23}s_{13}e^{i\delta})e^{i\alpha_2/2} & s_{23}c_{13} \\ (s_{12}s_{23} - c_{12}c_{23}s_{13}e^{i\delta})e^{i\alpha_1/2} & (-c_{12}s_{23} - s_{12}c_{23}s_{13}e^{i\delta})e^{i\alpha_2/2} & c_{23}c_{13} \end{bmatrix} \quad (2.2)$$

where $c_{ij} \equiv \cos\theta_{ij}$ and $s_{ij} \equiv \sin\theta_{ij}$. θ_{12} , θ_{13} and θ_{23} are the mixing angles. δ is a Dirac, α_1 , and α_2 are the Majorana CP-violation phases. Therefore, effective mass depends on seven out of a total of nine parameters in the neutrino mass matrix. Nuclear matrix elements are model dependent, and it creates uncertainty for the effective Majorana neutrino mass.

Neutrino oscillation experiments can provide the difference of the square of neutrino masses, however, the absolute magnitude of the masses is still unknown. This issue arises the case of three possible scenarios: the normal hierarchy ($m_1 < m_2 < m_3$), inverted hierarchy ($m_3 < m_1 < m_2$), and the degenerate case. The discovery of neutrino oscillations hints the physics to beyond the SM.

$2\nu\beta\beta$ decay process was first described by Maria Goeppert-Mayer in 1935 [53]. In this case, two neutrons are simultaneously converted into two protons, two electrons, and two anti-neutrinos. Ettore Majorana in 1937 proposed that neutral fermions could be their own anti-particle [54].

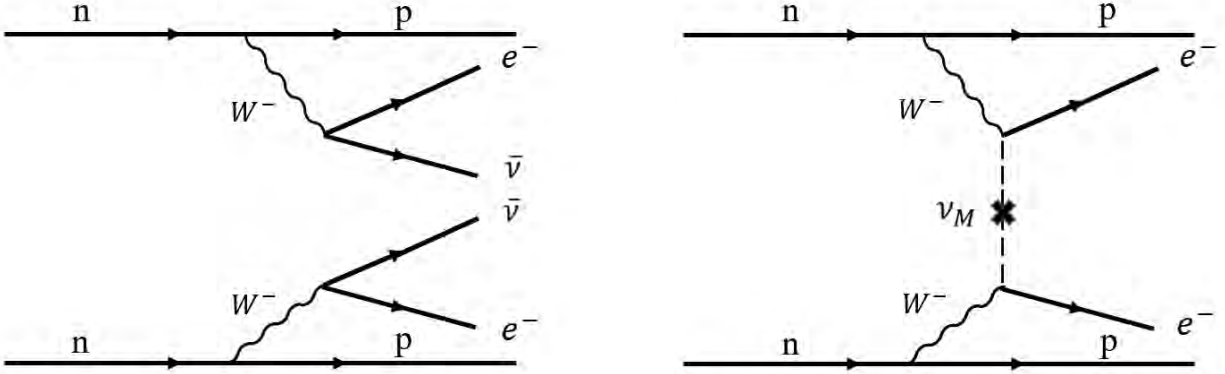


FIGURE 2.1: Shown is the Feynman diagram of the nuclear decay process. Left: two neutrino double beta decay; Right: neutrinoless double beta decay.

Later in 1939, Wendell H. Furry discussed the idea of $0\nu\beta\beta$ decay as a rare exotic nuclear decay in which an unstable nucleus decay with the emission of two electrons but without the emission of anti-neutrinos associated with them [55]. Neutrinos are Majorana particles if the neutrinos and anti-neutrinos cannot be distinguished.

There are two possibilities for double beta decay to occur [56].

$${}^A_Z X \rightarrow {}^A_{Z+2} Y + 2e^- + 2\nu^- \quad (2.3)$$

$${}^A_Z X \rightarrow {}^A_{Z+2} Y + 2e^- \quad (2.4)$$

The Feynman diagram of two neutrino double beta ($2\nu\beta\beta$) decay and $0\nu\beta\beta$ decay are shown in Figure 2.1. In $0\nu\beta\beta$ decay, a pair of W^- bosons are created at the first vertex during the conversion of a neutron to a proton and then these bosons exchange the Majorana neutrino to produce a pair of electrons. Whereas in $2\nu\beta\beta$ decay there is no exchange of such a virtual particle, two neutrinos are also emitted along with β 's. The sum of energy of two emitted electrons, Q-value, in the $0\nu\beta\beta$ decay process of ${}^{76}\text{Ge}$ isotope is 2039.061 keV [57].

There is no gauge symmetry associated with the lepton number so there is no fundamental reason that the lepton number should be conserved. However, the observation of $0\nu\beta\beta$ decay would also violate the baryon-lepton (B-L) number which is considered the fundamental symmetry

in the Standard Model. If neutrinos are heavy Majorana fermions [58–61], decay of such Majorana neutrinos violates the lepton number conservation and it is allowed in the SM of particle physics. There is a possibility of the creation of slight matter and antimatter mass asymmetry resulting from the decay of heavy Majorana neutrino in the early universe into leptons and antileptons [62, 63], this may be explained by the process known as Leptogenesis [64, 65]. By the see-saw model [66–68], the existence of heavy Majorana neutrinos can also explain why neutrino are not mass-less and have such a tiny mass. Majorana neutrinos are their own antiparticles, and $0\nu\beta\beta$ decay [69, 70] becomes possible.

Several large-scale experiments aimed at searching for $0\nu\beta\beta$ decay. Some of the experiments currently in the run have a capacity to cover the parameter space of inverted mass ordering as well as some part of the normal hierarchy region of absolute neutrino mass. The goal of the current $0\nu\beta\beta$ decay experiments is also to study the viability for future large-scale experiments which can cover inverted as well as a normal hierarchy of neutrino masses. The Cryogenic Underground Observatory for Rare Events (CUORE) [71] and Sudbury Neutrino Observatory (SNO⁺) [72] studies the decay of ¹³⁰Te isotope. KamLAND-Zen 800 [73], The Enriched Xenon Observatory (EXO/nEXO) [74], Neutrino Experiment with a Xenon TPC (NEXT) [75] uses scintillating noble gas, xenon (Xe), enriched in ¹³⁶Xe. LEGEND [31, 48] is in operation using ⁷⁶Ge as a source and a detector. There are several other experiments searching for $0\nu\beta\beta$ decay using various technologies such as gaseous tracking detectors, scintillating bolometers, solid time projection chambers, etc.

Detector exposure is defined as the product of the sensitive mass of the detector and time of operation. Exposure and energy resolution are two main aspects that determine the sensitivity of the $0\nu\beta\beta$ decay searches. To date, Xe-based experiments have had greater exposure than Ge-based experiments, but the energy resolution of Ge detectors is far better. This has made it possible for Ge-based experiments to put the best limits or be in a competitive stage despite shorter exposure.

2.1.1 Neutrinoless Double Beta Decay Searches Using Ge Detector Technologies

The GERmanium Detector Array (GERDA) [29, 76–79] and the MAJORANA DEMONSTRATOR (MJD) [80–82] experiments searched for the $0\nu\beta\beta$ decay from ⁷⁶Ge isotope. Next-generation

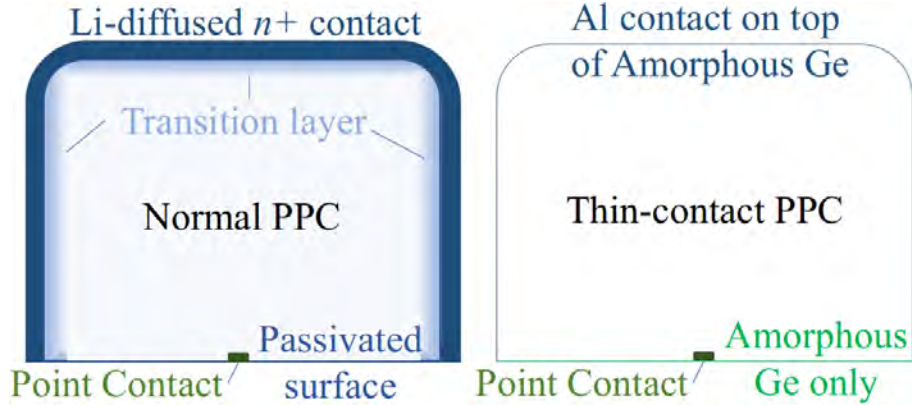


FIGURE 2.2: Shown is the comparison between a normal and a thin-contact PPC HPGe detector (not to scale).

experiment LEGEND [31, 48], a merger of GERDA and MJD, has started searching $0\nu\beta\beta$ decays using HPGe detectors dipped in liquid argon (LAr). The liquid argon acts as a coolant, a passive radioactive background shielding, as well as an active background veto.

The detectors deployed in GERDA were mostly p-type point-contact (PPC) HPGe detectors [83, 84], broad-energy germanium (BEGe) detectors [85, 86], and coaxial germanium detectors [79]. The detectors that are in use for LEGEND are mostly inverted-coaxial PPC. The point-contact detector is fully depleted at a relatively low bias voltage than the planar detector. A borehole feature on the opposite side of the point-contact detector further decreases the bias voltage required to deplete it fully. Hence, the large-size detectors can be fabricated and tested using the inverted-coaxial geometry.

The Ge detectors that were used in GERDA and MJD, and are used in LEGEND, most portion of the HPGe surfaces are fabricated with Li-diffused contact layer. These contacts are typically 1 mm in thickness, and it creates a transition layer underneath the Li-diffused layer of about the same thickness. Therefore, the active volume of the HPGe detector reduces substantially [83, 87–90]. To illustrate, consider a small PPC geometry detector of 3 cm \times 3 cm in height and diameter. For this size of PPC detector, the dead-layer and transition-layer created by a Li-diffusion may take up to 26 % of the volume of the crystal. If a large-size crystal of size 10 cm \times 8.4 cm in height and diameter, respectively, the effect of the dead and transition layer drops to about 9 %.

However, it is still a non-negligible fraction taking into account the cost of a ^{76}Ge -enriched PPC.

In a search as rare as $0\nu\beta\beta$ decays, it becomes important to shield or veto background events to increase the sensitivity of the experiment. One of the concerning backgrounds for LEGEND will be from the decays of ^{42}K (daughter of ^{42}Ar) decays with a Q-value of 3525 keV). High energy β 's from ^{42}K decay can become backgrounds to 2039 keV $0\nu\beta\beta$ decay signal from ^{76}Ge). GERDA observed the collection of ^{42}K ions in the detector electrodes. A number of solutions have been proposed to mitigate this effect, notably, the use of nylon shroud [91] or an underground argon (that is expected to be largely devoid of ^{42}K) [92] veto. Another idea discussed to mitigate the backgrounds from the decays of ^{42}K is an artificial enlargement of the Li-diffused layer but that would trade the active volume of the detector.

One alternative could be the use of thin contacts as shown in Figure 2.2. There are already commercial PPC detectors available in the market with their end surfaces made of thin contacts that are sensitive to α , β , and low-energy X-rays [93]. If the entire lithium-diffused contact is replaced by a thin contact, the sensitive volume of a large PPC can be enlarged by about 9%. This could be an exciting prospect for a ton-scale experiment like LEGEND. Since the thin contact can be penetrated by α , β , and γ particles, the use of low radioactivity underground argon [94], selection of radio-pure materials close to the detector, mitigating surface contamination, and an active LAr veto may be necessary to reach the desired physics goals.

Thin contacts can be easily segmented. Typically, signals from a surface segment have worse energy resolution than those from the point-contact due to the larger capacitance of the segment. However, they can be used to precisely reconstruct the event time, especially that of events that occur close to the surface. Combining the time information from segments and the energy information from the point-contact can help identify surface events which can allow additional suppression of backgrounds. However, an increase in the number of contacts may necessitate more readout cables and front-end electronics, which may increase the backgrounds. There may be a trade-off in maximum segmentation achievable without compromising on the background budget. Optimized segmentation can be achieved after the detailed Monte Carlo studies. A simple scheme for a PPC detector would be a segment for its side surface and another for the end surface opposite to the

point-contact side.

Typically thin contacts are designed by sputtering Ge or Si on bare HPGe crystals followed by the deposition of a thin layer of Al to form electrodes [16–19]. a-Ge/a-Si can block the injection of electrons and holes from contacts to the bulk of a detector, while still allowing charge carriers from the bulk to be collected on contacts [15]. The amorphous material acts as a passivation layer where it is not covered by Al electrodes. This technique has been well developed over the last two decades and was used to produce large planar strip HPGe detectors by Mark Amman at the Lawrence Berkeley National Laboratory (LBNL) [24] to detect soft γ -rays (0.2–5 MeV) in the Compton Spectrometer and Imager (COSI) [95, 96] experiment. The thin contact properties have been understood very well, they have survived even in harsh operating environments including a crash-landing of a COSI balloon [96].

2.2 Dark Matter

Zwicky’s observations [97] of velocity dispersion of nebulae in the Coma cluster of the galaxies in the early 1930’s revealed the presence of a significant amount of non-luminous matter (dark matter) in the galaxies. Applying the Virial theorem, Zwicky calculated that the galaxies are much more massive than that can be accounted for by the mass of ordinary matter alone [98]. Another strong evidence for the presence of dark matter comes from the rotation velocity curve of a galaxy. The spectroscopic observations show the luminous matter is mostly concentrated close to the core of a galaxy. However, the rotational velocity of the molecular clouds is observed to be constant beyond a few kiloparsecs from the center of the galaxy, well past the visible disk of a galaxy [99]. Gravitational lensing and Cosmic Microwave Background (CMB) power spectrum measurements also reveal that dark matter is a major contributor to the mass of a galaxy and galaxy clusters [100–103]. Overall mass-energy content of our universe comprises $\sim 68\%$ of dark energy, $\sim 27\%$ of dark matter, and $\sim 5\%$ of visible matter.

It is fairly well-established that none of the SM particles are viable candidates for dark matter. Some popular dark matter candidates that arise in beyond-the-SM theories are axions, sterile neutrinos, weakly interacting massive particles (WIMPs), and supersymmetric particles [104]. At

this point, one of the most favored dark matter candidates is WIMPs. WIMPs are often assumed to be thermally created and assumed to be in thermal equilibrium with SM particles in the early universe. Based on this assumption it can be shown that following the evolution of the universe, WIMP relic density corresponds to observed dark matter density provided the WIMP interaction cross-section is in a weak interaction regime. So, WIMPs interact very weakly with ordinary matter and may leave detectable signals in our terrestrial detector. Some WIMPs-like particles are predicted by supersymmetric theories. One such candidate dark matter particle is neutralino. The WIMP candidates have masses in the range of 1 GeV to 10^5 GeV and interaction cross-sections with ordinary matter is 10^{-40} to 10^{-50} cm² [105].

Neutrino exists in three flavors, ie. electron, muon, and tauon. A present-day abundance of SM neutrinos and their tiny mass suggest SM neutrinos are not viable dark matter candidates. Some beyond-the-SM models predict the existence of heavier neutrino: sterile neutrino. Sterile neutrino models have been proposed to explain the mass generation of the SM neutrinos as well as to explain dark matter [106, 107].

Another motivated candidate for dark matter is the axion. Originally, introduced by Peccei and Quin in 1977 to resolve the strong charge-parity (CP) problem in quantum chromodynamics (QCD), axions can also be a viable dark matter candidate if they have a tiny mass (order of eV or lower) and suitable coupling strength [108–110].

2.2.1 WIMP Detection Principle

Most sought WIMP signal is the signal from WIMP elastically scattering off some target nuclei. In the Center-of-Momentum (CM) frame, the recoil energy (E_R) can be expressed in terms of scattering angle (θ) in the extreme non-relativistic limit as [111];

$$E_R = \frac{\vec{q}^2}{2m_N} \tag{2.5}$$

where \vec{q} is the momentum transfer, q^2 is expressed as $q^2 = 2\mu^2v^2(1 - \cos(\theta))$, \vec{v} is the mean velocity of the WIMP, and μ is the reduced mass of the WIMP-nucleus mass which is given by

$m_\mu = \frac{m_N + M_\chi}{m_N M_\chi}$, where m_N and m_χ are the mass of the nucleus and WIMP particle respectively.

The differential event rate for nuclear recoils from WIMP interactions (usually expressed in counts/(kg.day.keV)) is given by;

$$\frac{dR}{dE_R} = \frac{\rho_0}{m_N m_\chi} \int_{v_{min}}^{\infty} v f(v) \frac{d\sigma}{dE_R}(v, E_R) dv \quad (2.6)$$

where ρ_0 is the local WIMP density, $\frac{d\sigma}{dE_R}(v, E_R)$ is the differential cross-section for WIMP-nucleus elastic scattering, $f(v)$ is the normalized WIMP velocity distribution in the detector frame, ρ_0 is the local dark matter density which is $\sim 0.3 \text{ GeV/cm}^3$ on average near to the Earth. The minimum speed of WIMP that can induce nuclear recoils is denoted by v_{min} in the above equation and it is given by, $v_{min} = \sqrt{(m_N E_R)/(2\mu^2 v^2)} = \frac{q}{2\mu}$. The upper limit for the velocity of WIMP is the escape velocity v_{esc} , above this limit WIMPs are not gravitationally bound to Milky Way galaxy.

The average ratio of kinetic energy transferred by a WIMP to a target nucleus is directly proportional to the mass of the target nucleus and is given by

$$\frac{E_R}{E_\chi} = \frac{2\frac{m_N}{m_\chi}}{1 + \frac{m_N}{m_\chi}} \quad (2.7)$$

If WIMPs have smaller mass, detectable nuclear recoils are even smaller, and low threshold detector is necessary. The higher the mass of the nucleus larger the nuclear recoil energy, hence the heavy target material such as Ge is preferred. The nuclear recoil energy (E_R) deposited in a detector from a WIMP particle masses (1 GeV-100 TeV) is ~ 1 -100 keV [105] which requires a detector with good energy resolution and low energy threshold. If an electron recoil happens then the mass of the nucleus (m_N) can be replaced by the mass of the electron (m_e) in Equation 2.7, which requires an ultra-low energy threshold detector since m_e is far less than m_N .

Integrating the differential event rate over all possible recoil energies gives the total event rate which is given as;

$$R = \int_{E_T}^{\infty} \frac{\rho_0}{m_N m_\chi} dE_R \int_{v_{min}}^{v_{esc}} v f(v) \frac{d\sigma}{dE_R}(v, E_R) dv \quad (2.8)$$

where E_T is the smallest E_R measurable by the detector called as threshold energy. In general, $d\sigma/dE_R$ can be separated into spin-independent and spin-dependent parts,

$$\frac{d\sigma}{dE_R} = \left(\frac{d\sigma}{dE_R}\right)_{SI} + \left(\frac{d\sigma}{dE_R}\right)_{SD} \quad (2.9)$$

The cross-section of the WIMP interaction with the nucleus can have two components, ie. spin-independent, and spin-dependent. Former results from scalar or vector couplings to quarks; later, from axial-vector couplings to quarks. The spin-independent differential cross-section is directly proportional to the square of a mass number, ie. $\left(\frac{d\sigma}{dE_R}\right)_{SI} \propto A^2$, whereas the spin-dependent differential cross-section scales with the spin of the nucleus, ie. $\left(\frac{d\sigma}{dE_R}\right)_{SD} \propto J(J+1)$, where J is the nuclear angular momentum [112]. A detector material with heavy nuclei is preferred for the direct detection of the WIMPs since the spin-independent (scalar) component in Equation 2.9 dominates for heavy target nuclei ($A > 20$). Hence, Si, Ge, argon (Ar), Xe are the most preferred target materials in WIMPs searches.

The spin-independent interaction limit set by various large-scale experiments using various detector technologies are shown in Figure 2.3.

Experiments usually are sensitive to WIMPs in the mass range of a few GeV/c^2 to $100 \text{ GeV}/c^2$. Current Ge detector technologies used by SuperCDMS and EDELWEISS are capable of differentiating between electronic and nuclear recoil when operated in ionization and phonon signal mode simultaneously. They have the capability of detecting the WIMP mass of the order of ten's of GeV/c^2 . It becomes difficult to differentiate between electronic and nuclear recoil when the mass of the dark matter candidates becomes less than the sub-GeV scale. The detection of MeV scale dark matter requires the improvement of the existing detector technologies. Recent results published from Xenon1T claim that they have reached the detection limit in the range of 1 - 7 eV [115]. In addition, the results published by The Cryogenic Rare Event Search with Superconducting Thermometers (CRESST) based on characterization of 2.66 gm of Li_2MoO_4 target crystal have shown that $\sim 1 \text{ eV}$ detector threshold can be achieved [116]. Mei. et al, have proposed the idea of using a Ge detector in an internal charge amplification mode [35]. The charge carriers can be created in

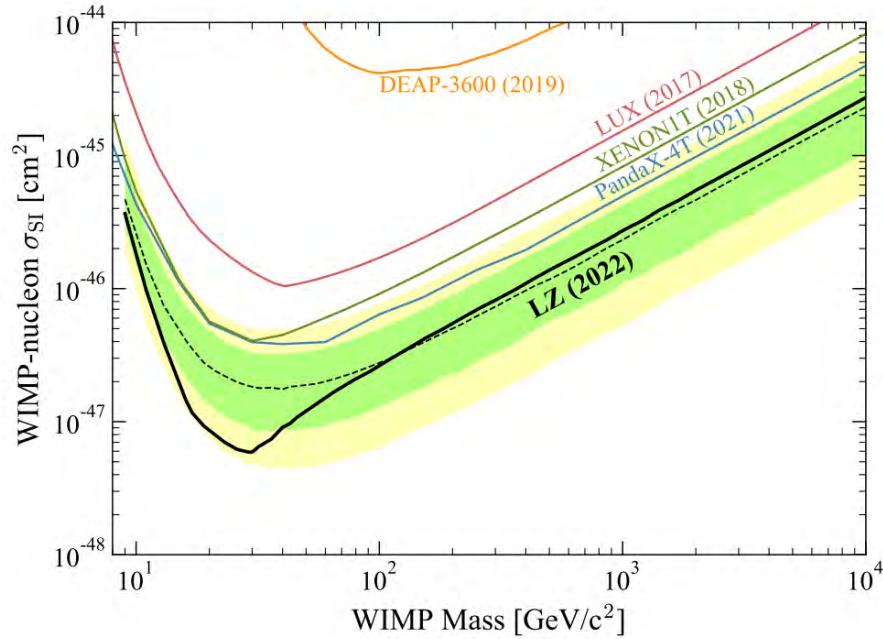


FIGURE 2.3: Shown is the spin-independent interaction limit as a function of WIMP mass set by various experiments. The black line represents the 90 % confidence limit, green and yellow bands represent the 1σ and 2σ sensitivity bands respectively for the LUX-ZEPLIN (LZ) experiment. The figure is taken from [113].

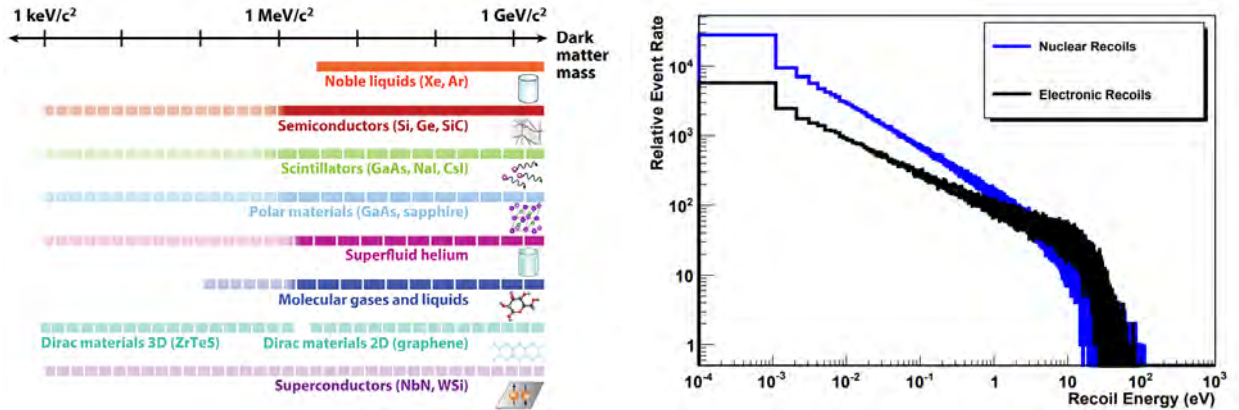


FIGURE 2.4: Left: shown are the detector materials used or under consideration for detecting sub-GeV dark matter. A solid line represents that the detector is currently in use for that mass sensitivity range. A long-dashed line represent the detector shown under consideration for the near term and a short-dashed line under consideration for the long term. The mass-sensitivity range is shown on the horizontal axis [114]; Right: shown is the relative event rate as a function of recoil energy for light dark matter searches [35].

a Ge crystal by ionization and excitation of impurity atoms. The shallow impurities of the order of 0.01 eV exist in an HPGe crystal. Charge carriers or phonons having an energy of more than 0.01 eV can excite and ionize the impurity atoms to create charge carriers from the donor (n-type impurity) or acceptor (p-type impurity) level of the atoms. The charge carriers gain high kinetic energy larger than the band gap of Ge while drifting through the application of the electric field. Hence cascade of charge carriers can be created. This mode of application may have the capability to reach as low as 0.1 eV threshold and differentiate between electronic and nuclear recoil in the range of sub-eV - 100 eV. Based on this model the relative event rate as a function of the nuclear and electronic recoil energy is shown in Figure 2.4.

Germanium Detector Fabrication with Amorphous Germanium Contacts

This chapter will give a brief overview of the zone refining, crystal growth, crystal characterization, and detector fabrication carried out at USD. Contact geometry changes the overall characteristics of the detector. There is a discussion on various contact geometries implemented in HPGe detectors in large-scale Ge-based experiments. Also, the key issues that arise in the detector fabrication process are discussed. a-Ge/a-Si contacts are the best alternatives for Li-diffused contacts. They can withstand a large enough electric field. However, the main drawback is that the leakage current of these contacts is higher than that of the Li-diffused contacts. The p^+ contacts formed by Boron ion implantation and n^+ contacts made with Li diffusion have a high concentration of holes and electrons respectively, therefore if used appropriately (p^+ and n^+ contacts for blocking electrons and holes respectively) the injection of charge carriers can be minimized. Though the leakage current is relatively higher than using doped contacts, a-Ge contacts possess several advantages over those contacts for searching rare-events.

3.1 HPGe Single Crystal

Raw Ge materials are zone refined and then grown into a single crystal. The wafers are characterized using the Hall effect measurement system for further processing of the crystal.

3.1.1 Zone Refining

Zone refinement is used to segregate the impurities. It is widely used in refining impurities in Ge and Si. It is a prerequisite process for single crystal growth to lower the impurity concentration, in this case, of the germanium ingots. Zone refining works on the principle of fractional crystallization. The difference in solubility of the impurities in the solid and liquid phases in Ge makes it possible to segregate the impurities. The segregation coefficient (K_0) of impurities in Ge is defined as

$$K_0 = \frac{C_{i,Solid}}{C_{i,Liquid}} \quad (3.1)$$

where, $C_{i,Solid}$ and $C_{i,Liquid}$ are concentrations of impure atoms in solid and liquid phases respectively. If the segregation coefficient is less than 1, impure atoms are mostly in the molten phase. The impurities that have a segregation coefficient close to 1 distribute uniformly throughout the ingot while the impurities with a segregation coefficient greater than 1 remain mostly in the solid phase during crystallization. When the hot inductive coil repeatedly moves over the Ge ingot, impurities accumulate at the two ends of the ingot according to their segregation coefficient with Ge. This process is repeated multiple times along one direction of the ingot. After several passes, the middle portion of the Ge ingot becomes pure (low-impurity concentration) than the head and tail part. The main impurities found in the Ge ingots are Al, boron, gallium, and phosphorus in our lab.

3.1.2 Crystal Growth

Zone refining usually brings the impurity level down to 10^{11}cm^{-3} [2]. The next step is to grow a large size HPGe crystal using the poly-crystalline Ge ingots obtained after the zone refining process. During the crystal growth, atoms are aligned in a crystalline structure. Czochralski method [3, 4] is one of the best techniques to grow a large size single crystal. The Ge crystal grown using the Czochralski process is shown in Figure 3.1. RF power supply is connected to the graphite boat which transfers heat to the quartz crucible and Ge starts to melt down. After the Ge melts, the seed is lowered to touch the molten part. The crystal growth is carried out in an

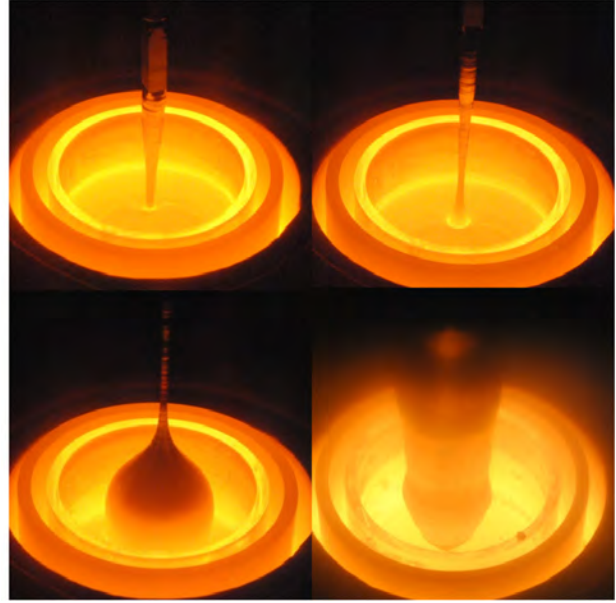
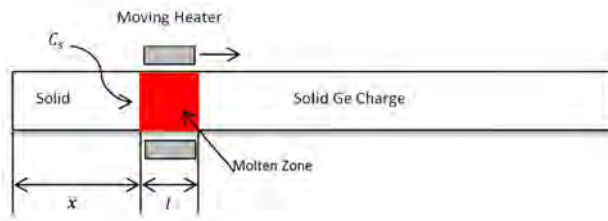


FIGURE 3.1: Left: shown is the schematic of the zone-refining process. Heater, molten zone, and impurities move from left to right through the solid charge during the zone refining process. The segregation of impurities occurs in the molten zone; Right: single crystal growth of Ge by the Czochralski process (taken from Hao Mei's thesis).

atmosphere of hydrogen (H_2) to minimize the Si oxide formation from the quartz crucible which might create trapping centers in a Ge crystal. USD lab can grow crystals with diameters in the range of 3.5 - 12.7 cm [5]. Growing a large crystal boule allows us to understand the impurity concentration profile of the crystal along the radial as well as the axial direction. The pulling rate and temperature profile of the crystal determine the diameter of the crystal. Detector-grade crystal requires uniform distribution of dislocations in the range of 300 - 10,000 / cm^2 . Large thermal conductivity, convective heat transfer coefficient, and lower viscosity of hydrogen gas make it difficult in controlling the thermal field and creates a challenge for growing crystal within the desired dislocation density. Controlled doping of impurities in semiconductors can be done to characterize the electrical properties of the semiconductors.

3.1.3 Crystal Characterization

It is important to check the impurity and dislocation density of the crystal after the crystals are grown to find out if the crystals can be processed for the fabrication of the detector or if it needs

to be grown again. Four-point resistance measurement is a common technique to find the impurity concentration of the Ge crystal. An impurity concentration of the crystal determines what size of the detector can be fabricated. Though, the geometry of the contacts is also crucial in determining the size of the crystal to be processed for the detector fabrication. Higher impurity concentration leads to the scattering of charge carriers. The impurity concentration of the crystal is lower than in zone refined materials if there is no additional contamination during the crystal growth process.

To make a successful detector it has to go through different steps, which is time-consuming and expensive. The Hall effect measurement is an efficient method to do the initial test of the crystal sample. For Hall effect measurements, the following processes are desirable. First, the wafers of small thickness (~ 0.2 cm) are cut using a diamond wire saw from the shoulder, and tail of the grown crystal. Usually, the detector grade crystal is found in the middle portion of the crystal. The shoulder and tail position gives the idea to make another cut to find out the HPGe crystal. Second, the wafer is cut into small samples of size ~ 1 cm \times 1 cm \times 0.2 cm in length, breadth, and height, respectively. Third, the samples are lapped and polished using sandpaper and powders and then etched in a hydrofluoric and nitric acid solution (1:4) for a few minutes. Fourth, the electrical contacts using Gallium Indium eutectic are made on the four corners of the already etched samples. Four pins are connected to the contacts made on the sample and the sample is cooled down to 77 K using liquid nitrogen to test the physical and electrical parameters such as impurity concentration, resistivity, mobility of charges, etc. The resistivity of the semiconductor material is a strong indicator of how it resists the electrical current. It depends on the mobility of charge carriers, hence on the temperature. The resistivity of the material is defined as;

$$R = \frac{1}{nq(\mu_e + \mu_h)} \quad (3.2)$$

where n is the free electron or hole charge carrier concentrations depending on the type of impurity crystal, q is the electronic charge, μ_e and μ_h are the mobility of holes and electrons respectively. The type of the crystal is identified by the sign of net impurity concentration, electrons carry a negative sign and it refers to an n-type crystal whereas positive sign refers to the majority of

impurities being p-type. It is important to know the type of impurity crystal for the fabrication and characterization of the detector. Its implication is discussed in later chapters.

Dislocation density is the measure of the number of etching pits per cm^2 . The lapped and polished samples are further cleaned using the etchant ($\text{CH}_3\text{COOH}:\text{HNO}_3:\text{HF}$ (11:10:5) with 30 mg Iodine(I_2) dissolved). Then the high-resolution optical microscope is used to observe the etching pits. The desired dislocation density is in the range of 300-10000 $/\text{cm}^2$ [15] for the detector grade crystal. If the dislocation density falls above that range, the charge trapping from the dislocation itself becomes significant. However, if the dislocation density falls below the range, deep impurities such as divacancy-hydrogen complex (V_2H) increase as they can take the interstitial position between Ge atoms. These deep traps can have a capture cross-sections above 10^{-13} $/\text{cm}^2$ [46], in which case, the detection efficiency and the energy resolution of the detector is compromised.

3.2 Ge Detector Fabrication and Challenges

Ge is brittle in nature. A diamond saw is used to cut the crystal boule and give the crystal desired geometry. Grinding the Ge crystal is preferable to cutting to avoid cracks or chips. Typically, the grinding speed is less than 2 mm per minute. Handling the crystal sample well is necessary for detector fabrication. a-Ge contacts are likely to fail the electrical test even in the case of a small scratch during detector fabrication and loading. To design a proper detector crystal, the Ge crystal has to be processed carefully. The steps involved in the process are described in greater detail below.

3.2.1 Mechanical Processing

The detector-grade Ge crystal grown from Czochralski pullers in the H_2 atmosphere is diced into about $2 \times 2 \times 1 \text{ cm}^3$ cuboid with diamond wire saws and grinding blades. Each cuboid is further grounded into a top hat shape, as shown in Figure 3.3. The brims are used to handle the crystals so that their sensitive surfaces remain untouched during fabrication and operation. The geometry of the crystal sample can be rectangular or square. Developing square-shaped geometry makes the handling of the detector easier during detector fabrication. Before starting to cut and grind the

crystal boule, it is necessary to glue the graphite plate on the stainless steel and then the crystal on top of the graphite plate using sticky wax. It should be emphasized that overheating of Ge crystal should be avoided when gluing in the graphite or taking it out after finishing the cutting. Cold water has to be supplied continuously to avoid excessive heating during the cutting and grinding of the crystal. The stainless steel is placed into the vacuum chuck and aligned perfectly with the diamond saw. The setup for cutting the crystal is shown in 3.2. First, a 0.5 mm width diamond blade is used to get a cuboidal shape, and then a 2 mm width blade to make wings and grooves.

Following the cutting process, the wax that initially glues the crystal on the top of the graphite plate is removed. Since the wax is acid-resistant, it is desirable to clean the entire surface of the crystal using trichloroethylene (TCE). If the wax attached to the top and bottom surface is not removed, it creates a problem with the lapping of the crystal. Small remnants of the wax can also be lapped away during the lapping of the crystal for the top and bottom surfaces. Since the grooves are not accessible for lapping, they require special attention. Each crystal should be chemically etched before the contact formation, hence the acid-resistant wax should be completely removed.

Cutting and grinding of the crystal create blade marks. It is also possible to have small cracks or chipping along the edge of the crystal. Mechanical lapping of crystal helps to remove those defects. Lapping can be coarse and fine lapping. Coarse lapping can quickly remove the chips and scratches from the top and bottom surfaces of the crystal. If both surfaces are smooth and flat without any visible chips and scratches, coarse lapping may not be necessary, and only fine lapping is required. The top and bottom surfaces of the crystals are lapped using micro-abrasives Si carbide (SiC) and Al oxide (Al_2O_3) with 17.5 and 9.5-micron grids, respectively, to remove visible scratches from cutting. A slurry can be made of each of these powders mixed with de-ionized (DI) water. Gentle downward pressure is applied on coarse lapping with the movement of the crystal directed in figure eight or the circular motion. The downward pressure is not needed for the fine lapping so a scratch-free surface can be obtained easily. The same process can be repeated to completely lap away any chips at the edges of the crystal. A uniform texture on both top and bottom surfaces are desirable. It is also necessary to make the top and bottom surfaces parallel. Blade marks left on the sides of the crystal are difficult to lap due to the presence of wings and grooves. However, if

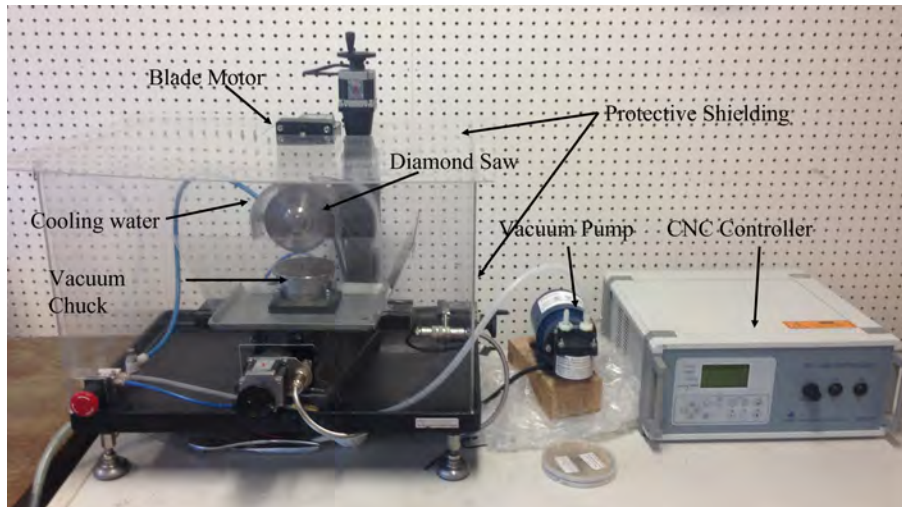


FIGURE 3.2: Shown is the setup for cutting and grinding the crystal to turn it into the desired geometry.

chips are present, they should be removed with gentle lapping on the edge of the glass plate in the vertical direction. Then the crystal is rinsed thoroughly with DI water and dried with dry nitrogen gas.

3.2.2 Chemical Processing

The purpose of etching the already lapped crystal is to obtain smooth and clean surface. Micro-scratches and defects not visible with the naked eye during lapping become visible if there are any after the chemical etching process. If minor scratches still remain after the chemical etching, it is desirable to do fine lapping again. Lapped crystal pieces are submerged in a mixture of HF and HNO₃ acids in a ratio of 1:4 to etch away small surface defects. Safety precautions are important in handling such types of strong etchants. Personal protective equipment (PPE) is required to avoid accidental damage, and the entire etching process should be carried out inside the fume hood. Etching requires two steps. First, a long-term etching, which takes around 3-4 mins and the second, short-term etching that takes around 30-45 secs. During a long-term etching, the crystal is submerged directly into the etchant containing Teflon beaker. Then the crystal is agitated continuously with a rapid circular motion. The crystal must be flipped 1-2 times in between to ensure the uniform etch on all sides of the crystal. After the etching, the crystal is taken out with

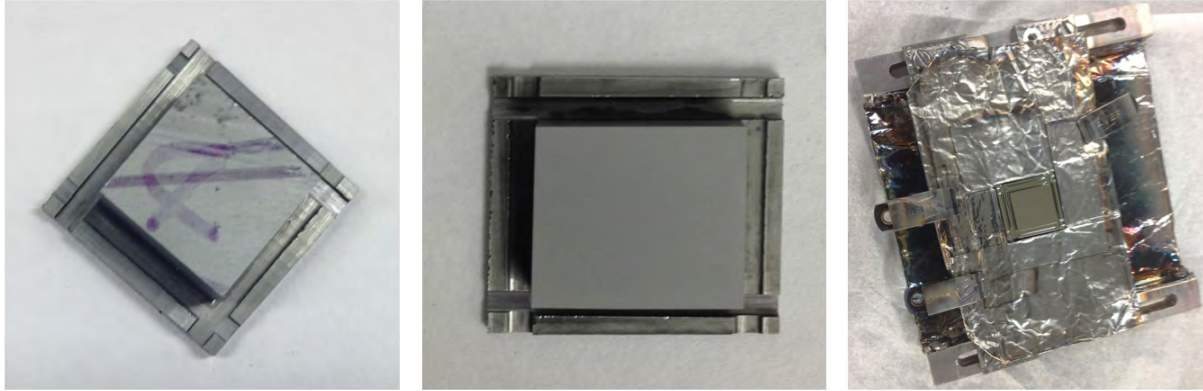


FIGURE 3.3: Shown is the germanium crystal that has gone through different process. Left: crystal after mechanical lapping; Middle: crystal after long-term chemical etching; Right: crystal loaded on the jigs with Al mask after short term chemical etching.

a Teflon tweezer and rinsed with the DI water, and dried with the dry nitrogen gas. If chips or cracks appear on the crystal then the crystal should be lapped again and the same etching process needs to be repeated. In the absence of any defects, short-term etching can be done just before the crystal is loaded into the jigs and the sputtering chamber. During the short-term etching, crystal wings should be held with tweezers all the time and then submerged into the fresh etchant without touching any other surface. Quenching in DI water and blowing the water with dry nitrogen gas are required after each etching process. In addition to avoiding the scratches, cloudy surface also needs to be avoided to begin thin film deposition. If a cloudy surface is present, etching should be done again. Typically, cloudy surfaces can be removed by applying a strong etchant for 30 seconds or so. By the end of the process, the expectation is the crystal has a smooth and shiny mirror-like surface.

3.2.3 Contact Formation

The formation of contacts on the Ge crystal is an important step in the detector fabrication. a-Ge contact is used to passivate crystal surface, and in addition, to provide the barrier height for charge injection. Al contacts are necessary for making electrodes which are needed to provide a bias voltage to the detector and signal read-out from the detector. a-Ge contacts are high-resistance contacts while Al contacts are low-resistance contacts. We have adopted the similar recipe developed by the



FIGURE 3.4: Shown are the equipments used to carry out the contact formation on the high-purity germanium crystal. Left: Perkin Elmer (2400 model) Sputtering machine at USD used for the a-Ge and Al deposition; Right: Electron-Beam machine at USD used for the Al deposition on top of a-Ge contacts.

LBNL [24] with some minor adjustments. The properties of a-Ge differ with changing the process parameters such as H_2 content in the H_2 Ar gas mixture, sputter pressure, power, thickness of the film, etc. [24].

Sputtered a-Ge Contacts

Immediately after short-term etching, the etched crystal is placed on the jigs. Indium foil is attached on the top of the jigs to avoid scratches when the crystal sits on the jigs. Only the wings of the crystal is touched to the indium-layered jigs, which remains un-depleted and does not affect the detector performance. Before loading the etched crystal into the sputtering chamber, the crystal is surrounded by an Al foil mask to minimize the back-sputtering of a-Ge atoms onto the down side of the crystal. The sputtering chamber is first vacuumed below 4×10^{-6} Bar and then pressurized at 14 mTorr with the H_2 and Ar gas mixture (7:93). The role of H_2 gas is to make high resistivity a-Ge contacts. The RF sputtering system used for the deposition of a-Ge is Perkin Elmer (model 2400). Typically 100 watt forward power and 0 watt reflected power is maintained and transferred to the gas mixture. Then the plasma is created ionizing the gas molecules and confined in the space containing a HPGe crystal. Then, ions are accelerated to the a-Ge target. Neutral atoms are ejected from the target and get deposited into the Ge crystal. Prior to the deposition on the surfaces

of the crystal, pre-sputtering was done with the shutter closed position for ~ 5 minutes to clean the target. A continuous flow of coolant for the detector stage and the target makes possible an uninterrupted deposition of a-Ge for ~ 15 minutes. Without the coolant each deposition is carried out for ~ 3 minutes with a 10 minutes interval in order to avoid excessive heating of Ge crystal. After sputtering the top and four sides of the crystal and allowing sufficient time for the crystal to cool down, the crystal can be taken out and flipped upside down. The same process is repeated for the bottom surface. The preference is given for sputtering on top and side surfaces first so larger surface area gets passivated first. After the first deposition, detector sample should be taken out of the sputtering chamber, flipped upside down and loaded into the chamber. Therefore, for the other surface there is a chance for additional contamination from the environment. The Alpha-Step Profiler was used to measure the thickness of the a-Ge layer coated on Ge crystal. In our work, the thickness of the a-Ge layer at top and bottom surfaces following a 15 minutes deposition was ~ 600 nm. For the side surfaces, however, there is a difference in height and the angle of sputter that resulted in a varied thickness: between ~ 350 nm near the top edge and ~ 250 nm near the bottom edge of the crystal.

Aluminum Deposition

At USD, Al deposition is done with an E-Beam machine or a Sputtering machine. The purpose of Al deposition is to provide a low-resistance contact area to test the electrical properties of the detector. Differences in the working principle and the contact properties for those methods are discussed below.

Evaporation Method

After the a-Ge is deposited in a crystal, the crystal is directly moved into the E-beam machine for the Al deposition. A high vacuum level (less than 4×10^{-6} torr) is required for the material deposition using the evaporation method. The electron beam coming out of the tungsten filament converges to the crucible containing aluminum and aluminum-melted. The evaporated Al atoms go to the crystal surface and get deposited. The desired conditions for our E-beam system are

4.89 kV high voltage, the deposition rate of 0.2-0.4 nm/s, and a thickness of Al layer \sim 100 nm. After the top and side surfaces were coated with the Al layer, the crystal is flipped and the coating process is repeated for the remaining side of the crystal.

Sputtering Method

Al deposition was also carried out in the sputtering chamber with a DC power supply. The process is similar to that of a-Ge deposition. The main difference is the use of Ar gas instead of H₂ and Ar gas mixture being placed at chamber pressure 3 mTorr. The thickness of \sim 150 nm can be achieved within 5 minutes of the deposition.

3.2.4 Contact Geometries

The last step in the detector fabrication process is to make contacts on the detector. This requires the removal of some of the Al-layer from the detector surface to separate the contacts. Acid-resistant tape is placed gently on the surfaces where the Al needs to be kept intact. This tape has low adhesion and no residue is left after it is removed. Q-tip is used to press gently and smooth out the tape on the detector surface to avoid air bubbles. Then the taped protected detector is handled with the Teflon tweezers and submerged in HF dip (1%) solution for \sim 3-4 minutes. Agitation helps to remove the gas bubbles that cling to the exposed surfaces. The detector should be immediately taken out from the acid solution after the set period of time and then it should be quenched in DI water for several seconds. Afterward, the detector is thoroughly dried with dry nitrogen gas. If the size of the detector is large it is better to quench in methanol after quenching in DI water which helps to dry the detector faster. Incomplete removal of Al from the region other than the contacts might cause the detector to break down. The a-Ge remains unscathed on all surfaces of the detector when etching in 1% HF solution. Different contact geometry can be made on the detector depending on its application. The discussion about the planar, point-contact detector that was fabricated in our USD lab follows. There exist several other contact geometries such as strip detector, coaxial detector, ring-contact detector, etc. After contact geometry is made, fabricated detector is loaded directly into the cryostat for characterization.

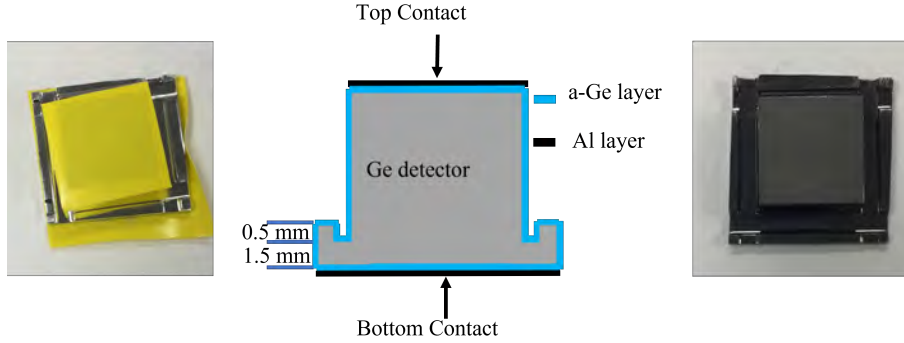


FIGURE 3.5: Shown in the contact formation process for a planar detector geometry. Left: acid resistant tape placed on top and bottom surface of the detector; Middle: schematic representation of a Ge detector with a planar structure (not to scale); Right: a planar Ge detector fabricated at USD.

Planar Geometry

In planar geometry, the Al of the two flat surfaces (top and bottom surfaces) of the detector is kept intact while the side surface Al is removed. Kepton acid-resistant tape is employed to cover both the top and bottom surfaces of the detector. The schematic representation is shown in Figure 3.5. This is the simplest form of detector geometry that can be made on a Ge detector. The main limitation of this geometry is the thickness of the crystal since the full depletion voltage (V_d) is directly proportional to the square of the crystal thickness for a given net impurity concentration of the crystal. There are several advantages of using planar geometry. First, the electric field distribution inside the detector and the mobility of charge carriers can be calculated with high precision. Second, impurity concentration on a small size planar detector varies a little along the axial and radial direction. Third, a-Ge coated Ge planar detector is useful in exploring the charge trapping phenomena since the alpha particles deposit energy within the order of micrometers thickness.

A guard-ring structure can be made on a planar geometry detector. The main purpose of a guard-ring detector is to separate the bulk leakage current (BLC) from the surface leakage current (SLC). The schematic representation of the guard-ring detector is shown in Figure [reff:GuardRingDetector](#). In addition to removing the Al-layer from the side surfaces, a ring of Al is etched away from the top surface surrounding the central contact. The V_d does not alter when adding a guard-ring structure.

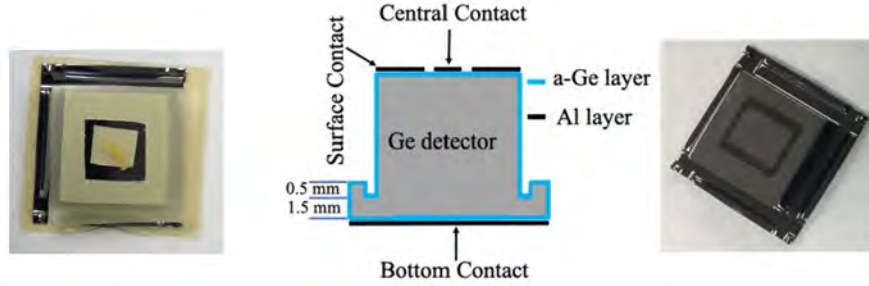


FIGURE 3.6: Shown is the guard-ring structure formed on a planar geometry detector. Left: acid resistant tape placed on top and bottom surfaces of the detector, Middle: schematic representation of a Ge detector with a guard-ring structure (not to scale); Right: a guard-ring Ge detector fabricated at USD.

In addition, the magnitude of the electric field also remains the same. However, the low capacitance of the detector can be achieved since the contact area gets smaller after adding a guard-ring structure. This structure allows us to study the various properties including barrier height, and inhomogeneity of the contacts.

Point-contact Geometry

For a point-contact detector, a ring of Al surrounding the point-contact is etched away from the top surface. The schematic of the point-contact detector is shown in Figure 3.7. One of the techniques of fabricating the point-contact detector is making Li-diffused contacts as n^+ contacts and boron ion-implanted contacts as p^+ contacts. This process requires extensive effort and is costly. Also, Li-diffused contacts create ~ 1 mm dead layer and ~ 1 mm transient layer, which reduces significantly the active volume of the detector. However, the Li-diffused detector is easier to handle during the crystal processing, since the outside diffused layer acts as a dead layer. Alternatively, we made a few point contact detectors entirely passivating the crystal using a-Ge on all surfaces of a HPGe detector and depositing Al on top of that. One of the challenges in making such a detector is in handling since the a-Ge contacts are not robust as Li diffused contacts. The main advantage of the point-contact detector is its discrimination ability for single-site and multi-site events. The capacitance of the point-contact detector is relatively less than the planar geometry detectors since the capacitance of former depends on the contact area only whereas the later also depends on the thickness of

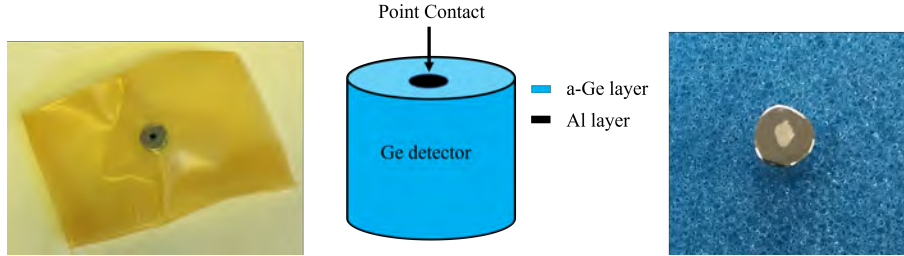


FIGURE 3.7: Shown is the contact formation process for a point-contact detector. Left: acid resistant tape placed on bottom and side surfaces, and xylene and piscine mixture to make a point contact; Middle: schematic representation of a point-contact detector (not to scale); Right: a p-type point contact Ge detector fabricated at USD.

the detector, hence providing better energy resolution. In addition, it also can detect low-energy radiations allowing the detection threshold to be low (in a sub-keV range). The bias voltage required to fully deplete the detector is comparatively less than the planar detector geometry of the same thickness, hence providing room for large-size detectors. Point-contact detectors fabricated using a-Ge contacts could be a potential detector for rare-event searches [117]. This geometry are in use extensively in $0\nu\beta\beta$ decay searches [29–31], low-energy nuclear recoils [118], and coherent elastic neutrino-nucleus scattering ($CE\nu NS$) [119].

Inverted-Coaxial Geometry

The inverted-coaxial detector has a borehole on the opposite face of the point contact. This geometry allows the detector to be fully depleted at a relatively low bias voltage than a planar and point contact geometry. A large-size detector can be fabricated and operated at a reasonable bias voltage using this geometry. This detector geometry was used by GERDA [29] and currently in use in LEGEND [48] experiment. Segmented Inverted-coaxial GerMANium (SIGMA) project also uses inverted-coaxial Ge detector for the γ -spectroscopy [120].

3.3 Conclusions

High-purity crystals can be depleted at lower bias voltage. Therefore, detectors made from high-purity crystals are preferred in the rare event searches. However, one draw back of using such high-purity crystals is that the electric field is lower than in less impure crystals. Using the Ge

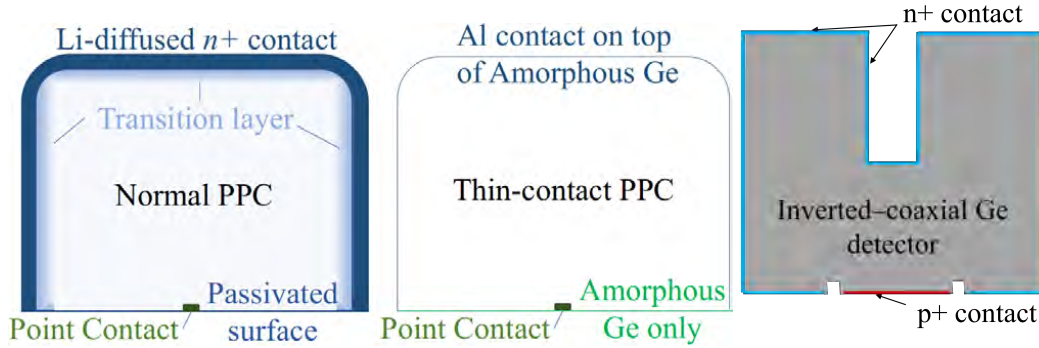


FIGURE 3.8: Left: comparison between a normal and a thin-contact PPC germanium detector (not to scale); Right: inverted-coaxial germanium detector (not to scale).

crystal grown at USD, several detectors were fabricated. The main objectives of fabricating the detector with the crystals grown in our lab are a) To find out the quality of the crystal and hence to provide the feedback to our crystal growth group, b) To compare the impurity concentration measured from the C-V characteristics to that of the Hall effect measurements and c) To efficiently and economically explore the detector properties.

There are some drawbacks of using Hall-effect based measurements to do the impurity concentration test. This method relies on the resistance of the charge impurities. First, only the measurements of resistance close to the contact surface is possible. Second, the procedure is influenced by the aspect ratio and the Vander Pauw geometry of the sample [121]. Contacts size are not even in the absence of proper mask. As a result, there are large uncertainties. Evaluating Capacitance-Voltage (C-V) characteristics is an effective way to find out the physical parameters of the crystal and the uncertainties associated with the Hall effect measurement are avoided.

Cosmic-ray activation of Ge crystal limits the performance in searching for rare events. Operations of Ge crystal such as growing the Ge single crystal, fabrication of the detector, and storage for a long time might result in the production of radioactive isotopes. These isotopes with long half-lives might impact on the background for rare-event searches. Hence, it is desired to explore the possibility of growing a Ge single crystal and Ge detector fabrication in underground labs.

Detector fabrication needs a lot of effort and patience. HPGe crystal is only the initial requirement for detector fabrication. There are a lot of factors that can affect the detector performance.

First, mechanical lapping of the crystal; second, chemical etching of the crystal; third, detector handling; fourth, process parameters; fifth, dislocation density, etc. For a detector with a-Ge contacts, it is recommended to have four-wings geometry of the crystal for the easy handling of the crystal during fabrication and characterization. One should be careful to avoid the back-sputtering of a-Ge atoms onto the rear-facing surface of the crystal. When a crystal is loaded into the sputtering jigs, Al mask should be placed close enough to the wings of the crystal.

Characterization of Germanium Detector in Cryogenic Liquids

Electrical characterization (Current-Voltage (I-V) and C-V characteristics) and energy spectroscopy measurements can help test a detector's performance. Stability of contacts is particularly desirable for large size detectors. Typically a detector handling involves various processes including transport, extended storage of the detector, and multiple thermal cycles during the operation. Long-term storage at room temperature also results in change in a-Ge contact properties. In this chapter, a major focus will be the discussion of electrical and spectroscopic measurements carried out for a-Ge contact Ge detectors at the cryogenic temperatures.

4.1 Detector Characterization in a Vacuum Cryostat at 77 K

4.1.1 *Detector Characterization Setup at USD*

The Ge detectors fabricated using home-grown crystals at USD were tested in a vacuum cryostat. The schematic representation of the detector characterization set up at USD is shown in Figure 4.1. The electrode at the bottom is connected to the indium foil and one at the top electrode to the gold-plated pogo pin. The current setup at USD allows us to bias the detector through its bottom contact and signal and leakage current read-out from the top contact. After the detector was loaded inside the cryostat, the connection between the high voltage supply and signal cable was tested using a multimeter. At room temperature, the resistance of the Ge detector is measured to be in

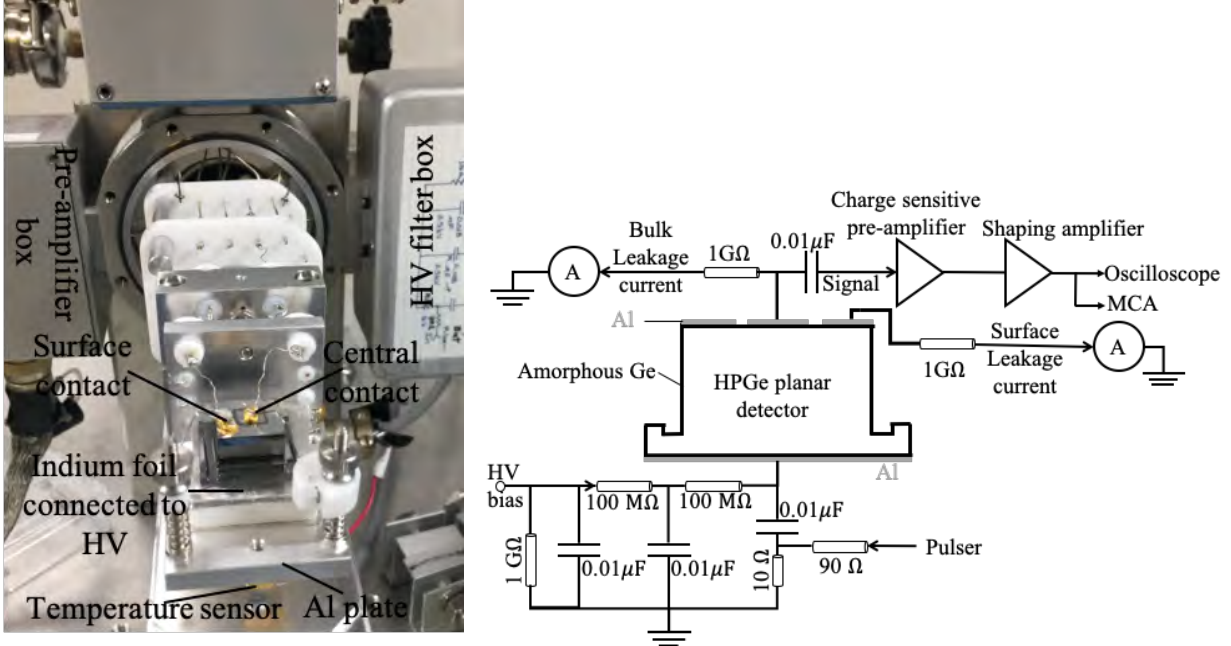


FIGURE 4.1: Shown is the detector characterization setup at USD. Left: internal structure of vacuum cryostat; Right: schematic representation of electronic circuit for detector characterization.

the range of a few ten's of Ω to several $\text{k}\Omega$. If the connection between the high-voltage cable and the signal cable shows any resistance value, it signifies the connections to the detector are successful. The next step is to vacuum the cryostat down to the order of 10^{-6} Bar before adding liquid nitrogen in the chicken feeder style dewar. The vacuum cryostat is equipped with a heater and a temperature sensor which are placed at the bottom of the Al stage. The minimum temperature that was attained in the vacuum cryostat was ~ 78 K. A LakeShore temperature controller was used to monitor and control the temperature of the detector. Electrical measurements were carried out an hour later to provide time for the detector to be in thermal equilibrium with the Al stage. The leakage current, and the transient signals are recorded from the single top contact. This is possible since the leakage current is a d.c. signal and it could not pass through the $0.01\mu\text{F}$ capacitor before the charge-sensitive pre-amplifier, but the $1\text{G}\Omega$ resistor before the ammeter, and the transient signals, a.c. signals, could not pass the resistor, but the capacitor. Transient signals were amplified by the charge-sensitive pre-amplifier.

4.1.2 Electrical Characterization

I-V Characteristics

It is desirable to have a low leakage current for the radiation detectors so energy resolution of the detector is not compromised. Leakage current generates shot noise and affects the energy resolution of the detector. Since the Ge has a relatively small band gap (0.67 eV at room temperature), it needs to be cooled down to less than 140 K to minimize the thermal generation of charge carriers.

The leakage current was measured with the combination of a trans-impedance amplifier and a multimeter. The precision of the leakage current measurement from our current setup is 0.1 pA. Since the Ge detector works similar to a capacitor, the leakage current increases initially for several seconds, then gradually decreases and becomes constant. The leakage current data was taken after a 2 minutes stabilizing time. A sudden increase of leakage current can damage the pre-amplifier. As can be seen in Figure 4.1 to measure the leakage current, a pre-amplifier is not needed since the leakage current is a d.c. signal. Hence, to avoid the possible damage to the pre-amplifier it is better to do initial I-V characterization without using a pre-amplifier.

The detector with a guard-ring structure allows the characterization of leakage current as: a) Bulk leakage current (BLC) and b) Surface leakage current (SLC). The fabrication procedure for the guard-ring detector is described in Chapter 3. The main purpose of guard-ring detector fabrication for us was to separately study the bulk leakage and surface leakage current, hence, the information about the contact properties and the surface defects can be extracted. BLC allows us to find the barrier height of the a-Ge contacts and to understand the inhomogeneity of the contacts. A sample guard-ring detector, USD-R02, is shown in Figure 4.6 for illustration. The ring of Al etched away from the top contact allows us to measure the leakage current separately from the two contacts. The BLC is mostly dominated by the charge injection from the top and the bottom contacts which is measured from the central contact. The SLC is the current created by the surface defects and measured from the surface contact. a-Ge has defect states near the Fermi level. Small energy is sufficient to initiate the conduction of carriers through the hopping mechanism which contributes to the SLC [122–124]. The SLC measured from the USD-made detectors is more than the BLC on

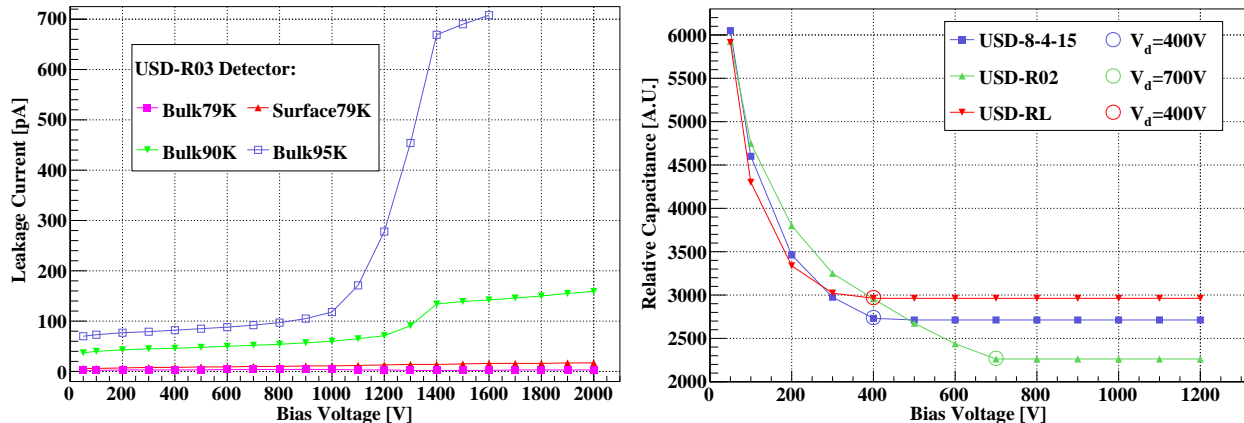


FIGURE 4.2: Shown is the electrical characterization plots obtained at 77 K. Left: the plot of leakage current versus bias voltage for the USD-R03 detector at different temperatures; Right: relative capacitance as a function of bias voltage for three detectors. All three detectors has different net impurity concentrations and thickness.

average and also compare to the pioneers in detector fabrication [24], which signifies that there is still a room for the improvement by making side surfaces smoother. The SLC measured at 79 K, and BLC measured at 79 K, 90 K and 95 K is shown in Figure 4.2. Leakage current measurements can help to determine the full depletion voltage (V_d). As shown in Figure 4.2, the sudden increase in BLC appears around the V_d , ie. ~ 1400 V. The physics of such phenomena is discussed in Section 5.3. A step function can be observed clearly at the higher temperature, however, to see such a step at low temperature, a precise measurement of BLC is necessary. This is primarily because the leakage current is small at low temperatures and the accuracy of the measuring instrument limits the measurement. Leakage current may also change over the first few thermal cycles after fabrication but gradually stabilizes afterward [23]. A thorough study of the leakage currents of the USD detectors for a wide range of temperatures can be found in References [125, 126]. The temperature-dependent and bias voltage-dependent properties of leakage current are discussed in Chapter 5.

C-V Characteristics

C-V characteristics allow us to find out the bias voltage needed to fully deplete the detector. The process of C-V characterization is described as follows: C_d at various bias voltages (V_b) was

recorded. Increasing the V_b applied to the detector, the thickness of the depleted region (d) also increases. Hence, with the increase of V_b , d increases, and C_d goes down. When the detector is free of free charge carriers, fully depleted, the d and detector thickness (D) becomes equal i.e. $d = D$. After that the d cannot increase anymore, C_d becomes a constant. The bias voltage at which the C_d - V_b curve starts to flatten out is known as the full depletion voltage (V_d) of the detector. The measurement process for the C_d is described as follows: First, the step voltage pulses of fixed amplitude (V_p) were injected from a pulse generator into the circuit. The voltage change is converted to charge injection to the detector through the $0.01 \mu\text{F}$ capacitor in between the pulse generator and the detector. The charge-sensitive pre-amplifier converts this change of charges to a voltage pulse (V_o). An oscilloscope was used to identify the magnitude of a voltage pulse. The relation $q = CV$ holds equally well for the Ge detector. For a fixed charge injection, q , the V_o is proportional to C_d . Taking advantage of the identical behavior of V_o - V_b to that of C_d - V_b curve, the V_d can be determined. The C_d - V_b curve for the three detectors is shown in Figure 4.2. The circle on each curve denotes the V_d for that particular detector.

The depleted Ge detector can be assumed as a parallel metal plate capacitor. In a parallel plate capacitor the C_d is anti-proportional to the distance (x) between the plates as shown in Equation 4.1.

$$C_d = \varepsilon A/x, \quad (4.1)$$

where ε is the permittivity of the material between the metal plates.

A variation in V_d for three different planar detectors can be described using the following Equation 4.2. The net impurity concentration ($|N_A - N_D|$) of the crystal is directly proportional to the V_d , and inversely proportional to the square of D of the crystal.

$$|N_A - N_D| = 2\varepsilon V_d/e/D^2, \quad (4.2)$$

where, N_A and N_D are the p and n-type impurity concentrations, respectively, ε is the permittivity of Ge, e is the elementary charge. The $|N_A - N_D|$ calculated using Equation 4.2 can be used to compare the results obtained from the Hall-effect measurement of the crystal sample. Though there

may be some error in determining the V_d , this method is more efficient compared to the Hall-effect measurements. The uncertainty in Hall-effect measurements is discussed in Section 3.3.

Capacitance Measurement

Low-capacitance detector is often preferred since it provides better energy resolution. The method to determine the absolute capacitance of the detector is described below as an example for one of the detectors, USD-RL. The V_d of this detector is 400 V, a negative bias voltage of 1000 V was applied to the bottom of the detector to minimize the charge trapping effects. The absolute capacitance (C) was calculated using Equation 4.3;

$$C = Q/V \tag{4.3}$$

where, $Q = Eq/\epsilon$, E is the energy of the input pulse generated from a pulse generator, $\epsilon = 2.96$ eV is the average energy required to generate one electron-hole pair in Ge at 77 K, and V is the amplitude of the output pulse detected through the oscilloscope. The input pulse generated from the pulse generator is calibrated to the known energy peak of a radioactive source, in this case using 661.7 keV γ from ^{137}Cs , placed on top of the detector. The absolute capacitance calculated for the USD-RL detector using Equation 4.3 is ~ 5.12 pF. The relative capacitance obtained from C-V characteristics was then normalized to get the absolute capacitance value for the lower bias voltage. The plot of absolute capacitance as a function of the applied bias voltage is shown in Figure 4.3. The theoretical calculation of absolute capacitance using Equation 4.1 for the same detector is 4.51 pF. This discrepancy may arise from the uncertainty in the measurement of the contact area and detector thickness, stray capacitance, etc. The absolute capacitance measured for all the detectors fabricated at USD is in the range of 0.4 pF to 6 pF depending on the area of the contacts and thickness of the detector.

4.1.3 Spectroscopy Measurements

The small capacitance of the detector implies a low noise level for the detector and hence better detection threshold can be achieved. A low detection threshold is desirable especially in dark matter

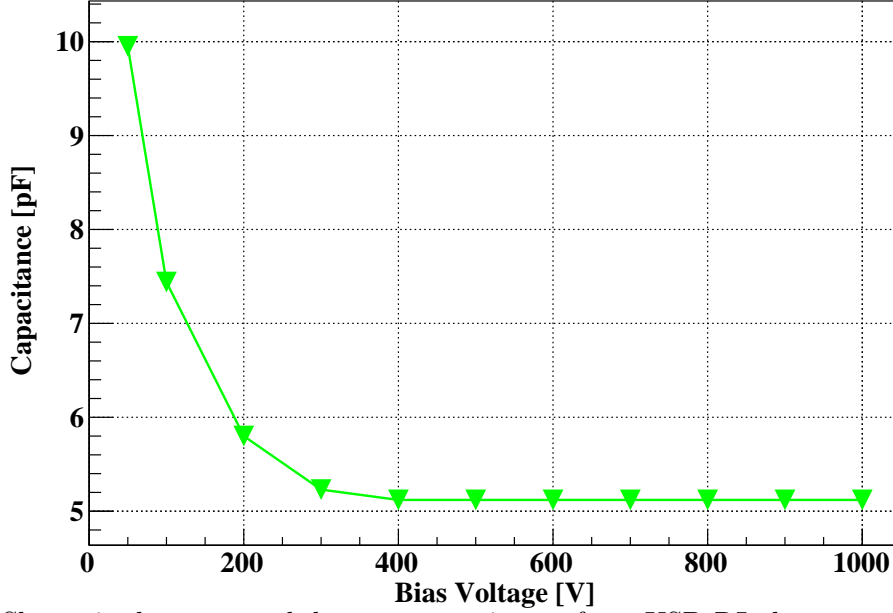


FIGURE 4.3: Shown is the measured detector capacitance for a USD-RL detector as a function of bias voltage. Absolute capacitance of the detector was measured at 1000 V and then the relative capacitance data was normalized to obtain the absolute capacitance for the lower bias voltages.

and neutrino experiments as it increases the sensitivity and physics reach of those experiments. The capacitance of the detector is largely related to the contact geometry. Therefore contact geometry should be optimized keeping in mind the detector can be fully depleted and electric field in all region of the detector is strong enough. High electric field is required in order to obtain the saturation velocity for charge carriers. The rate at which the charge carriers drift through the detector depends on their mobility and the electric field. The magnitude of the electric field determines the charge carrier drift velocity hence the drift time. At the full depletion voltage, some parts of the detector may not have enough electric field and may cause charge trapping. To avoid this, the operation voltage should be much higher than the full depletion voltage. The energy resolution of an HPGe detector depends mainly on the three factors. It is a convolution of the electronic noise ΔE_e , the fluctuation of the number of charge carriers in their creation process ΔE_n , and a component due to incomplete charge collection or trapping of charge carriers ΔE_t :

$$\Delta E^2 = \Delta E_e^2 + \Delta E_n^2 + \Delta E_t^2. \quad (4.4)$$

The pulser signal is injected through a circuit to determine the electronic noise of the setup. The signal is calibrated using the energy peaks obtained from the radioactive source. The resolution of the calibrated pulser peak determines the electronic noise ΔE_e . A γ -ray or X-rays peak should be well resolvable than the pulser peak since there are additional contributions ΔE_n and ΔE_t . Usually, the terms ΔE_n and ΔE_t are entangled together with the energy spectrum. ΔE and ΔE_e can be obtained from the energy spectrum taken for a given detector. Hence, the convolution of two components ΔE_n and ΔE_t is related to the resolution of detector only excluding the electronic noise and is given by

$$\Delta E_d^2 = \Delta E^2 - \Delta E_e^2 \quad (4.5)$$

where $\Delta E_d^2 = \Delta E_n^2 + \Delta E_t^2$. Radioactive sources either Cs-137, with radioactivity of 5.0 μCi , and Am-241, with radioactivity of 1.0 μCi were used to conduct the spectroscopy measurements. The radioactive source was placed outside the cryostat directly facing the top surface of the detector. The energy spectrum shown in figure 4.4 was taken at 79 K with an applied bias voltage of 1700 V in a LBNL cryostat. The full depletion voltages for USD-R08 is 800 V. As discussed earlier, the signals were read out from the top electrode with a combination of charge-sensitive pre-amplifier and shaping amplifier. The shaping time was optimized for 2 μs . The pulser signal amplitude was fixed and it was adjusted far away on the right side of 662 keV peak. The resolution of the γ -ray peak from both sources (Am-241 and Cs-137), ΔE , was always slightly larger than that of the pulser peak, ΔE_e for all the detectors and is shown in Figure 4.4.

4.2 Characterization of a-Ge Contacts Ge Detector Directly Immersed in Cryogenic Liquids

Three mini planar HPGe detectors with a-Ge contacts were used to investigate contact properties at Max-Planck-Institut (MPI) für Physik in Munich. Two of the detectors: USD-RL and USD-R02 were designed at USD, while the detector USD-8-4-15 was designed at LBNL by Mark Amman. The measurements of leakage currents, V_d , and spectroscopy were carried out in a vacuum cryostat at USD before immersing them directly in cryogenic liquids. The dimensions and properties of these detectors are summarized in Table 4.1.

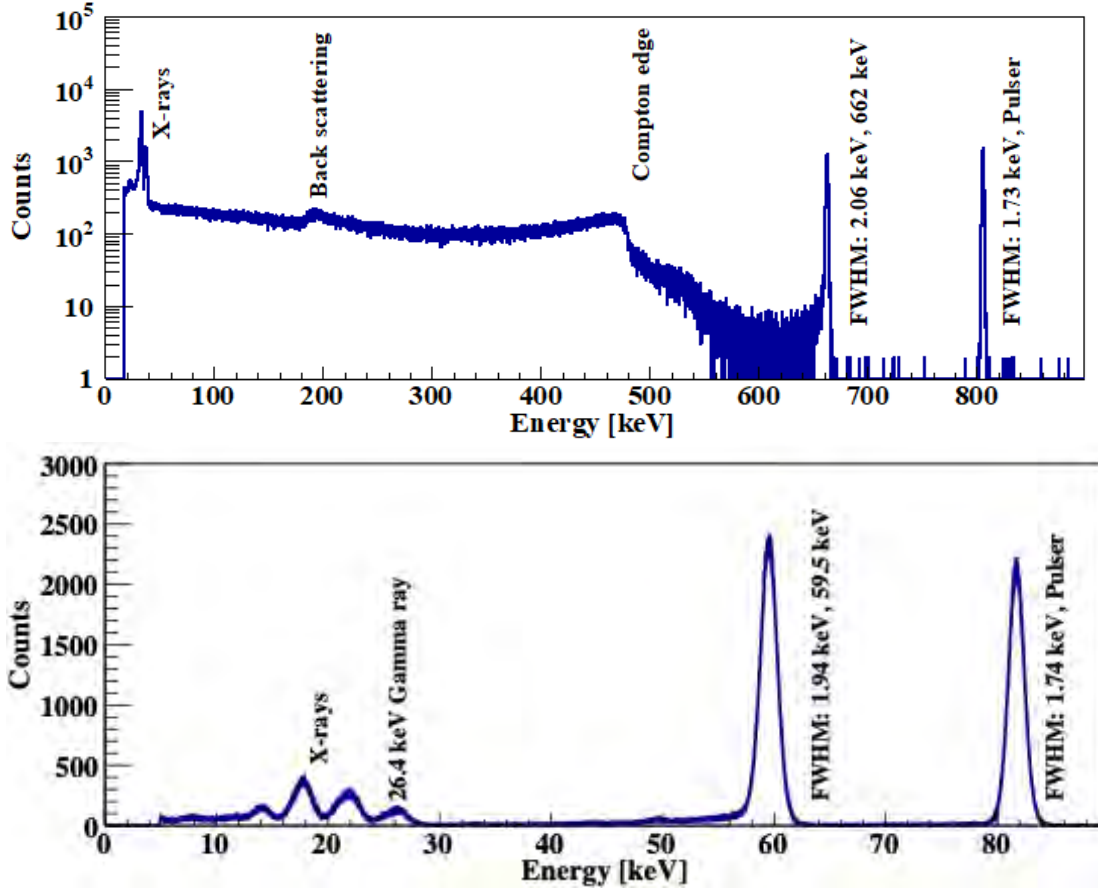


FIGURE 4.4: Shown are the energy spectra obtained for a USD-R08 detector. Top and bottom spectra are obtained from ^{137}Cs and ^{241}Am source, respectively. Both the sources were placed outside of the LBNL cryostat. Pulser determines the electronic noise level.

4.2.1 Detector Characterization Setup at MPI

The discussion about the detector characterization setup for vacuum cryostat at USD is already presented in Section 4.1.1. There are a few variations across different electronic setups which can be seen in Figure 4.5. The measurement of leakage current in the MPI setup was done using a Keithley pico-ammeter which has in-built noise cancellation. The sensitivity of the pico-ammeter is 20 fA. The device allows us to obtain the average value from a certain number of leakage current measurements. The leakage currents of these detectors in different environments at operating voltage, 1200 V are summarized in Table 4.1.

Three USD Ge detectors were operated in a liquid argon cryostat (named Gerdalinen II)

Table 4.1: Shown is the summary of USD detector properties used for the characterization in MPI setup.

Detector	USD-RL	[†] USD-8-4-15	USD-R02
[▷] Impurity/cm ³	6.2×10^9	1.7×10^{10}	2.9×10^{10}
Thickness/cm	1.07	0.70	0.65
Top area/cm ²	1.88×1.79	1.27×1.20	[‡] 0.5×0.5
* V_d /V	400	400	700
[◇] I_{before} /pA	10	1	[‡] 1
[◇] I_{LN_2} /pA	3–5	≤ 0.2	[‡] 1
[◇] I_{LAr} /pA	210–234	10	[‡] 25
[◇] I_{after} /pA	7	\oplus_-	[‡] 3
• $\Delta E_{\text{pulser}}^{\text{before}}$ /keV	1.93	1.28	1.67
• ΔE^{before} /keV	2.55	1.66	2.16
• $\Delta E_{\text{pulser}}^{\text{LN}_2}$ /keV	5.63	5.64	\odot -
• ΔE^{LN_2} /keV	5.92	5.81	\odot -
• $\Delta E_{\text{pulser}}^{\text{LAr}}$ /keV	5.44	4.95	5.42
• ΔE^{LAr} /keV	5.91	5.03	6.01
• $\Delta E_{\text{pulser}}^{\text{after}}$ /keV	1.10	\oplus_-	2.00
• ΔE^{after} /keV	1.74	\oplus_-	2.98

[▷] Net impurity concentration calculated using Eq. 4.2.

[†] Made by Mark Amman at LBNL in 2015.

[‡] Values are for the central contact.

* V_d : Depletion voltage.

[◇] I : leakage current measured at 1200 V in LN₂, LAr, and vacuum before/after the MPI deployment

• ΔE : energy resolutions of the pulser and the 662 keV γ -ray peak measured at 1200 V in LN₂, LAr and vacuum before/after the MPI deployment.

\oplus No measurement at USD after its deployment at MPI since the detector was left at MPI.

\odot No measurement since the ¹³⁷Cs source was temporarily unavailable.

developed by the Germanium-Detector (GeDet) group at MPI [127]. An artistic view of this cryostat is shown in Figure 4.5. The cryostat was used to operate USD detectors in LN₂ and LAr. The top flange of Gerdalinen II could be opened up for the installation of the detectors. Detector holders and the central part of the infrared (IR) shield are attached to a vertical stainless steel bar, which is fixed to the top flange. The assembly is lifted together with the top flange.

For the operation of the USD detectors, a simple PTFE stage was made and mounted to the lowest position on the vertical bar as shown in Figure 4.6. An indium foil was pressed on top of the stage using two PTFE bars. A rigid high voltage (HV) cable went through the vertical PTFE

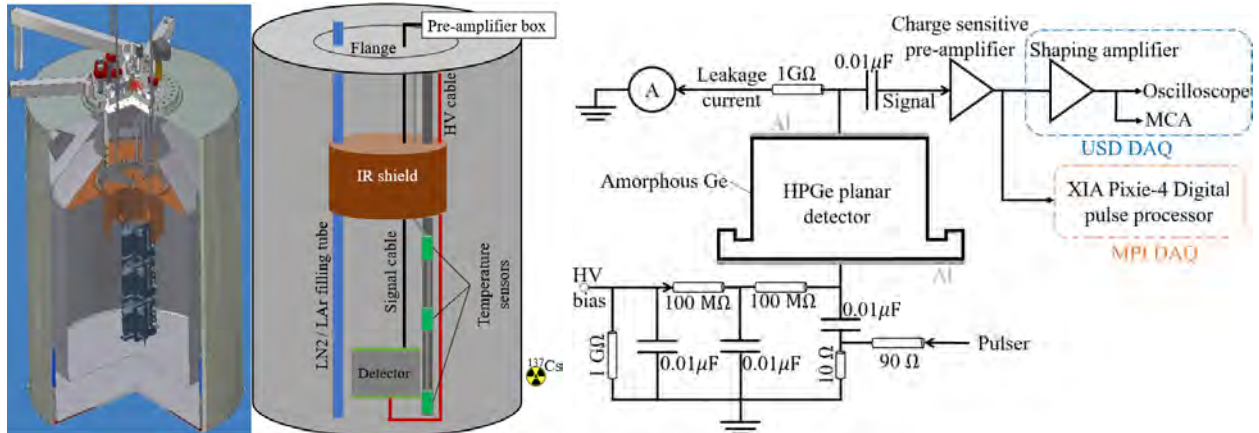


FIGURE 4.5: Left: technical drawing of the MPI cryostat; Middle: schematics of its internal wiring; Right: schematics of electronic circuit for the detector characterization.

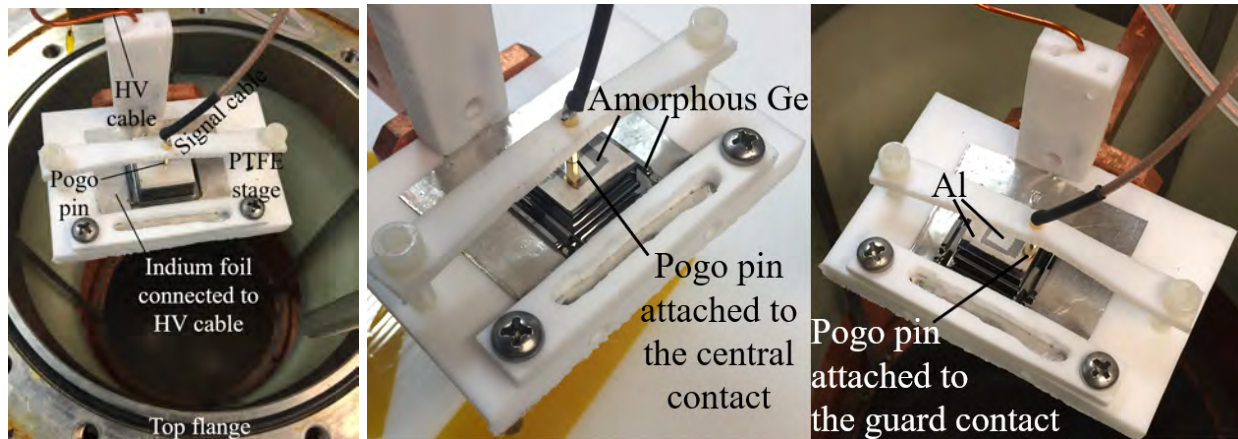


FIGURE 4.6: Left: detector to be lowered into the MPI cryostat; Right: two different contact schemes of the guard-ring detector USD-R02 in the MPI cryostat.

bar and was pushed tightly against the indium foil to provide the bias voltage. The detector was placed on top of the indium foil. A pogo pin connected to the signal cable was pressed lightly on the top surface of the detector. Three PT100 temperature sensors were mounted along the stainless steel bar. The lowest sensor was slightly below the bottom of the detector. The middle one was a few centimeters above the detector. The top one was close to the IR shield. They were used to monitor the liquid level in the cryostat and temperature of the detector. The internal wiring scheme is shown in Figure 4.5.

Safe procedures were in place to fill and empty Gerdalinen II primarily to avoid any frosting

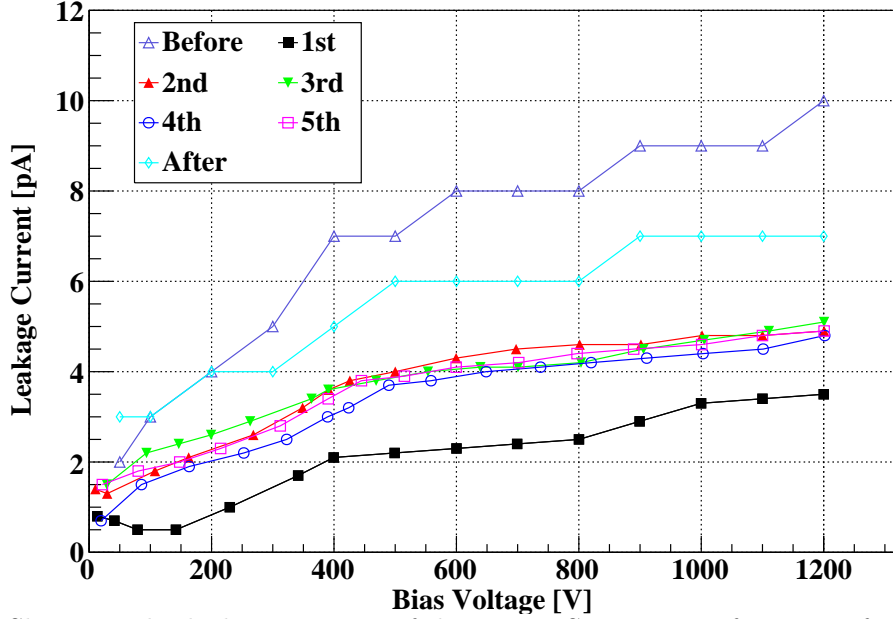


FIGURE 4.7: Shown is the leakage current of detector USD-RL as a function of its bias voltage in LN₂, except for the “Before” and “After” data sets, which were measured in vacuum at USD before and after the MPI deployment, respectively. The numbers denote thermal cycles in LN₂.

of the detectors. The Gerdalinen II cryostat was filled with liquid nitrogen or liquid argon after vacuuming it down. Cryogenic liquid was pump out of the cryostat and detector was warmed upto the room temperature using dry nitrogen gas, before performing another thermal cycle or when taking the detector out from the cryostat.

4.2.2 Detector Operation in Liquid Nitrogen

The first operation of the detectors was carried out in LN₂. Measurements were done in the leakage current and the relative capacitance as functions of bias voltage, and the energy resolution of the 661.7 keV γ -ray peak from a collimated 5 MBq ¹³⁷Cs source at 1200 V. Figures 4.7, 4.8 and 4.9 show the leakage currents of the three detectors as functions of their bias voltages after each thermal cycle in LN₂. For reference, data taken in the vacuum cryostat at USD before and after the MPI deployment are plotted in the same figure. Each data point was recorded a few tens of seconds after a new bias voltage was applied when the reading stabilized.

The leakage current of detector USD-RL measured during the first cooling cycle was 3.5 pA at 1200 V, shown as the last point in the lowest curve in Figure 4.7. Detector was monitored after

the measurement, a slow steady increase in the leakage current was observed over time. Such a slow increase of the leakage current was not observed in other detectors in these studies. It might be due to a gradual development of a small leakage channel on the side surface of the detector. After about an hour, the leakage current stabilized at 5.1 pA. After that the leakage current was found to be very stable over five thermal cycles. 5 pA current was observed at 1200 V. The data sets “before” and “after” represent the measurements before and after the MPI deployment in the cryostat. Measurement values are slightly higher than those measured in LN₂. Higher values in this case may be attributed to the temperature of the detectors in the vacuum cryostat being a few degrees higher than the LN₂ temperature. Leakage current increases with temperature [122, 128]. However, there was no significant change of the leakage current for detector USD-RL measured in different thermal cycles and environments. All current values were below 10 pA up to 1200 V.

As shown in Figure 4.8, the leakage current of detector USD-8-4-15 was approximately 1 pA in both environments, except for the data set measured during the first cool down when leakage current increased rapidly above 1500 V. One possible explanation is that some dust attached itself to the surface of this detector during the transport of the detector from USD to MPI. The dust created a surface leakage channel, which was washed or blown off from the surface in the first cooling cycle; following the removal of the leakage channel, the detector behaved normally.

Only one read-out channel was established in the MPI cryostat. The central and the guard contacts on the top surface of detector USD-R02 were connected to the channel through a pogo pin one at a time, while other contact was left floating as shown in Figure 4.6. However, both contacts were read out at the same time in the vacuum cryostat at USD.

As shown in Figure 4.9, the leakage currents of USD-R02 were mostly below 5 pA for different contacts, environments and thermal cycles. However, the bulk leakage current measured at USD after the MPI deployment were higher possibly due to damage to the detector surface during the shipment; a small scratch was observed on its top surface.

The “capacitance” versus bias voltage curves measured in LN₂ were almost identical to those measured in the vacuum. The V_d determined in the measurement were the same as those determined at USD. This was expected, the V_d is determined by the impurity level of the crystal and is not

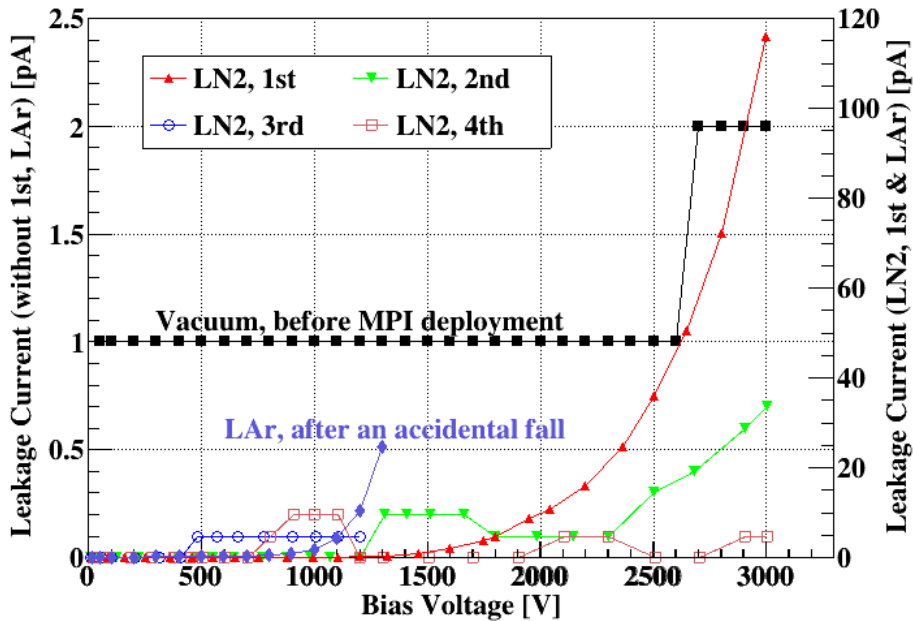


FIGURE 4.8: Shown is the leakage current of detector USD-8-4-15 as a function of its bias voltage in various environments. The numbers in the legend denote thermal cycles in LN₂. The scale for the first cycle in LN₂ and the LAr measurement is on the right.

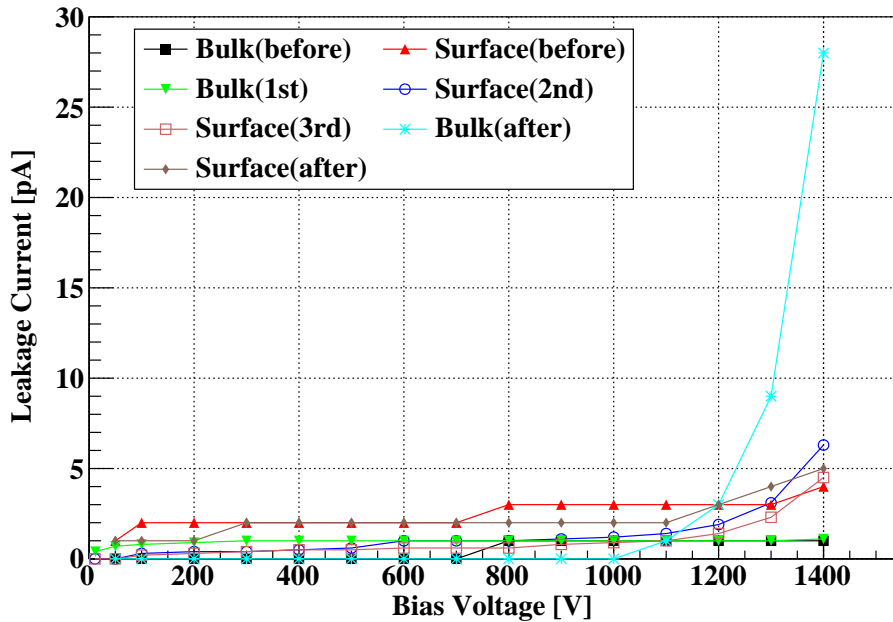


FIGURE 4.9: Leakage currents of detector USD-R02 versus its bias voltage in LN₂, except for the data sets marked with “before” and ”after”, which were measured in the vacuum cryostat at USD before and after the MPI deployment. The bulk leakage currents were measured through the central contact. The surface leakage currents were measured through the guard contact.

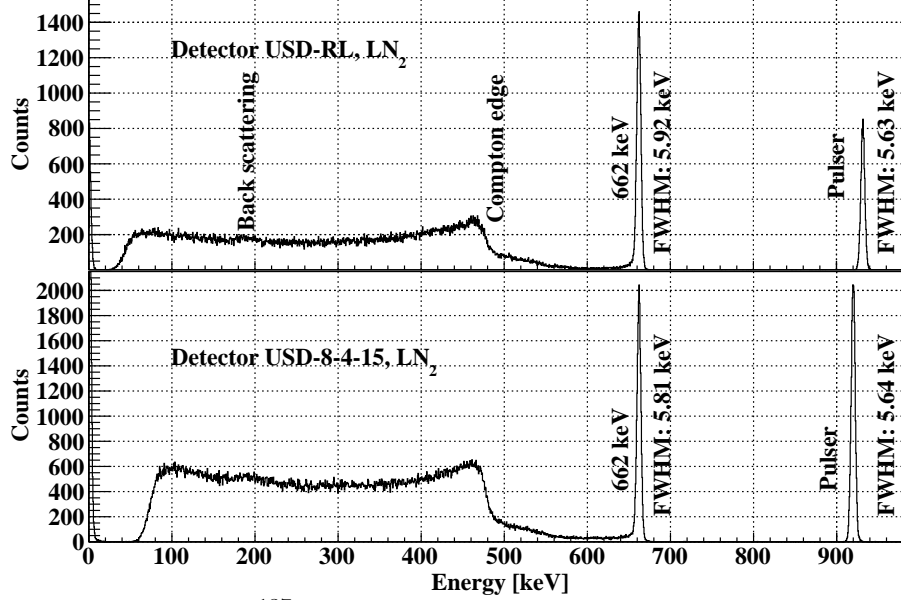


FIGURE 4.10: Energy spectra of ^{137}Cs taken in LN_2 . No spectrum was taken with USD-R02 since the source was temporarily unavailable for the measurement.

expected to change with the environment at a given temperature.

The energy spectra of ^{137}Cs taken with the detectors in LN_2 are shown in Figure 4.10. The FWHMs of the pulse peaks were about 5.6 keV. Due to the presence of significant noise, the influence of cryogenic liquids on the energy resolution of these detectors couldn't be studied quantitatively. Nevertheless, the spectra measured in LN_2 were very similar to those measured in vacuum shown in Figure 4.14, which proved that these detectors worked as spectroscopic devices in LN_2 .

There was no effort made to optimize the read-out as it was beyond the scope of this initial study. Improvements can be made by moving the front-end jFET from the pre-amplifier board to somewhere inside the cryostat, a few centimeters above the liquid level. This reduces the signal cable length and helps achieve an optimized operating temperature of the jFET. This and other important measures will be taken in the future to reduce the impact of electronic noise.

4.2.3 Detector Operation in Liquid Argon

Similar measurements as discussed above were repeated with the same detectors in LAr using the same cryostat at the MPI. Figures 4.8, 4.11 and 4.12 show the leakage currents of the three detectors as functions of their bias voltages after each thermal cycle in LAr. For reference, data sets taken

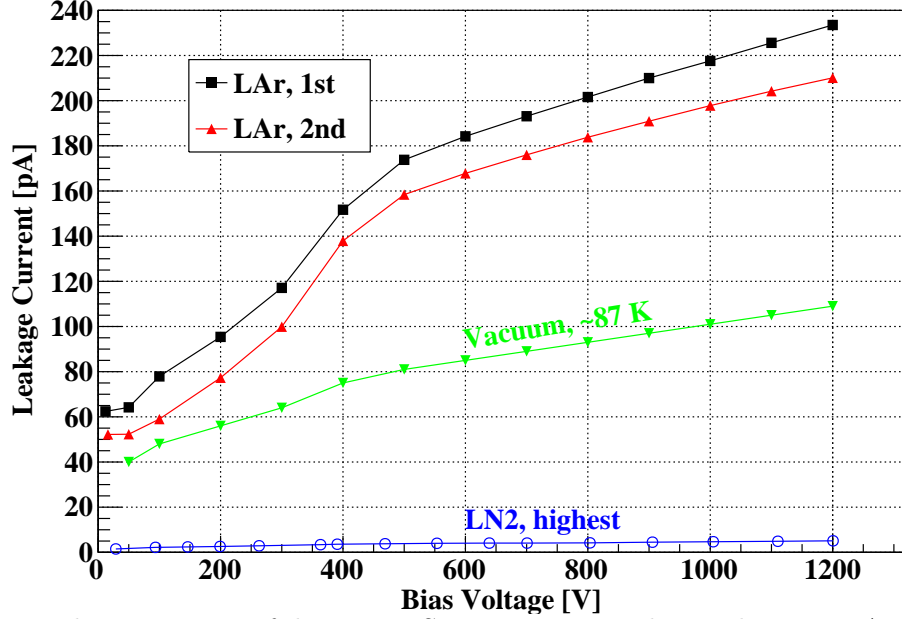


FIGURE 4.11: Leakage currents of detector USD-RL versus its bias voltage in LAr. The numbers denote individual thermal cycles. Also plotted are the highest leakage current measured with the same detector in LN₂ and the one measured in the vacuum cryostat at USD after its deployment at MPI.

at 90 K in the vacuum cryostat at USD before and after the MPI deployment are plotted in the same figure and are labeled as “before” and “after”, respectively.

Detector USD-RL went through two more thermal cycles in LAr. The leakage currents were about 20 times higher than those measured in LN₂.

One operation was carried out with Detector USD-8-4-15 in LAr. Below 800 V, the leakage current was < 1 pA. The observed small leakage current can be attributed to higher quality of the a-Ge surface made at LBNL [23, 24] than at USD [125, 129]. Sharp rise of the leakage current above 800 V was due to damage to the detector when it fell from the PTFE stage during the preparation of the fifth thermal cycle in LN₂. Nonetheless, it still had the best performance compared to the other two detectors.

USD-R02 was operated twice in LAr, first with the central contact connected to the signal cable, and next with guard contact connected to the signal cable. The bulk leakage is a few times higher compared to those in LN₂, while surface leakage is 20 times higher. The leakage current of detector USD-RL in LAr was also about 20 times higher, probably also dominated by surface leakage.

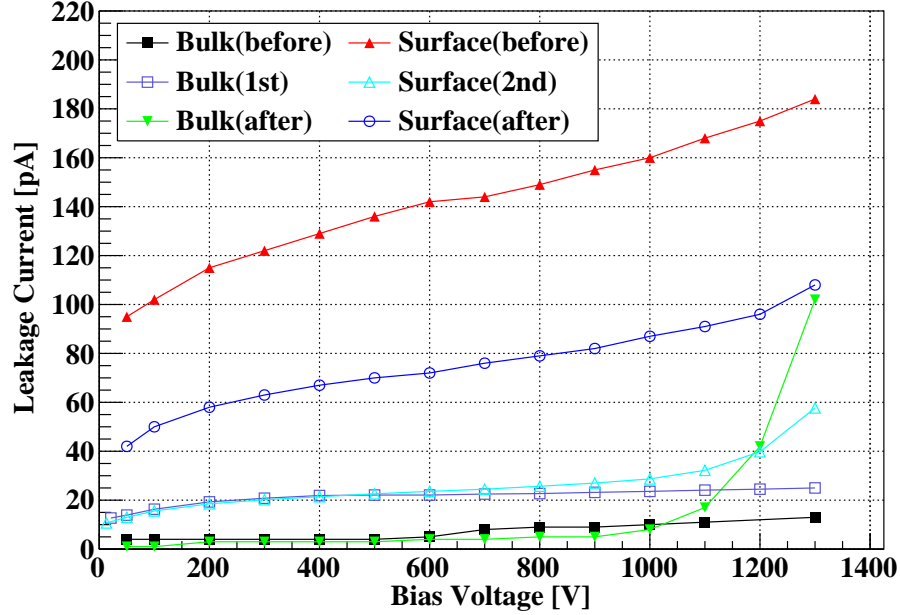


FIGURE 4.12: Leakage currents of detector USD-R02 versus its bias voltages in LAr, except for the ones labeled “before” and “after”, which were measured in the USD vacuum cryostat at 90 K. The numbers denote the thermal cycles in LAr. Bulk leakage currents were measured through the central contact, surface ones were through the guard contact.

At USD, the measurements after the MPI deployment were done at about 90 K instead of 78 K, temperature closer to that of LAr. The leakage current of the central contact of USD-R02 (triangle data points connected with green lines) rose sharply after 1,100 V, which might be due to damage to the detector top surface during the shipment to USD. A small scratch was visible.

The energy spectrum of ^{137}Cs measured with detector USD-RL is shown in Figure 4.13. The detector was biased at 1200 V in LAr. The energy resolution and the noise level were similar to those measured in LN_2 . It hints that, even though the leakage currents in LAr were ~ 20 times larger than those in LN_2 , dominant contribution to the noise was from the read-out system than from the leakage current generated noise.

4.2.4 Characterization in Vacuum Again

The characterization of detectors USD-RL and USD-R02 was done in the vacuum cryostat following their operations in cryogenic liquids. The detector operation was normal even after deployment in MPI. The leakage current measurement results in LN_2 and LAr are shown in Figures 4.7, 4.9, 4.11

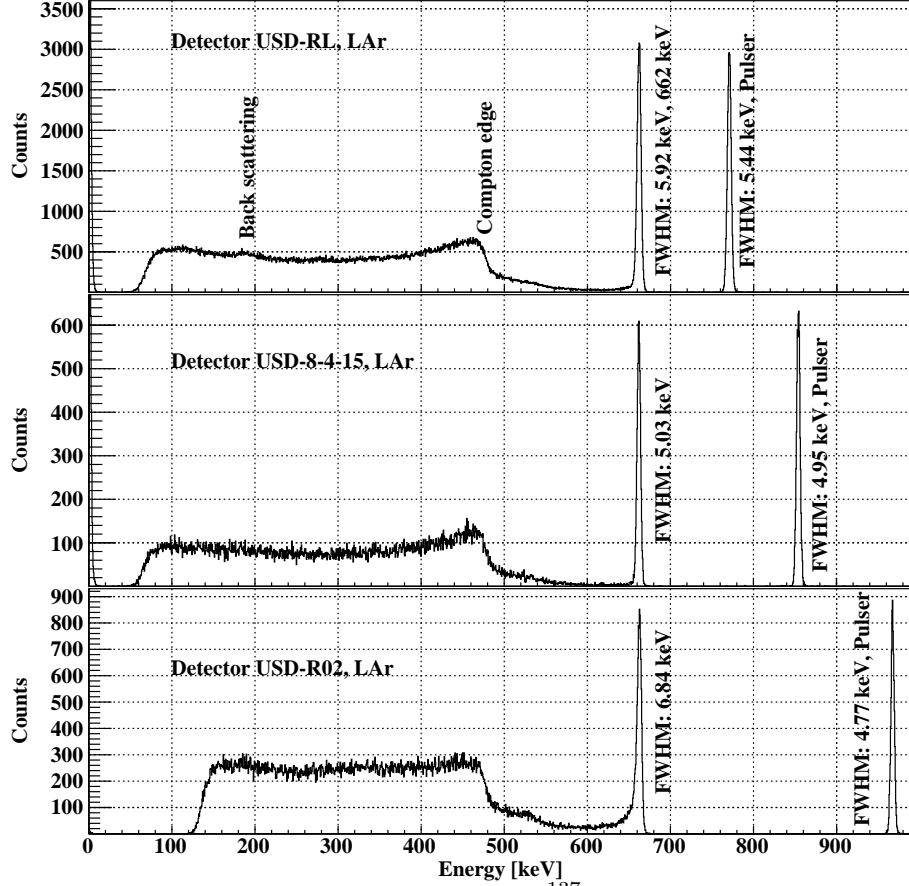


FIGURE 4.13: Energy spectra of ^{137}Cs taken in LAr.

and 4.12 as references. The energy spectrum of ^{137}Cs taken with detector USD-RL (at 1200 V, 78 K in vacuum) is shown in Figure 4.14. There were no further measurements done with the vacuum cryostat at USD for detector USD-8-4-15. It was left at MPI for future investigations. The electronic noise of the MPI setup needs to reduce largely for the quantitative analysis based on the energy resolution of the detector.

4.3 Cross Comparison

4.3.1 Different Detectors in Same Environment

The comparison of the leakage current measurements of the three detectors in LN_2 and LAr is shown in Fig. 4.15 and 4.16. USD-RL exhibited the highest leakage current among the detectors in both environments (LN_2 and LAr), while USD-8-4-15 exhibited the lowest. The side surface leakage

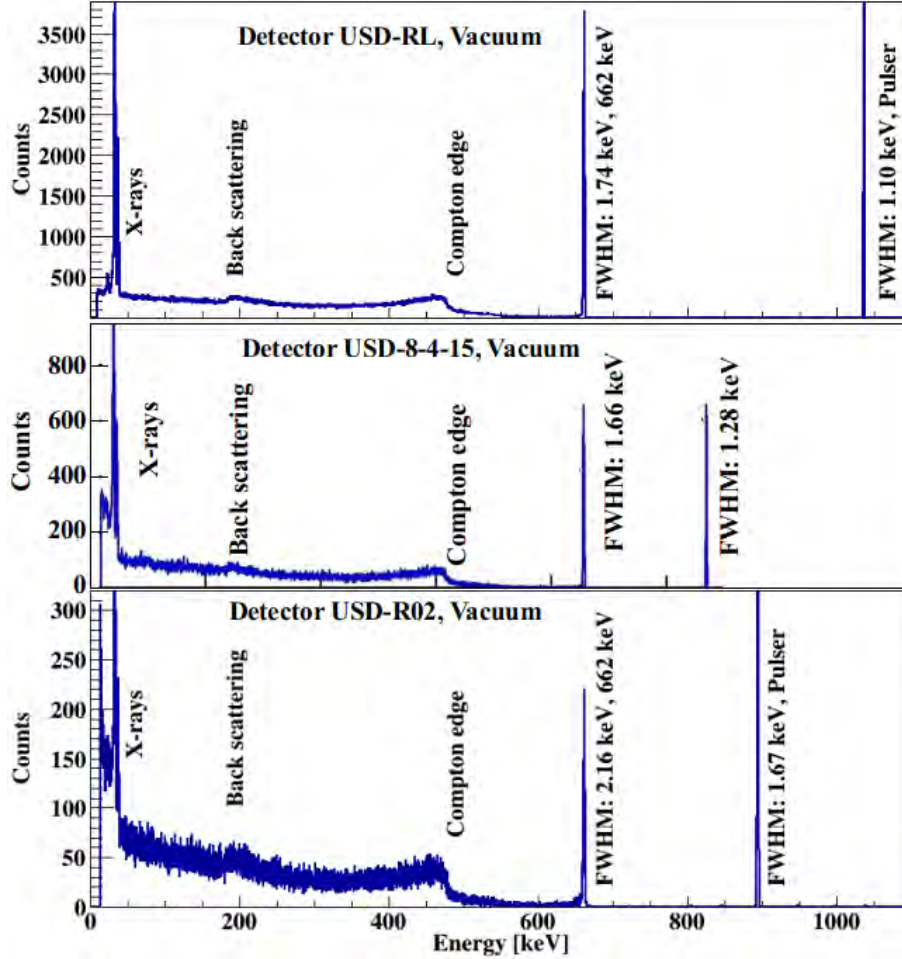


FIGURE 4.14: Energy spectra obtained with the LBNL vacuum cryostat and a ^{137}Cs source outside of the cryostat. Pulsar determines the electronic noise level.

currents of USD-R02 were typically higher than its bulk leakage currents through the central contact around operational voltages in both environments. These results are consistent with the results from the vacuum system at USD with more sample detectors [125, 129]. Some improvements are necessary for the detectors at USD, in particular, the quality of the side surface, to match the performance of the detectors made at LBNL by Mark Amman. Nevertheless, the performance of USD-8-4-15 in cryogenic liquids (LN_2 and LAr) is very encouraging.

4.3.2 Same Detector in Different Environments

Figure 4.17 shows the comparison between the bulk leakage currents through the central contact of USD-R02 measured in various environments (LN_2 , LAr and Vacuum). Leakage current from the

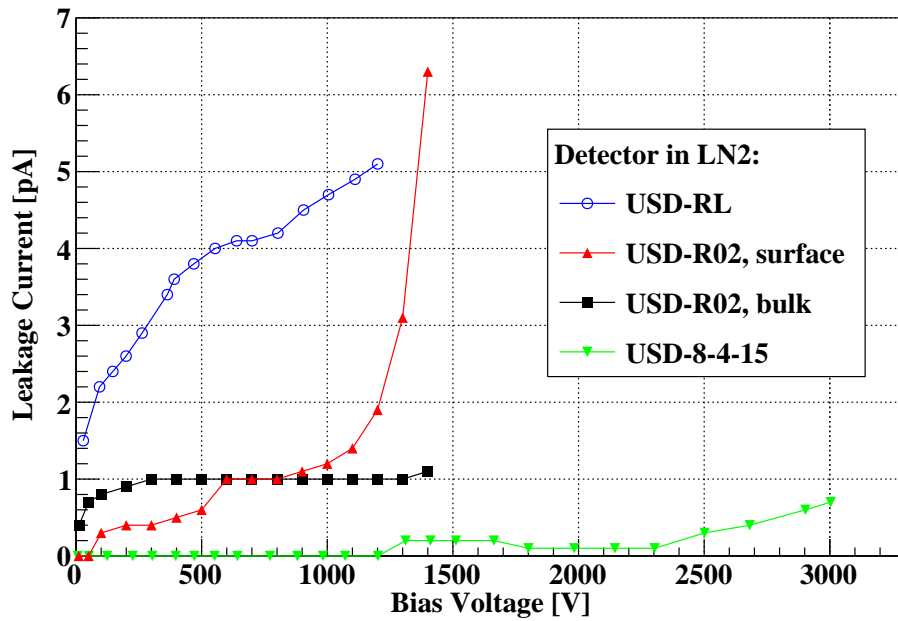


FIGURE 4.15: Highest leakage currents of the three detectors measured in LN₂.

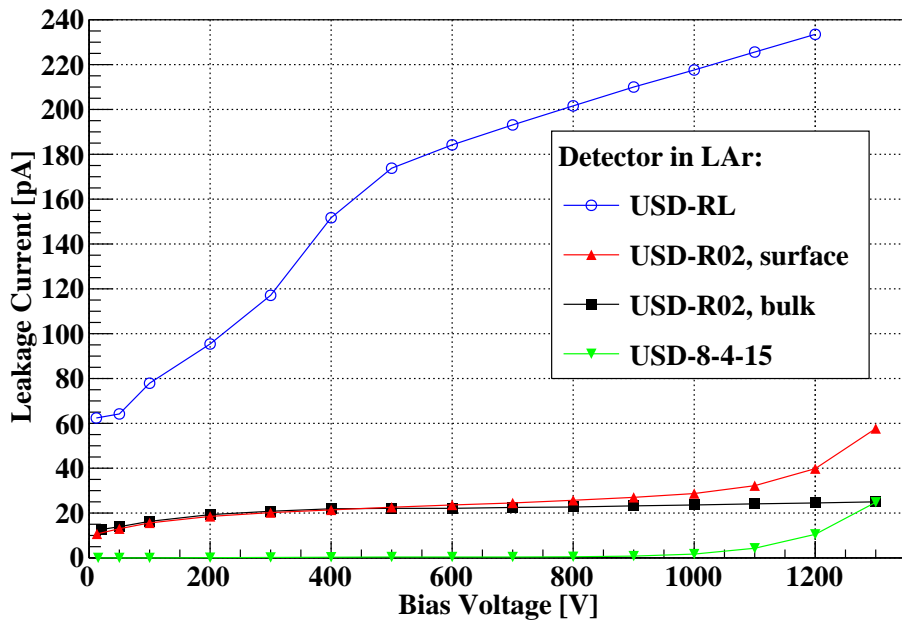


FIGURE 4.16: Highest leakage currents of the three detectors measured in LAr.

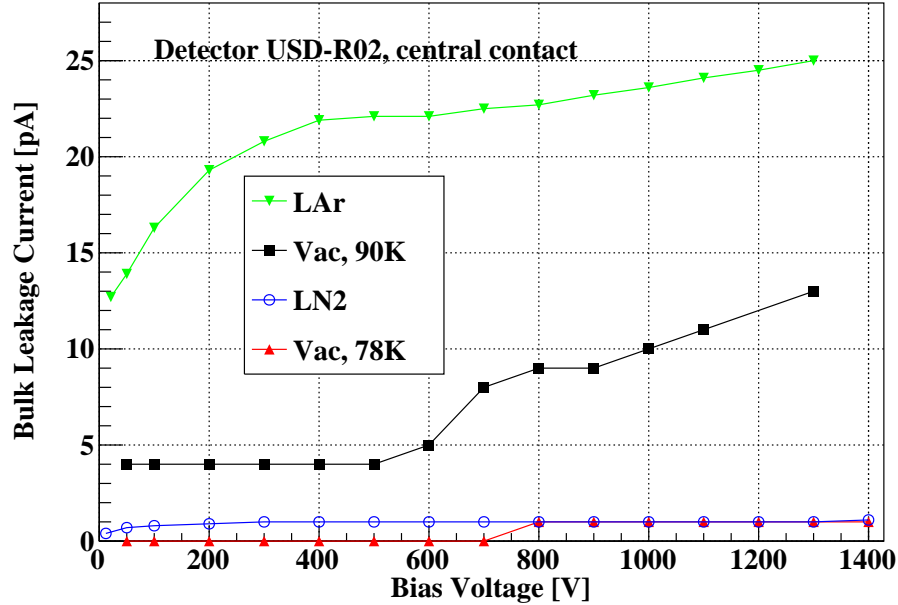


FIGURE 4.17: Largest leakage currents of detector USD-R02 in various environments through its central contact.

side surface was significantly minimized in those measurements. The magnitude of leakage current increased with an increase in the temperatures. Such temperature dependence is well-documented in the literature [23, 122, 126, 128, 130–132].

Differences between the LAr and vacuum measurements at similar temperatures may have two possible explanations. First, LAr may have decreased the charge-carrier blocking capability of the amorphous germanium contact. Second, it took longer for surface property to stabilize for USD-R02. A slow decrease of leakage currents over time has also been observed for LBNL detectors as well [23].

The leakage current measured in vacuum at around 78 K was found to be lower than in LN₂ below 800 V. However, it should be emphasized here that those measurements were done with two different sets of equipments. When precision of the equipments is accounted for, the results are consistent.

Leakage currents of USD-8-4-15 in various environments are compared with each other in Figure 4.8. Accounting for the scratch effects that were the results of the accidental fall of the detectors, they were all ≤ 1 pA below 1200 V. The precision of the experimental setup was not enough to

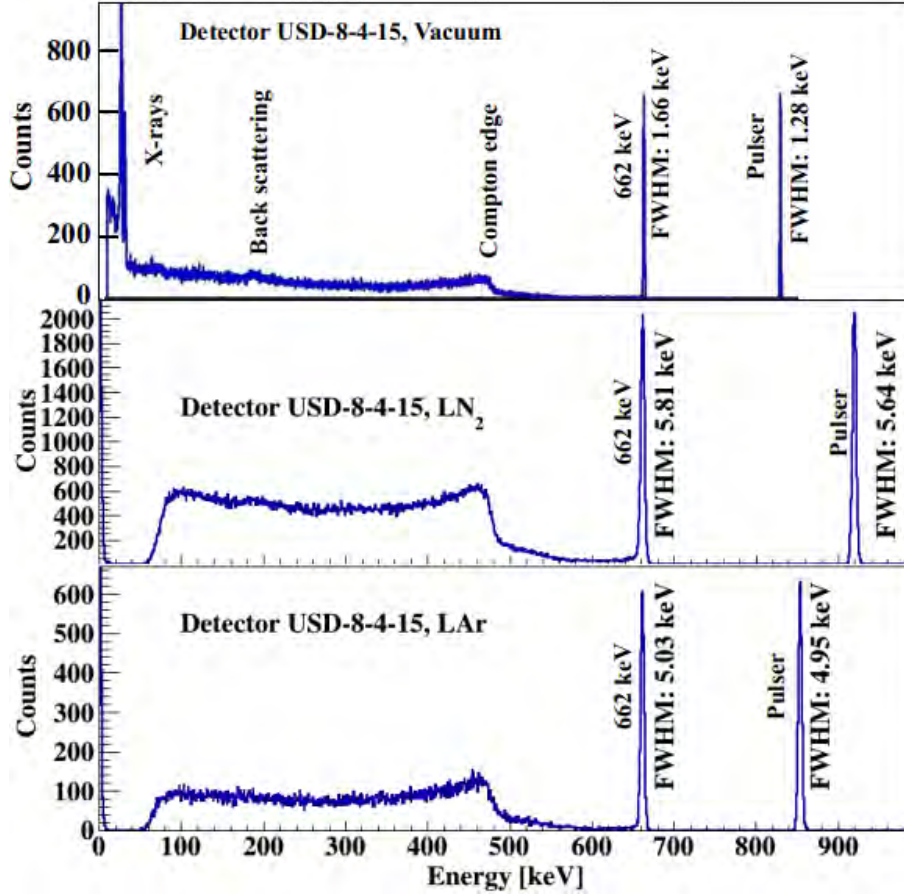


FIGURE 4.18: Energy spectra taken with detector USD-8-4-15 in various environments.

tell the subtle difference at that level.

Energy spectra taken with USD-8-4-15 in various environments are plotted again in Figure 4.18. Pulser peaks are wider in the spectra for LN₂ and LAr system compared to that in vacuum. The reason behind that is the dominant contribution of the electronic noise from the read-out system in smearing the γ -ray peaks. Large noise prevented a meaningful extraction of the intrinsic resolution of the detector from these measurements.

A high energy threshold was set for the measurements in LN₂ and LAr to maintain a reasonable trigger rate. No X-ray lines from the ¹³⁷Cs source are observed since the detector energy threshold was set higher than the energies of these X-rays. Otherwise, features in the spectra structures are very similar to that taken in the vacuum.

4.4 Detector Characterization at Liquid Helium Temperature

Characterization of HPGe detectors at ~ 77 K provides valuable insight into the type of the detector, and notably the net impurity concentration of the detector. Understanding the response of the charges inside the detector is crucial to applying measures to enhance detector performance. Currently, large-scale experiments that use the HPGe detector are operated at \sim LN₂ or mK temperature. Understanding the detector performance at \sim liquid helium (LHe) temperature is also desirable. Planar Ge detectors having $|N_D - N_A|$ ($6 \times 10^9/cm^3 - 7 \times 10^{10}/cm^3$) were fabricated from the crystal grown at USD and characterized at this temperature. Operating Ge detector at low temperatures has several advantages. The detector has a lower surface and bulk leakage current compared to that of ~ 77 K. Also, a decrease in capacitance at low temperatures results in better energy resolution of the detector. Further, the detector is already depleted at around LHe temperature even without the application of bias voltage hence the complicated geometry of the contacts can be avoided.

4.4.1 Detector Characterization Setup for Liquid Helium Temperature

Detectors that were characterized at LHe temperature were first tested in LBNL cryostat at LN₂ temperature. The information of I-V, C-V, and energy spectroscopy was obtained to confirm that these detectors can be fully depleted, leakage current is within the reasonable limit, and the detector works as a radiation detector. The schematic representation of the detector characterization setup is shown in Figures 4.19 and 4.1. The procedure to load the detector into the Pulse Tube Refrigerator (PTR) is similar to the one into the vacuum cryostat, which is discussed in detail in previous section. Only the difference in setup between the vacuum cryostat and PTR is explained here. The PTR is equipped with a heater that is a little far from the detector stage hence there is a difference in the actual temperature set and the real temperature of the detector. Set temperature and the actual temperature of the detector were calibrated using one temperature sensor (Sensor A) close to the heater and another one (Sensor B) on top of the Ge crystal. The calibration results are shown in Table 4.2. As can be seen in the table difference in the set temperature and crystal temperature

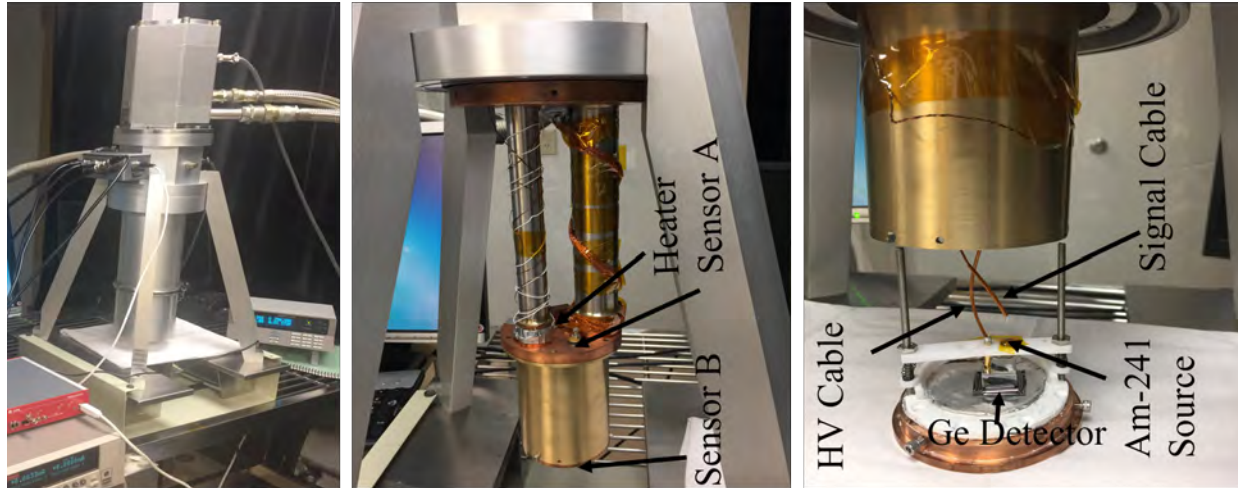


FIGURE 4.19: Shown is the experimental setup for detector characterization at LHe temperature. Left: Enclosed PTR; Middle: detector enclosed with the radiation shield; Right: detector loaded inside the cryostat and ^{241}Am source into the PTFE bar.

is minimum when the temperature is ~ 40 K, since the heater is mounted on the 40 K stage, therefore, control of temperature is better. After that calibration, Sensor B was moved to the bottom of the detector stage to monitor the temperature of the detector closely. The minimum temperature reached in a PTR was ~ 5 K using the He gas compressor which compresses the He gas and LHe flows in and out of the PTR. The heater allows us to warm the temperature of the detector stage up to ~ 80 K with the continuous flow of LHe in the PTR. Electrical measurements were carried out one and half hours later to give time for the detector to come in thermal equilibrium with the copper stage. The electronic setup for the leakage current and signal read-out is similar to the LBNL cryostat. A major difference is the mechanical noise from the motor head of the compressor which is high and the distance between the detector to the pre-amplifier is large. As a result, the electrical noise obtained for this setup is ~ 20 times higher (comparing the lowest noise achieved in two setups) than the LBNL setup.

4.4.2 *I-V Characteristics*

Leakage current measurements were carried out for the USD-R02 detector at LHe temperature. This is discussed in conclusion section of Chapter 5. Since the current setup allows us to measure

Table 4.2: Shown is the set temperature and actual temperature of the crystal.

Set Temperature (K)	Crystal Temperature (K)	Difference (K)
80	80.89	0.89
60	60.60	0.60
40	40.35	0.35
20	20.36	0.36
15	15.85	0.85
12	12.94	0.94
10	11.02	1.02
8	9.06	1.06
6.5	7.63	1.13
5.5	6.76	1.26
5	6.39	1.39
4	5.73	1.73
3.5	5.46	1.96
2.9	5.24	2.34

the leakage current from only one contact, no quantitative measurements of leakage currents were done for the other detectors. However, the leakage current was closely monitored for each detector while taking the energy spectrum. The leakage currents were found lower than the one obtained for LN₂ temperature. Based on our prediction from the barrier height and inhomogeneity of the a-Ge and crystalline Ge interface (Chapter 5), injection leakage current is temperature-dependent and so largely suppressed (negligible). The observed leakage currents for a detector without a guard-ring structure hints that the surface leakage current decreases < 50 percent compared to LN₂ temperature.

4.4.3 C-V Characteristics

C-V characteristics at ~ 77 K are presented in greater detail in Section 4.1.2. A similar process was repeated to determine the V_d at different temperatures. A pulse of known magnitude was injected through the electronic circuit and the output pulse height was recorded. At first, the detector was warmed using a heater from the LHe temperature to a set temperature of 80 K. Relative capacitance as a function of bias voltage was also recorded. As in the previous measurements carried out in an LBNL cryostat, the USD-R11 detector fully depletes at 500 V, we observed the same characteristics. Then the temperature of the detector was lowered and set to 60 K, 40 K,

20 K, 15 K, 12 K, 10 K, 8 K, 6.5 K, 5 K, and 2.1 K (the minimum one). The detector was given enough time to neutralize after each measurement placing the radioactive source outside of the PTR. For each temperature, similar C-V characteristics were repeated. The results obtained from the C-V characteristics are described in detail in Chapter 6.

4.4.4 Energy Spectroscopy

^{241}Am source was placed on the PTFE bar directly on the top of Ge detector to study the detector performance. As discussed earlier, electronic noise level was high so quantitative analysis based on the energy resolution of the detector was not possible. A typical energy spectrum obtained from the ^{241}Am source is shown in Figure 4.20. Charge trapping phenomena was studied using an α and γ sources separately. This is discussed in detail in Chapter 6.

4.5 Conclusion and Outlook

The operation of HPGe detectors with thin a-Ge contacts directly in LN_2 and LAr has been demonstrated experimentally for the first time. Three mini planar detectors with such contacts made at LBNL and USD using USD HPGe crystals, despite long-distance transportation of the detectors, and multiple thermal cycles in both cryogenic liquids, leakage currents and spectroscopic performance were reasonable. Best detector performance for the leakage currents recorded < 1 pA at bias voltages well above the V_d . Leakage currents in LAr of the other two detectors were much higher than those measured in LN_2 , mainly due to the side surface leakage.

There is a significant difference in the geometric configurations of the tested detectors and PPC detectors used in $0\nu\beta\beta$ decay experiments. As a result, no direct comparison can be made between the leakage currents measured here in LAr and those measured with the detectors used in GERDA [133, 134]. The USD group has fabricated few mini PPC detectors with their entire surfaces covered by a-Ge [135]. There is a plan to operate the detectors in the MPI setup for extended time in the future and investigate detector performance so as to verify the feasibility of such a technique in the detectors used in $0\nu\beta\beta$ decay experiments. In addition, recently built PTR at USD will be crucial to explore the a-Ge contact properties and Ge detector properties at a wide

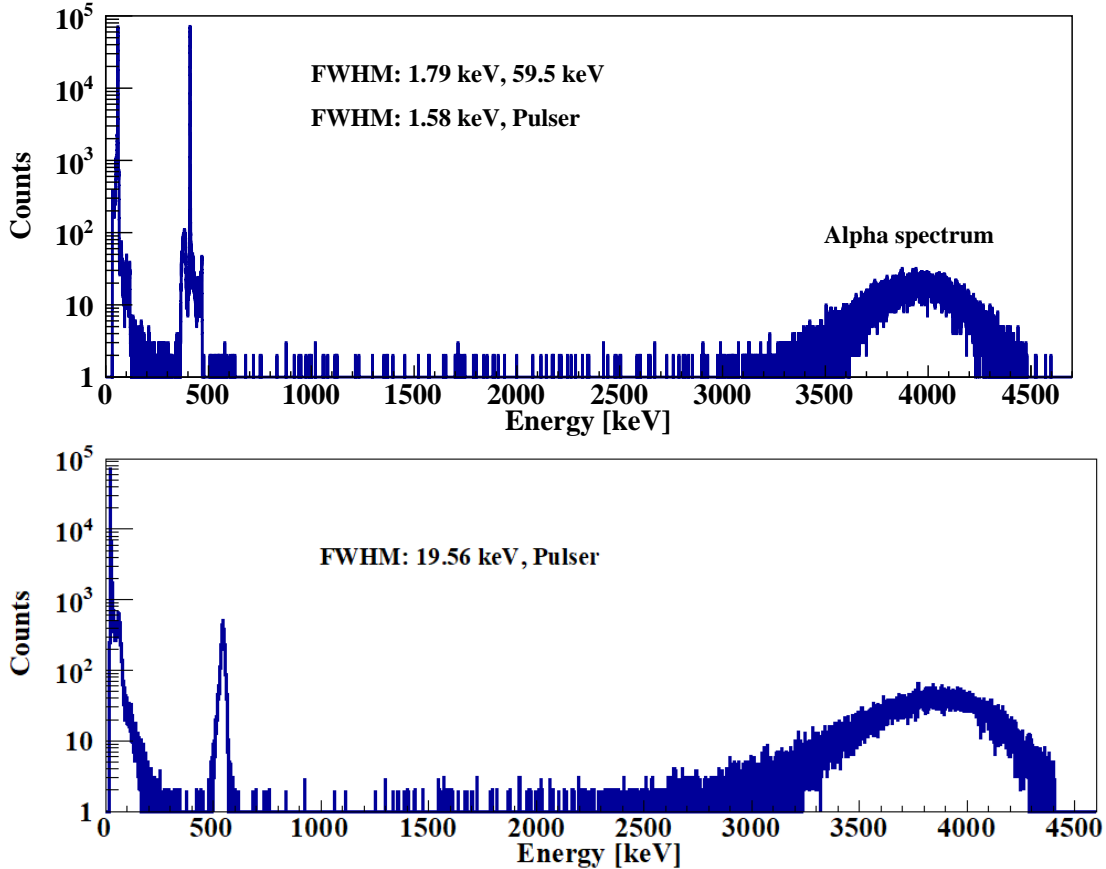


FIGURE 4.20: Shown is the energy spectra obtained for a USD-R09-02 detector. Top and bottom spectra were obtained from ^{241}Am source in a LBNL and PTR, respectively. ^{241}Am source was placed inside the cryostat on both setups. FWHM of pulser in each setup determines the electronic noise level of that setup.

temperature range (5 K - 80 K). Also, the USD group has plan to fabricate large-size Ge detectors using a new Sputtering machine which allows sputtering for larger surface area.

GERDA collaboration has found that the leakage current through the passivated end surfaces of some of their detectors in LAr increased after long-term operation or irradiation with γ -ray sources [133, 134]. It is a matter of interest for larger Ge-detector community to monitor the leakage current through the side surface of a planar detector passivated with a-Ge during long-term operation in LAr. Such measurements will be done with planar detectors with guard contacts allowing in an year gap following fabrication so as to allow a-Ge surfaces to stabilize prior to their operation in LAr.

To summarize, we demonstrated that thin a-Ge contacts passed some preliminary survivability tests in LN₂ and LAr. More dedicated efforts are necessary to verify the feasibility of deploying such a technique for a physical experiment. Collaborative research among institutions with complementary expertise and resources would accelerate the progress in developing such capabilities.

Charge Barrier Height of Amorphous Germanium Contacts

Detectors having low leakage current are preferred for radiation detection. Leakage current is temperature and bias voltage dependent for a particular passivation contact. Choice of passivation layer plays important role in minimizing the leakage current. The ohmic contacts allow charge carrier injection into the Ge detector, hence non-ohmic contacts are required to differentiate between the signal and the noise. In addition, to block the charge carrier injection, contacts formed on the detector should allow the flow of charges from the detector to the contacts. a-Ge is widely used as a passivating material for the Ge crystal, which acts as a charge blocking contact and does not inhibit the collection of charges from the Ge detector. a-Ge lacks the long-range crystalline structure of atoms hence the density of defects is large, whereas, in the crystalline Ge, atoms are perfectly arranged in a diamond-like structure. However, the band gap of both of the structures is the same. Defects near the Fermi level referred to as localized energy states near the Fermi level play a significant role in the electrical conduction through the hopping mechanism. This chapter focuses on the importance of charge blocking (passivation) contacts on the performance of a detector. In addition to that, barrier height calculation using two different techniques as well as inhomogeneity of a-Ge and crystalline Ge heterojunction is discussed.

5.1 Introduction

Leakage current can be measured as SLC and BLC for a guard-ring detector. An example of a guard-ring detector and the characterization setup is shown in Chapter 4. Chapter 4 also discusses the origin of BLC and SLC in a Ge detector. The heterogeneous interface between a-Ge contact and crystalline Ge creates a barrier for charge injection characterized by charge barrier height (CBH). a-Ge has the feature of blocking both types of charge injection, ie. electrons or holes. The primary source of BLC is the injection of charge carriers from a-Ge surface to the bulk of the Ge detector governed by thermionic emission. Thermal ionization of impurities is also another source of BLC. Operating the detector at liquid nitrogen temperature reduces the thermal effect by \sim three orders of magnitude [15] compared to injection from the a-Ge contacts. Therefore, it makes sense to study the CBH of the interface (a-Ge and crystalline Ge) using the measured BLC as a function of bias voltage at a wide temperature range. The BLC is measured through the central contact as shown in Figure 4.1.

Though a Ge detector coated with a-Ge layer needs cryogenic cooling, it still works fine as a radiation detector below temperature 140 K. This makes it possible to investigate the nature of CBH formation at the interface. Since charge carriers in a-Ge are created by the thermionic emission, better understanding of CBH helps in optimizing the process parameters that are used for making the interface. The inhomogeneity of the interface is characterized using the fluctuation of CBH with respect to the temperature. A lot of studies have been done by particle physics and semiconductor community to determine the height of rectifying Schottky contacts as well as for the CBH using different techniques [132, 136–141]. This work focuses on the I-V characteristics of the BLC at different temperatures.

5.2 Experimental Methods

Three guard-ring detectors made from p-type Ge crystals that were grown at the USD were used for the CBH study. All the crystals had uniform surfaces after mechanical lapping, polishing, and chemical etching. The fabrication process is the same for all the detectors used in this study, hence

the uniformity of the a-Ge layer deposition on the detectors is expected. This allows us to study the inhomogeneity of a-Ge layer deposition during the sputtering process that can influence the leakage current. The fabrication process for the guard-ring detector is described in Chapter 3. The detectors used for this study were first tested to find out if the detectors are workable. If contacts are not well fabricated, the leakage current might suddenly increase inhibiting proper understanding of the contact properties. That results from the contact failure. In such cases, detector re-fabrication may be necessary. Therefore, I-V, C-V, and energy spectroscopy measurements were carried out in a liquid nitrogen cryostat. The procedures for the characterizations are discussed in Chapter 4. The properties of the detectors used for this study are summarized in Table 5.2.

5.3 Charge Blocking Contacts

Charge blocking contacts (passivation materials) are necessary to minimize the leakage current in a reverse-biased Ge detector. One of the techniques that are used widely is to make lithium-diffused (n^+) and boron-implanted (p^+) contacts to block hole and electron injection, respectively. The exploration of a-Ge contact is important to overcome the drawbacks of Li-diffused contacts. Bipolarity blocking feature of a-Ge sets aside the need for two different contacts to be formed on a Ge crystal [16]. This study is only related to the a-Ge and crystalline Ge interface. Barrier height and inhomogeneity of the interface can be calculated using the similar theory for other amorphous and crystalline interfaces. For a p-type Ge detector, biased positively from the bottom electrode of the detector, the detector starts to deplete from the bottom. BLC is dominated by hole injection from the bottom contact. The depletion region increases with the increase of bias voltage and reaches the top contact after enough bias voltage is applied. After the detector is fully depleted, electron injection from the top contact also contributes to the BLC. Therefore, near the full depletion voltage, a step-like feature of BLC appears. If it is negatively biased from the bottom electrode for the p-type Ge then the depletion starts from the top. In this case, hole injection occurs for bias voltage less than full depletion voltage and both electron and hole injection after it is fully depleted. For an n-type detector, the cases are exactly opposite ie. p-type detector positively biased, and n-type detector negatively biased on the same surface (top or bottom) show similar

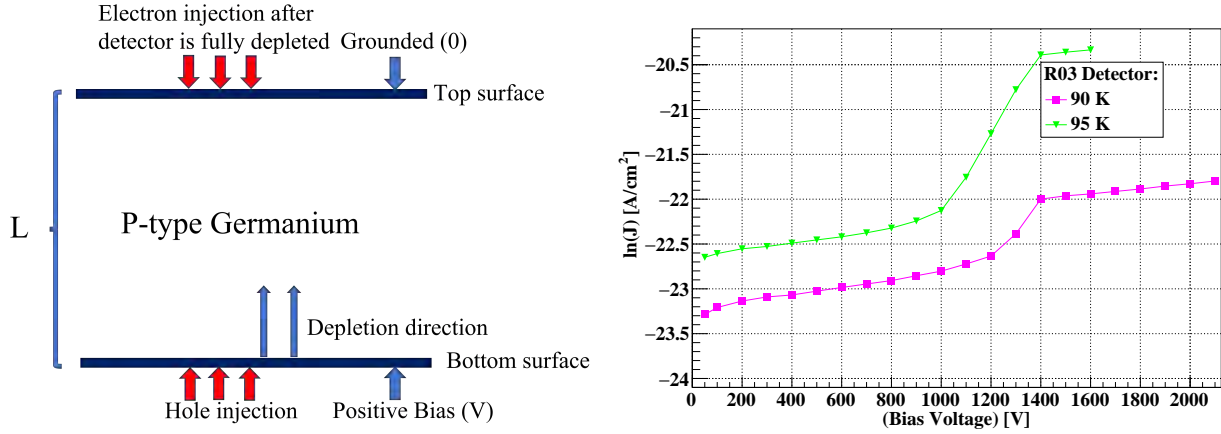


FIGURE 5.1: Left: schematic representation showing the depletion direction, charge injection in a p-type germanium detector with positive bias voltage applied on the bottom electrode of the detector; Right: shown is the variation of logarithmic of bulk leakage current density versus the applied bias voltage for USD-R03 detector at 90 K and 95 K.

charge injection behavior. The schematic representation of injection current behavior is shown in Figure 5.1. Usually, the energy spectroscopy is taken at a bias voltage a few hundred volts higher than the V_d to avoid the trapping of charge carriers. BLC is the sum of electron and hole injection in that case. It is important to understand the contact properties for a better understanding of the leakage current generation and charge collection in a detector. a-Ge contacts made on a Ge crystal are characterized based on: a) the CBH of a-Ge with respect to crystalline Ge; b) the thermal stability of the contacts; c) the ability to withstand high bias voltage without breakdown; and d) the surface inhomogeneity.

5.4 I-V-T Characteristics

Amorphous and crystalline materials form a heterojunction. The model developed by Döhler, Brodsky [122, 130, 131] during the 1970s predicts the leakage current and voltage relationship for the heterojunctions. Schottky successfully applied this model to a-Ge contacts on HPGe detectors [128]. Based on the model, the leakage current is directly proportional to the bias voltage and the temperature [132]. The barrier height of a-Ge contact is calculated based on the current-voltage-temperature (I-V-T) characteristics. The extrapolation of logarithmic current density vs bias voltage ($V \geq 3kT/q$) down to zero bias voltage gives the saturation current density. The satu-

ration current is defined as the current density corresponding to zero bias voltage. The thermionic emission model was originally proposed for the metal-semiconductor junction and later it was also applied for the amorphous-semiconductor interface. This model predicts the current density flowing across the metal-semiconductor interface as;

$$J = J_\infty \exp(-\psi_{0,b}/kT)[1 - \exp(-qV_a/kT)]f(V_a), \quad (5.1)$$

where $f(V_a) = \exp\{[(2q(V_{bi} + V_a) + N/N_f)N/N_f]^{1/2} - N/N_f\}/kT\}$, J is the BLC density, the ratio of BLC to the contact area (area of central contact only), $\psi_{0,b}$ is the barrier height at zero bias voltage, k is the Boltzmann constant, T is temperature, V_{bi} is the built-in voltage, V_a is the applied bias voltage, N is the net impurity concentration, N_f is the density of localized energy states near the Fermi level. Conductivity or resistivity of a-Ge layer can be studied based on N_f .

$J_\infty T^2$ equals $A^* T^2$ in the case of a metal-semiconductor interface. Here, A^* is the effective Richardson constant. Since electric field penetration through the contacts is negligible in an ideal MS contact, the value of $f(V_a)$ is nearly close to 1. It is worth mentioning that $J_\infty T^2$ can be substituted by $J_0 T^2$ [24] for the a-Ge and crystalline Ge junction assuming certain simplistic conditions for the term J_0 . For the simplification of calculation in case of $V_a \gg V_{bi}$, or kT/q , or N/qN_f equation 5.1 reduces to

$$J = J_0 T^2 \exp(-\psi_{0,b}/kT) \exp[(2qV_a N/N_f)^{1/2}/kT] \quad (5.2)$$

$$J = J_0 T^2 \exp(-\psi_{0,b}/kT) \exp[(\frac{\epsilon}{N_f})^{1/2}(V_a - V_d)/t]/kT] \quad (5.3)$$

Equation 5.2 is for a partially-depleted detector contributing BLC either through electron or hole injection, where $\Delta\psi = \sqrt{2qV_a N/N_f}$ and Equation 5.3 is valid after the detector is fully depleted contributing BLC from another type of charge injection, where $\Delta\psi = (\frac{\epsilon}{N_f})^{1/2}(V_a - V_d)/t$; t is the detector thickness. Therefore, total BLC density for a fully depleted detector is given by the sum of Equations 5.2 and 5.3. $\Delta\psi$ is the barrier lowering term which is directly proportional to the applied bias voltage for a given detector and a particular contact. This term varies from one detector to

another since it also depends on the impurity concentration of the crystal and the density of defect states near the Fermi level of an a-Ge. It is desirable to keep the barrier lowering term at a minimum value since it lowers the barrier height of the contacts. A crystal with low $|N_A - N_D|$, and a-Ge contacts that have less density of localized energy states near the Fermi level is ideal. The barrier lowering term is also the indicator of the field penetration that occurs when the bias voltage is applied. Equations 5.2 and 5.3 hold for any bias voltage, only the barrier lowering term is affected by changing the bias voltage. J_0 , called a pre-factor, is treated as a constant for particular contact. J_0 is left as an open parameter in Equations 5.2 and 5.3 and it is calculated from the temperature-dependent I-V measurements [24].

The barrier height needs to be treated as constant with respect to temperature to calculate J_0 from equation 5.2 or equation 5.3. However, researchers in the semiconductor field have done a thorough study of temperature-dependent barrier height for several contact materials and stated that barrier height is a function of temperature [142–148]. Barrier height fluctuation with temperature indicates there exists a barrier inhomogeneity at the interface, in this case for an a-Ge and crystalline Ge interface. First, the barrier height and density of defects of localized states near the Fermi level are calculated assuming the barrier height is constant at two close temperatures (difference of ~ 5 K). Afterwards, fluctuation in barrier height with respect to temperature as a result of the inhomogeneity is considered.

5.4.1 Barrier Height Calculation

As discussed earlier and illustrated in Figure 5.1, for a fully depleted p-type detector negatively (positively) biased from the bottom contact, hole (electron) injection from the top (bottom) contact takes place. Therefore the ψ_0 , J_0 , and N_f for holes from the top contact and the same parameters for electrons from the bottom contact can be determined separately. Following a similar recipe, the parameters can be analyzed for the n-type detector. Taking natural log of Equations 5.2 and 5.3 it can be written as;

$$\ln(J) = \ln(J_0) + 2\ln(T) - \frac{\psi_{0,b}}{kT} + \frac{m_1(V_a)^{1/2}}{kT} \quad (5.4)$$

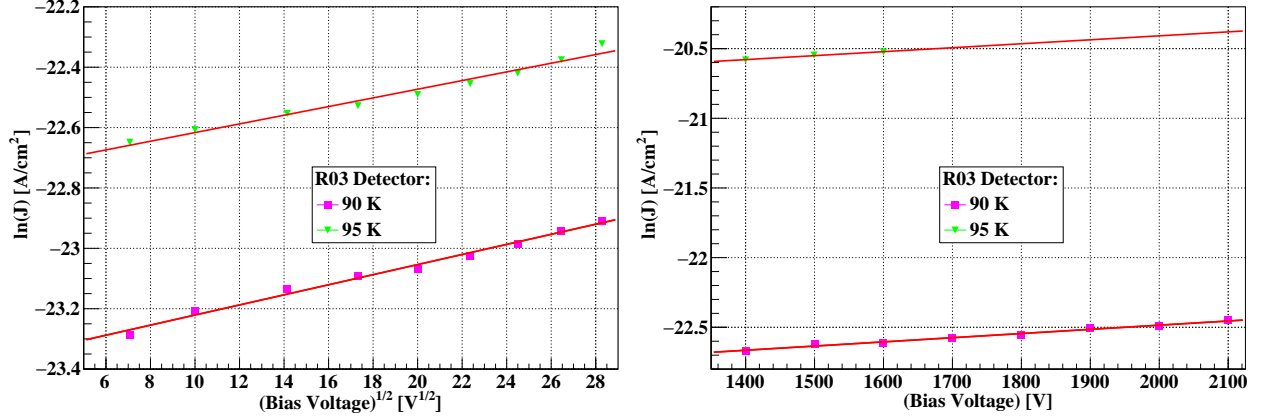


FIGURE 5.2: Shown is the plot of logarithmic of BLC density as a function of its bias voltage for a USD-R03 detector at 90 K and 95 K. Left: shown is the plot for $V_a < V_d$; Right: shown is the plot for $V_a > V_d$

$$\ln(J) = \ln(J_0) + 2\ln(T) - \frac{\psi_{0,b}}{kT} - \frac{m_2 V_d}{kT} + \frac{m_2 V_a}{kT} \quad (5.5)$$

respectively, where $m_1 = \sqrt{2qN/N_f}$ and $m_2 = (\frac{\epsilon}{N_f})^{1/2} \frac{1}{t}$.

For illustration, an analysis is shown for a p-type detector, USD-R03, having V_d 1400 V. Negative bias was applied from the bottom contact, in which case, the hole injection from the top contact for $V_a < V_d$, and electron injection from the bottom contact for $V_a > V_d$ occurs. Hence, after the detector is fully depleted, $V_a > V_d$, both types of charge carriers are injected through the separate contacts. The BLC was extrapolated to higher bias voltage from $I - (V_a)^{1/2}$ plot where $V_a < 800$ V and was subtracted from the total BLC when $V_a > 1400$ V. The purpose of this is to exclude the contribution of hole injection from the top contact while finding out the barrier height for electrons from the bottom contact. $\psi_{0,b}$ for holes and electrons, N_f , J_0 can be found separately for the top and bottom contact if the detector is characterized for both polarities of bias voltage.

The process to find out the above-mentioned parameters is described as follows. BLC density (J) is calculated as BLC per unit contact area. Then natural log of J is plotted against $V^{1/2}$ for $V_a < V_d$ and J against V for $V_a > V_d$ as shown in the Figure 5.2. The analysis for the $V_a < V_d$ and $V_a > V_d$ was done separately since they carry different information (top and bottom contact information). Finally, the data were fitted using a linear function. The slope of the fit gives the

information about N_f in both Equations 5.4 and 5.5. Since there are two unknown parameters (J_0 and $\psi_{0,b}$) on the Y-intercept of the fit, data from two different temperatures is needed. Information obtained from 90 K and 95 K was used to find these parameters.

The electron barrier height, N_f and J_0 obtained from the bottom contact are 0.2917 eV, $2.51 \times 10^{18}/eVcm^3$, $370.64 \text{ A/cm}^2\text{K}^2$ respectively. Similarly, from the top contact hole barrier height, N_f and J_0 obtained are 0.076 eV, $4.52 \times 10^{18}/eVcm^3$, $1.60 \times 10^{-10} \text{ A/cm}^2\text{K}^2$ respectively. The results obtained from the electron injection when a detector is fully depleted are similar to the results published by Amman [24]. However, the parameters extracted from a partially depleted detector using Equation 5.4 are not trustworthy, to extract those parameters detectors need to be fully depleted starting depletion from another side of the detector. For a partially depleted detector, barrier height and J_0 only depend on the difference between two intercepts and not on the slope of $J - V_a^{1/2}$ plot. However, in a fully depleted case barrier height depends on the slope of the $J - V_a$ curve. Therefore, the J_0 is defined as the pre-factor, and the assumption that it depends on the fabrication process is not likely to be true. From the two results mentioned above the pre-factor has a difference of order 10^{-12} . However, the entire recipe used to prepare the crystal and fabrication process were similar. Another possible reason might be the non-uniformity of the electric field caused by the surface channels in a partially depleted detector.

5.4.2 Barrier Inhomogeneity

In this section, the primary focus is to illustrate the relation between the inhomogeneity of the interface and the barrier height. The pre-factor J_0 is assumed same as A^* for this calculation which is given by [128]

$$A^* = \frac{4\pi q m^* k^2}{h^3} \quad (5.6)$$

where q is the electronic charge, m^* is the effective mass of charge carriers, k is the Boltzmann constant, and h is the Planck constant. Plugging in the values on the above Equation 5.6, the value of A^* is $48 \frac{A}{cm^2K^2}$ [136] for a p-type Ge in the $\langle 100 \rangle$ direction. Equations 5.2 and 5.3 can be

re-written as

$$kT \ln(J/A^*T^2) = -\psi_{(0,b)} + m_1 \sqrt{V_a} \quad (5.7)$$

$$kT \ln(J/A^*T^2) = -\psi_{(0,b)} + m_2(V_a - V_d) \quad (5.8)$$

where m_1, m_2 are $\sqrt{2qN/N_f}$ and $(\frac{\epsilon}{N_f})^{1/2} \frac{1}{t}$

The plot in Figure 5.1 shows the variation of the natural log of BLC density as a function of the square root of bias voltage. As can be seen in Figure 5.1, for 10 - 20 bias voltage, the reflection coefficient of charge carriers is dominating at the boundary hence the leakage current is low. Increasing the bias voltage (higher than 20 V) the dependence is linear up to a certain bias voltage where the detector gets close to full depletion. Near the V_d , a sudden step feature appears since both the contacts inject leakage current and it again becomes linear further increasing the bias voltage. For three different guard-ring detectors BLC with respect to bias voltage in the range of 30 - 70 V was considered.

The inhomogeneity of the a-Ge and crystalline Ge for three detectors is calculated considering the fabrication process. The A^* is treated as a constant (48 A/cm²K²). Y-intercept obtained from the $\ln J$ as a function of $(V_a)^{1/2}$ in Equation 5.7 gives the value of saturation current density (J_s) which is given by

$$J_s = A^*T^2 \exp(-\psi_{0,b}/kT). \quad (5.9)$$

$\psi_{0,b}$ can be re-written and calculated for a given temperature as

$$\psi_{0,b} = kT \ln(J_s/A^*T^2). \quad (5.10)$$

In addition to information on J_s , information about the N_f of an a-Ge can also be obtained from Equation 5.7 if the $|N_D - N_A|$ of the crystal is known. However, as shown in equation 5.9, N_f does not affect the J_s , hence also the $\psi_{0,b}$ calculation. No efforts were made to study the indirect contribution to the systematic errors to the $\psi_{0,b}$.

The variation of the BLC density as a function of the square root of applied bias voltage for USD-R03 detector is shown in Figure 5.4. I-V data for this detector was taken at the temperatures

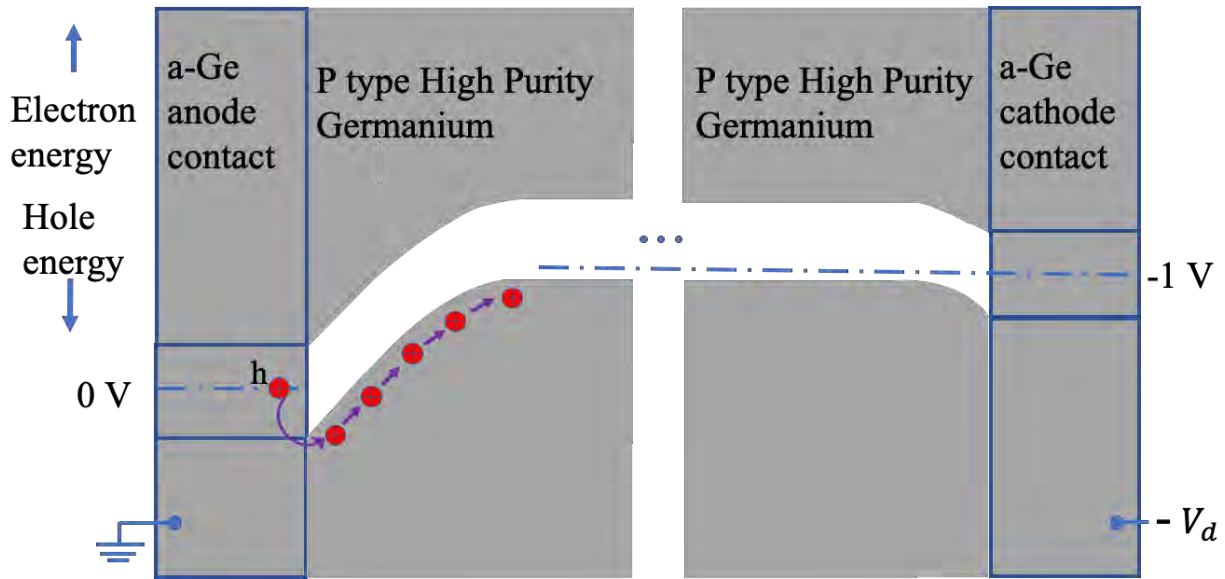


FIGURE 5.3: Shown is the schematic representation of energy band diagram for a p-type germanium detector. The Fermi level in the amorphous germanium lies in middle of the conduction and valence band. A small negative bias is applied to the bottom contact of the detector, hence the detector starts to deplete from its top surface [24]. (not to scale)

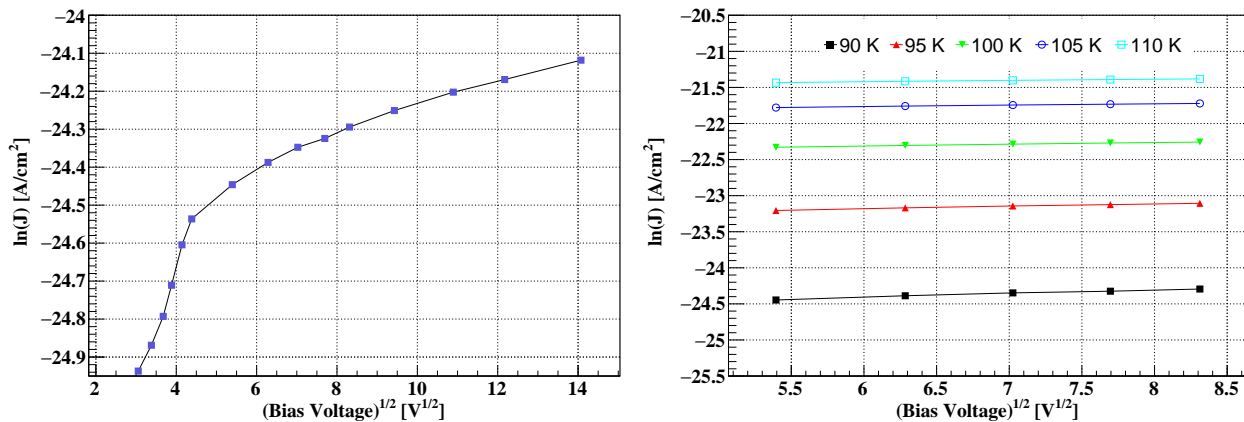


FIGURE 5.4: Left: the variation of the current density versus the square root of bias voltage for USD-R03 detector at 90 K. The plot shows that there are two distinguishable regions, which correspond to two different ranges of the applied bias voltage, 10- 20 volts and 30-70 volts; Right: shown is the variation of the leakage current density versus the square root of bias voltage for USD-R03 detector at different temperatures.

Table 5.1: Barrier height extrapolated from a linear fit of $\psi_{0,b}$ versus temperature.

Detector	[†] $\psi_{0,b}/eV$	* <i>slope</i>
<i>USD – R02</i>	$0.14983 \pm 8.4E - 4$	$0.00178 \pm 7.8E - 6$
<i>USD – R03</i>	$0.09285 \pm 5.8E - 4$	$0.00214 \pm 5.6E - 6$
<i>USD – W03</i>	$0.23962 \pm 1.1E - 3$	$0.00086 \pm 1.1E - 5$

[†] The zero-bias barrier height extrapolated to 0 K .

* The slope obtained from $\psi_{0,b}$ versus temperature plot.

90 K, 95 K, 100 K, 105 K and 110 K. Similar I-V characteristics were obtained for USD-R02 and USD-W03 detectors at the temperature 95 K to 115 K with the increment of 5 K. The zero-bias barrier height was calculated using the equation 5.10 which also takes into account the saturation current density obtained from the Y-intercept of the $\ln J$ vs $\sqrt{V_a}$. The relation between calculated barrier height and temperature is illustrated in Figure 5.4 for all detectors. As can be seen from the figure temperature and barrier height are interrelated to one another.

A linear fit was applied to the $\psi_{0,b}$ versus temperature plot as shown in Figure 5.4, the Y-intercept of the plot gives the $\psi_{0,b}$ at absolute temperature without considering the barrier lowering term. Since the data points are not perfectly linear there is some uncertainty in the prediction of barrier height in the low-temperature range. The slope obtained from the same linear fit gives the variation of the barrier height at a given temperature. Y-intercept ($\psi_{0,b}$) and slope (variation in barrier height) obtained from the linear fit are listed in Table 5.1.

The variation of the $\psi_{0,b}$ for each detector with temperature is attributed to the inhomogeneity of the interface. The energy band diagram for an a-Ge and p-type Ge interface is shown in Figure 5.3. The nature of the $\psi_{0,b}$ gives an impression that the barrier height saturates to a value ~ 0.32 eV for USD-R02 and USD-W03 detectors, and ~ 0.29 eV for USD-R03 detector. The predicted leakage current at 0 K is negligible, assuming the barrier height saturates (highest barrier height for 0 K). We have also predicted conservatively the leakage current using the linearly extrapolated data (lowest barrier height at 0 K). The assumption of the highest and lowest barrier height possible for a given temperature predicts the lowest and maximum BLC, respectively, for a detector at that temperature.

5.4.3 The Relation Between the Inhomogeneity of Interface and CBH

If a homogeneous interface layer is achieved for the contact formation, barrier height becomes constant with the temperature, hence, BLC density can be predicted at different temperatures and bias voltage with the help of equations 5.2 and 5.3 depending on the V_d of the detector. However, since the perfect homogeneity of the interface is difficult to achieve therefore barrier height cannot be treated as a constant value with respect to temperature.

The variation of CBH with respect to temperature is explained using the I-V-T characteristics. The fabrication process parameters used for the three detectors used in this study are the same except for the fluctuations from the instrument itself. There exist several uncertainties such as slight variation in the thickness of a-Ge layer due to the instability of process gas which jumps between 12 to 16 mTorr that also leads to slight variation in forward and reflected power, the exposure of the crystal outside the vacuum chamber when flipping the detector after depositing a-Ge on top and sides. In addition, the Ge crystal surfaces may not be identical since it involves multiple hands-on steps such as mechanical cutting and lapping, chemical etching, etc hence, it leads to the variation in the heterogeneous interface for three different detectors. The inhomogeneity at the interface for each detector might be related to the cleanliness of the surface of the Ge crystal before depositing a-Ge and the variation in thickness of a coated a-Ge layer. It is important to minimize the exposure of the etched crystal before loading into the chamber for a-Ge deposition as well as during the flipping of the crystal after completing one side (either top and sides or bottom) deposition of a-Ge to minimize the Ge oxide formation when exposed to the atmosphere.

The Gaussian distribution model was used to explain the correlation between the barrier height variation and the inhomogeneities of the heterogeneous interface. This model was developed by Werner and Guttler and can be expressed as [149];

$$\psi_{0,b} = \bar{\psi} - \sigma^2/2kT, \quad (5.11)$$

where $\bar{\psi}$ is the mean barrier height and σ is the standard deviation. σ is assumed to be a constant with respect to temperature for this calculation, therefore, barrier height varies with

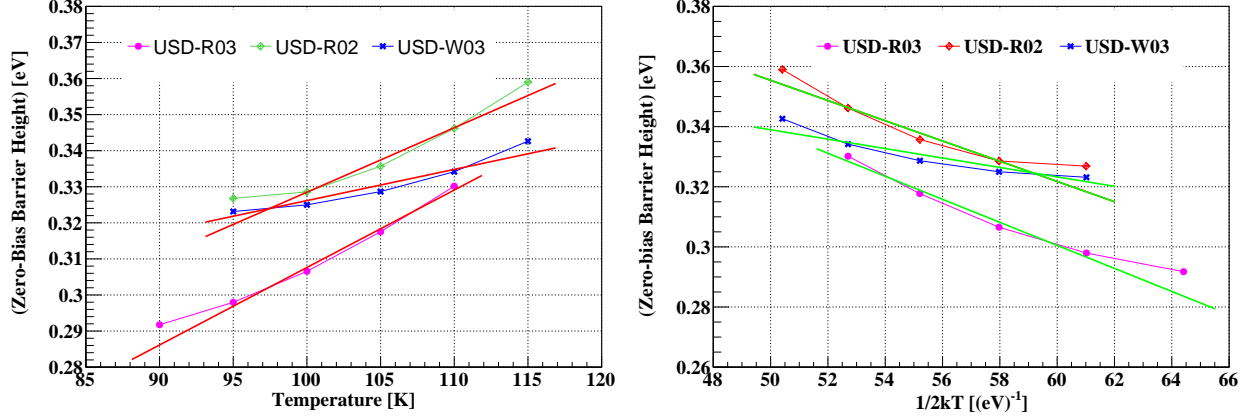


FIGURE 5.5: Left: shown is the variation of the $\psi_{0,b}$ versus temperature. The CBH at 0 K was extracted from the first-order polynomial fit; Right: shown is the variation of $\psi_{0,b}$ with respect to $1/2kT$.

the temperature. $\bar{\psi}$ and σ^2 were extracted from the plot in Figure 5.5 which corresponds to the Y-intercept and the slope respectively. Extracted $\bar{\psi}$ and σ^2 for three detectors are summarized in Table 5.2. The USD-W03 detector has a smaller value of σ than the other two detectors, indicating that the barrier height fluctuation is smaller for this detector than the other detectors. The implication of less fluctuation in the barrier height is in proportion to the variation of the BLC when the temperature of the detector is increased or decreased. The deviation of σ with respect to $\bar{\psi}$ is within the range 9% – 12% for three detectors characterized which gives a measure of barrier inhomogeneity. The thermionic emission model better explains the metal contacts formed on semiconductors, in which case the value of σ^2 is close to zero. Therefore, a smaller value of σ^2 indicates the interface formed is close to an ideal thermionic case and barrier homogeneity is established [150]. The measurement of σ^2 helps optimize the fabrication process parameters.

Assuming there is a little or no inhomogeneity (when σ^2 is close to 0), the band gap of a-Ge equals the sum of electron barrier height (ϕ_e) and hole barrier height (ϕ_h) [23]. The results published in these cited papers are based on the assumption that the barrier height is constant with respect to temperature. The procedure to calculate the barrier height for holes and electrons has already been discussed in the previous section. Constant barrier height and the trade-off relationship between the pre-factor and barrier height, the sum of $\phi_e + \phi_h$ equals the band-gap of a-Ge are simplified assumptions and may not explain the data accurately.

Table 5.2: Summary of three USD detector properties used for the study of inhomogeneity of the interface.

Detector	USD-R02	<i>USD – R03</i>	<i>USD – W03</i>
▷ Impurity/cm ³	2.93×10^{10}	3.78×10^{10}	2.60×10^{10}
Thickness/cm	0.65	0.81	0.94
‡ Area/cm ²	0.29	0.48	0.24
* V_{fd}/V	700	1400	1300
⊢ $\psi_{0,b}/eV@90K$	–	$0.29174 \pm 1.8E - 4$	–
⊢ $\psi_{0,b}/eV@95K$	$0.32679 \pm 1.8E - 4$	$0.29795 \pm 9.7E - 5$	$0.32313 \pm 1.3E - 4$
⊢ $\psi_{0,b}/eV@100K$	$0.32858 \pm 9.3E - 5$	$0.30655 \pm 5.4E - 5$	$0.32498 \pm 1.5E - 4$
⊢ $\psi_{0,b}/eV@105K$	$0.33570 \pm 6.4E - 5$	$0.31752 \pm 5.4E - 5$	$0.32866 \pm 1.6E - 4$
⊢ $\psi_{0,b}/eV@110K$	$0.34619 \pm 6.7E - 5$	$0.33015 \pm 5.3E - 5$	$0.33418 \pm 1.8E - 4$
⊢ $\psi_{0,b}/eV@115K$	$0.35898 \pm 1.2E - 4$	–	$0.34262 \pm 2.4E - 4$
* $\bar{\psi}/eV$	$0.52367 \pm 8.2E - 4$	$0.52359 \pm 8.3E - 4$	$0.41734 \pm 1.1E - 3$
± $\sigma^2/(eV)^2$	$0.00336 \pm 1.5E - 5$	$0.00371 \pm 1.4E - 5$	$0.00156 \pm 2.7E - 5$

▷ Net impurity concentration calculated from the C-V measurements.

‡ Area of the central contact on the top surface.

* Full depletion voltage for the detector.

⊢ Zero-bias barrier height.

* Mean-barrier height.

± Variance of barrier height fluctuation.

5.5 Conclusions

Barrier height was calculated for the USD-R03 detector without considering the inhomogeneity. However, assuming the dependence of BLC only on the temperature of operation alone doesn't reproduce the leakage current data for a wide temperature range. Another method was also applied to calculate the barrier height for the three detectors used for this study, this model treats the J_0 same as the A^* but does not take into consideration the inhomogeneity [136]. Without the J_0 or the inhomogeneity consideration, the model was unable to accommodate the fabrication process parameter. Most of the previous studies were based on the assumption that the J_0 depends on process parameters and is an unconstrained parameter.

Variation of CBH with respect to temperature was studied for the first time for an a-Ge deposited Ge detector. To investigate the inhomogeneity of the interface layer, we have treated the pre-factor (J_0) the same as the (A^*). The inhomogeneity level of the interface is attributed to

the process parameters used in fabricating the detectors. The nature of barrier height formed also depends on the surface properties of the crystalline Ge. The Gaussian distribution model developed by Werner and Guttler was used to study the variation of the CBH at a wide temperature range. The fluctuation of barrier height with respect to temperature is attributed to the inhomogeneity created when the a-Ge contacts are formed on the crystalline surface of HPGe. The observed variation of inhomogeneity between three USD-made detectors hints that the fabrication process can be optimized to minimize the variation in the barrier height.

A linear fit to the data was used to estimate the barrier height and the BLC at a lower temperature. Since the analysis done in this study is only for a limited temperature range (90 K to 115 K), there exists a large uncertainty in the prediction for the lower temperature. However, it is safe to say that the BLC will be less than $\sim 10^{-24}$ A at LHe temperature since the CBH of 0.02 eV is sufficient to block the charge injection through the contacts. As seen from Table 5.1, the CBH either saturates at a large value or if it follows the linear trend also it will be significantly larger than 0.02 eV. To cross-check the prediction for the lower temperature, BLC measurements were carried out at the temperatures of 5 K and 80 K. The injected leakage currents were observed < 0.4 pA for both the temperatures. The accuracy of the Keithley picoammeter currently in use at USD is 0.4 pA. To verify the prediction more accurately better sensitive device to measure the leakage current is needed or other techniques need to be explored.

Charge Trapping in Germanium Detectors

Charge carrier transport has been studied very well around liquid nitrogen (LN_2) and millikelvin (mK) temperature. However, the physics of charge carriers is little understood around liquid helium (LHe) temperature. It is important to understand the physics of the Ge detector at a wide temperature range. This is particularly important for large-size Ge detectors in rare event searches, in which case, a low energy threshold is desirable. In this chapter, the physics of charge trapping in the Ge detector at LN_2 and LHe temperature is discussed.

6.1 Charge Carrier Transport in Ge Detector

6.1.1 Electric Field Calculation in a Planar Detector

All the detectors characterized in this study are of planar geometry. It is important to know the magnitude of the electric field within the detector to evaluate the detection efficiency of the detector. Trapping length, charge collection efficiency, scattering cross-section, and drift velocity are some of the parameters in the charge transport mechanism which depends on the electric field in the detector. For the simplification of electric field calculation, the net impurity concentration ($|N_A - N_D|$) in the crystal is assumed to be constant and uniformly distributed within the detector. The magnitude of the electric field at the top and bottom contacts of the detector, and as a function of distance for an n-type detector biased positively from the bottom contact of the detector are

given as [151];

$$E_t = \sqrt{\frac{2qV_a N_{|N_A - N_D|}}{\epsilon}}, V_a < V_d \quad (6.1)$$

$$E_t = \frac{V_a + V_d}{D}, V_a > V_d \quad (6.2)$$

, respectively. The magnitude at the bottom contact of the detector is given as;

$$E_b = 0, V_a < V_d \quad (6.3)$$

$$E_b = \frac{V_a - V_d}{D}, V_a > V_d \quad (6.4)$$

Since the impurities are in an ionized state after the free charge carriers are swept away to the electrodes in a fully depleted detector, the impurity ion screens the electric field distribution. As a result, the magnitude of the electric field decreases linearly as a function of distance from the contact. For a fully depleted detector, the magnitude of the electric field as a function of distance, x , can be written as;

$$E(x) = \frac{V_a + V_d}{D} - \frac{2V_d x}{D^2}, V_a > V_d \quad (6.5)$$

Where E_t , E_b , V_a , V_d , $|N_A - N_D|$, and D represents the electric field at the top contact, electric field at the bottom contact, applied bias voltage, full depletion voltage of the detector, net impurity concentration of the crystal and detector thickness, respectively. The USD-R09-02 and USD-RL detector fully depletes at ~ 1200 V and ~ 400 V, respectively, determined from the C-V characteristics. As shown in Figure 6.1, in order to achieve a high enough electric field throughout the detector volume, the detector needs to be over-biased with a voltage above a few hundred volts than the V_d . The impurity atoms turns into space-charge after the detector is depleted and affects the electric field distribution within the detector, hence, it is desired to have a low impurity concentration crystal, otherwise, the electric field on one of the contacts will be much higher. The

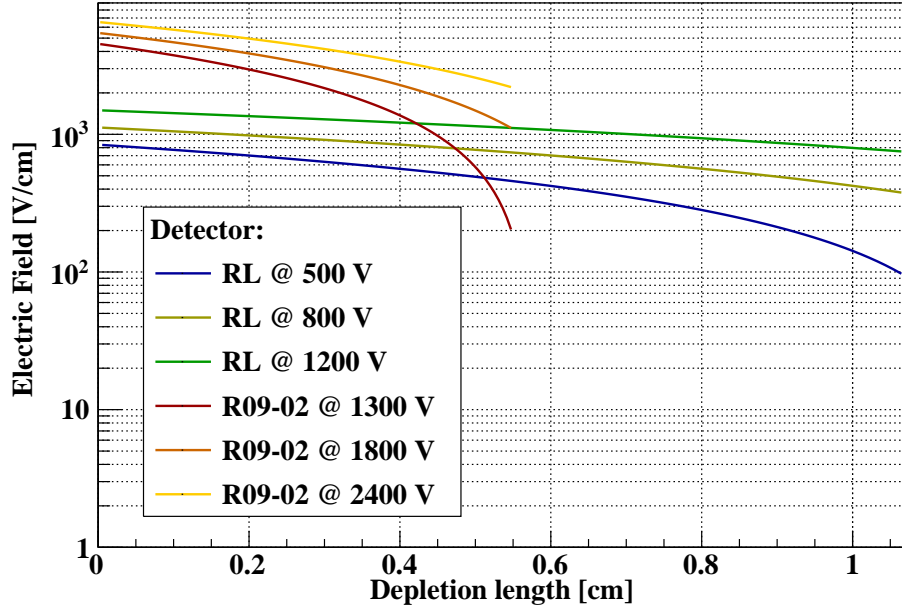


FIGURE 6.1: Shown is the electric field distribution in two detectors, USD-RL and USD-R09-02. The V_d for these detectors is 400 V and 1200 V, respectively.

contacts should be robust enough to hold such a high field. A detailed study of space charge contribution in various detector geometries can be found in this published paper [152].

6.1.2 Schokley-Ramo Theorem

When incoming radiation interacts with the target (Ge-detector), it generates free-moving charge carriers (electrons or/and holes). Since for our setup, bias is only applied from the bottom electrode of the detector, the bottom electrode can be positive or negative (depending on the polarity of bias voltage) whereas the top electrode is always grounded. Electrons are accelerated to the positive (grounded) electrode and holes to the grounded (negative) electrode. The induced charge generated from the moving charge q is Q , which gives a measure of the amount of energy deposited within the detector. The output signal is time-dependent which can be predicted considering the charge Q as a position-dependent parameter. The model for the amount of Q induced on the electrode was developed by Shockley and Ramo [153, 154], and described by the equation;

$$Q = -q\psi_0(\vec{x}) \quad (6.6)$$

and induced current is given as;

$$i = q\vec{v} \cdot \vec{E}_0(\vec{x}) \quad (6.7)$$

where \vec{v} is the instantaneous velocity which is determined from the actual electric field applied to the contacts and also considering the electric field generated by space charges, $\psi_0(x)$ is the electric potential and $E_0(x)$ is the electric field at point x . Equation 6.7 can also be written in terms of weighting electric field (E_w) as

$$i = qE_w v \quad (6.8)$$

The magnitude of the instantaneous velocity is equal to $\frac{dx}{dt}$. For an n-type planar detector geometry, biased positively from the bottom electrode of the detector, electrons drift towards the positive electrode transversing the distance L (for a fully depleted detector and localized charge carriers created on the top surface of the detector). Weighting potential at the bottom electrode in such a condition is given by;

$$E_w = -\Delta\psi_0(x) = \frac{1}{L} \quad (6.9)$$

Using Equation 6.9 and the relation $dQ = idt$, Equation 6.8 can also be written as;

$$dQ = q \frac{dx}{L} \quad (6.10)$$

6.1.3 Charge Collection Efficiency

Ge detectors are usually operated in reverse bias mode to enhance the depletion region. When the incident radiation interacts with Ge atoms, it creates a cloud of charge carriers. The charge carriers can encounter impurities while drifting through the detector. Charge trapping occurs as the charge carrier drifting through a detector gets bound to a spatially localized impurity state. Charge carriers can be temporarily or permanently trapped to the impurity state and hence there is a delayed signal or no signal at all. Trapping of charge carriers causing the prolonged pulse can be recovered partially or fully. Charge trapping can distort signals and also directly affect the energy resolution of the detector.

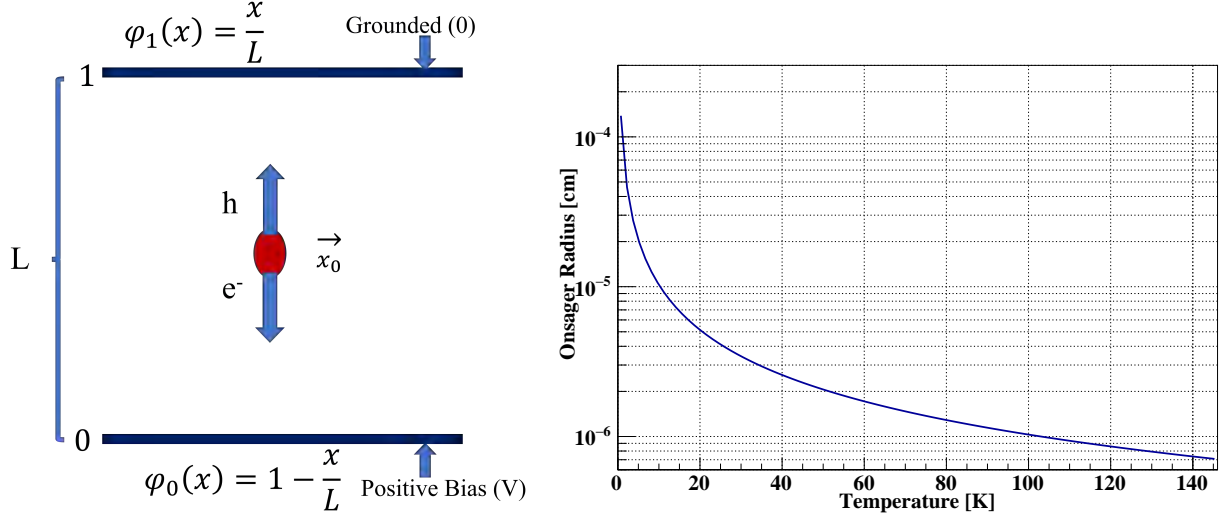


FIGURE 6.2: Left: shown is a schematic diagram of the charge drifting process in a planar detector. A positive bias voltage is applied from the bottom electrode of the detector and top contact is grounded. Interaction shown here represents the interaction point that occurs somewhere middle of the detector and charge carriers are drifted towards the oppositely biased electrode; Right: shown is the plot of Onsager radius as a function of temperature.

In order to understand the charge trapping phenomenon better, both shallow and deep traps have to be investigated. Shallow and deep trapping levels are defined relative to the energy of the trap. In an intrinsic Ge detector, there exists a forbidden band between the conduction band and the valence band. Defects such as impurities, vacancies, interstitials, etc exist in the Ge detector which creates the allowed energy states somewhere between the conduction and valence band depending on the type of impurities.

Neutral impurities are present in the Ge crystal. The charge trapping phenomena described here is for the case of a fully depleted detector, hence, neutral impurities are in the form of ions. Trapping length is the characteristic property of the detector defined as the mean length the charge carriers travel through a detector before being trapped. Therefore, the number of charge carriers will decrease exponentially with the distance the particles travel. The statistics of holes, after traversing a distance (x) is given as [155];

$$N_h(x) = N_h(0)e^{(-\frac{x}{\lambda_h})} \quad (6.11)$$

where $N_h(0)$ is the population of holes generated near the top electrode ($x \sim 0$) and λ_h is the

trapping length for holes.

In a fully depleted detector of thickness, L , the number of induced charges at the position x can be found by integrating Equation 6.10 from $x = 0$ to $x = L$, which is given as;

$$Q_{h,L} = Q_{h,0} \frac{\lambda_h}{L} (1 - e^{-\frac{L}{\lambda_h}}) \quad (6.12)$$

Where $Q_{h,0} = qN_{h,0}$ is the total charge at $x = 0$ and $Q_{h,L}$ is the total charge at $x = L$.

Equation 6.12 is the generalized form when only one type of charge carriers transverses the detector which is mostly applicable to the localized charges created by α s and low-energy β s. Since the γ s create a cluster of charges within the detector, both types of charge carriers traverse through the detector.

$$Q = Q_0 \frac{\lambda_h}{L} (1 - e^{-\frac{z}{\lambda_h}}) + \frac{\lambda_e}{L} (1 - e^{-\frac{(L-z)}{\lambda_e}}) \quad (6.13)$$

where λ_e and z are the electron trapping length and the hole drift distance respectively. The sum of hole drift distance and electron drift distance is equal to the total thickness of the detector.

6.2 Charge Trapping and Capture in a Ge Detector at LHe Temperature

6.2.1 Impurities Freeze-out Phenomena

Different techniques can be used to find $|N_A - N_D|$ in a Ge crystal, some common techniques are discussed in Chapters 3 and 4. At around 80 K, free charge carriers (holes or electrons) are available in the crystal. When a small bias voltage is applied, free charge carriers are swept away from the depleted region, hence the neutral impurity atoms turn into ions (space charges). If the applied bias voltage is equal to or greater than the full depletion voltage of the detector, all the free charges in the detector are swept away to the electrodes. Further lowering the detector temperature without the application of bias voltage, these free charge carriers start to freeze-out. Even when the bias voltage is applied, those charge carriers are not swept away at low temperatures (< 11 K). Note that if the temperature of the detector is lowered from ~ 80 K for a fully depleted detector without turning down the bias voltage to zero, the process could be different. USD group is currently taking

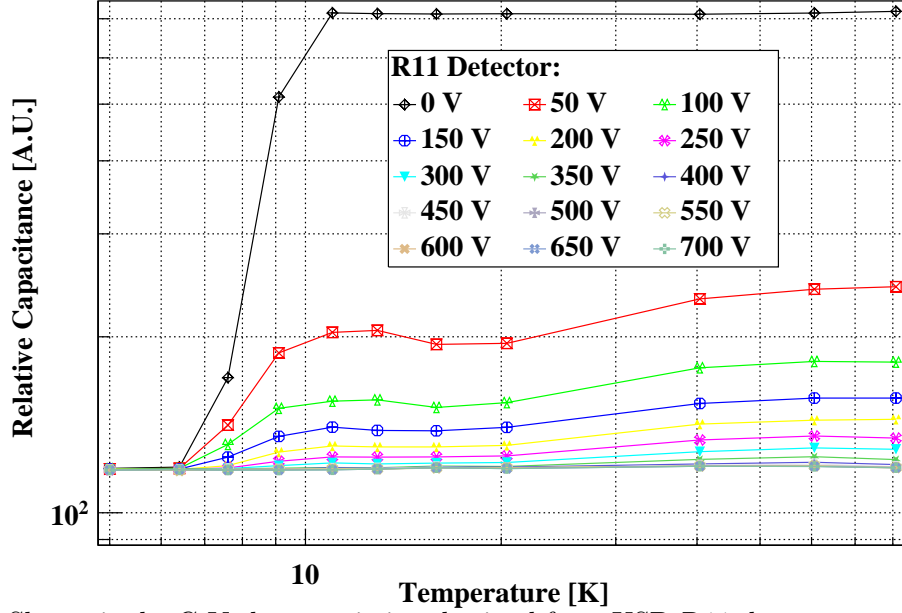


FIGURE 6.3: Shown is the C-V characteristics obtained for a USD-R11 detector at various temperatures. The V_d of this detector is 500 V. It has a $|N_A - N_D|$ of $5.81 \times 10^{10} / \text{cm}^3$ and a thickness of 3.9 mm.

data to understand if there is any physics difference involved in these two modes of operation. All the physics phenomena described here are based on the former mode of operation. The free-charge carriers start to freeze-out at a temperature below about 11 K and are completely frozen at a temperature below 6.4 K as shown in Figure 6.3. There might be a slight deviation in these values for a Ge crystal depending on the impurities present in the crystal since the freezing temperature is related to the binding energies of the impurities. The freezing of free charge carrier means they are bound to their respective impurity atoms. The freeze-out of charge carriers creates excited electric dipoles or neutral states ie. D^{0*} and A^{0*} , hence the number of free charge carriers start to decrease at around 11 K. C-V characterization method is discussed in detail in Chapter 4. The capacitance as a function of temperature at various bias voltages (C-T-V) in the temperature range of 80 - 5 K is shown in Figure 6.3. As seen in Figure 6.3, the relative capacitance of the detector without any bias voltage applied at less than 6.4 K is the same as that of at 80 K with the 500 V applied. 500 V is the V_d of the detector, USD-R11, used for this study. Therefore, it confirms that there exist no free charges at less than 6.4 K.

The extra (free) electrons or holes of impurity atoms that are not bounded to the Ge atoms can move freely if the thermal energy exceeds the Coulomb energy. The model developed by Onsager in 1938 relates the Onsager radius (R) as a function of temperature as;

$$R = \frac{e^2}{4\pi\epsilon kT} \quad (6.14)$$

where e is the electronic charge, ϵ is the permittivity of Ge, k is the Boltzmann constant, and T is the temperature.

The thermal separation of a hole or electron at less than 11 K elongates the outer orbital largely, from the core of the atom hence it is no more circular. For example, for an n-type impurity atom, the fifth electron of the outermost shell is separated from the core of the atom. This separation of a core of the atom (positively charged) and the fifth electron (negatively charged) creates the thermally excited electric dipole states D^{0*} , since the atomic structure is deformed. Similarly, it can be described for a p-type impurity in this case excited electric dipole states A^{0*} are formed.

6.2.2 Cluster-dipole Formation

The freezing of charge carriers at around LHe temperature forms excited dipole states A^{0*} and D^{0*} in p-type and n-type impurities, respectively. When incoming radiation interacts with the detector, it deposits energy in the detector resulting in electron-hole pairs. There exists a Coulomb attraction between the charge carriers and charges or ions of excited neutral dipole states. The trapping of charge carriers by these excited neutral states forms the cluster dipole states. The schematic diagram of dipole and cluster dipole formation in a p-type and n-type impurity atom is shown in Figure 6.4. Energy is released by the phonon excitation if the excited cluster dipole is formed by the shallow trap whereas for the deep trap single space-charged state is formed.

The positively charged donor ion and negatively charged acceptor ion for p-type and n-type impurities, respectively are deeply confined by the deformation potential. Therefore the allowable phase space for charge trapping is less than that of bounded frozen charge carriers. The electrons or holes can move within the limit defined by the Onsager radius. Therefore the likelihood of the formation of D^{-*} and A^{+*} is more through the trapping of holes with the electrons, and electrons

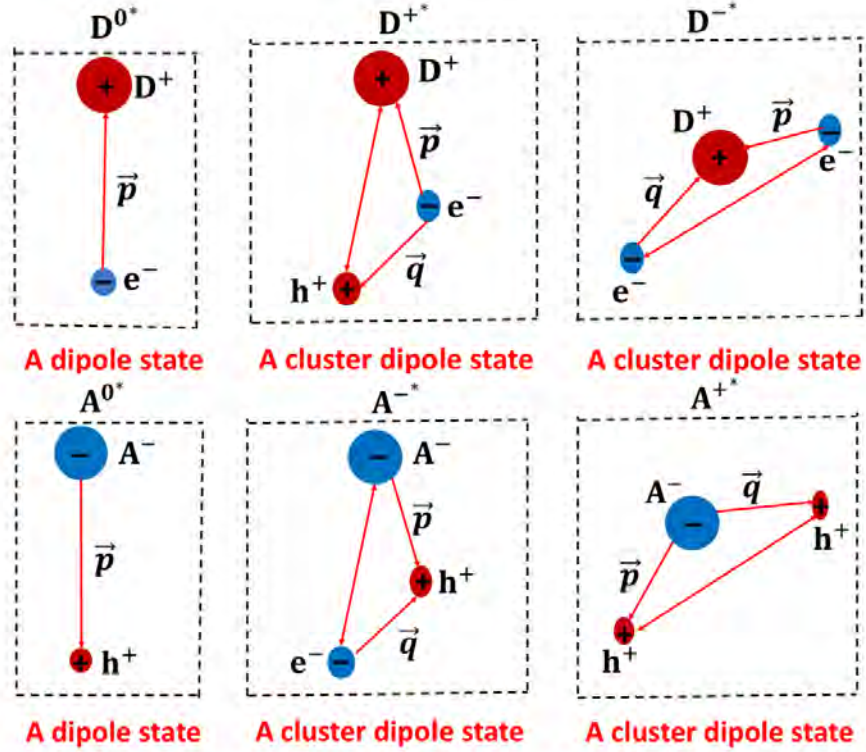


FIGURE 6.4: The schematic representation of the excited states of the dipole and cluster dipole formation in a p-type and n-type impurity atom in a Ge crystal. This process comes into play at temperatures below ~ 11 K. \vec{p} and \vec{q} represent the corresponding dipole moments [156].

with the holes respectively. The probability of trapping electrons and holes by the D^+ and A^- states respectively is less. Hence, electrons and holes are trapped more severely in a p-type and n-type detector respectively than the holes in a p-type and electrons in a n-type detector.

The cluster dipole formation process is summarized as follows;

- $D^{0*} + h^+ \rightarrow D^{+*}$
- $D^{0*} + e^- \rightarrow D^{-*}$
- $A^{0*} + e^- \rightarrow A^{-*}$
- $A^{0*} + h^+ \rightarrow A^{+*}$

6.2.3 Spectral Analysis

The energy deposited from a 5.3 MeV α s generated from ^{241}Am source was recorded at 5.2 K and 77.8 K for both polarity of bias voltage for a USD-R09-02 (n-type) and USD-RL (p-type) Ge planar detector. Note that the bias voltage was only applied from the bottom electrode and the signal was read out from the top electrode. The well-known characteristics of α s in a Ge detector at 77.8 K were used for the comparison at 5.2 K. The ^{241}Am source was placed inside the PTR ~ 0.5 cm above the top surface of the detector. The schematic diagram of the charge carrier's movement shown in Figure 6.2 represents well for the γ s since the γ s create a cluster of charges everywhere in the detector. In the case of α s, the energy deposited is localized within < 100 μm in a crystalline Ge detector. The following mode of operation was followed to study the charge trapping of holes and electrons separately.

- ^{241}Am source was placed on the collimated-PTFE bar just above the top surface of the detector, hence the 5.3 MeV α s deposit energy on the top surface of the detector (< 100 μm thickness in Ge detector).
- the p-type detector was biased negatively from the bottom contact, hence the holes drift throughout the detector thickness and reach the bottom electrode. (Mode#1, hole trapping study in a p-type detector)
- the p-type detector was biased positively from the bottom contact, hence the electrons drift throughout the detector thickness and reach the bottom electrode. (Mode#2, electron trapping study in a p-type detector)
- an n-type detector was biased negatively from the bottom contact, hence the holes drift throughout the detector thickness and reach the bottom electrode. (Mode#3, hole trapping study in an n-type detector)
- an n-type detector was biased positively from the bottom contact, hence the electrons drift throughout the detector thickness and reach the bottom electrode. (Mode#4 electron trapping study in an n-type detector)

For the above-mentioned modes of operation, when α deposits energy in the detector, only one type of charge carrier travels through the detector when a bias voltage is applied. Hence, using the α source and changing the polarity of bias voltage, the charge trapping phenomenon can be studied for each type of charge carrier separately for both p and n-type detectors. The direction of charge carriers' movement does not depend on the n-type and p-type detector, it is only determined by the polarity of bias voltage. ^{137}Cs spectrum was also taken in a similar mode of operation as described above. ^{137}Cs source was placed outside the PTR, closed to the detector surface from the side. Unlike α s whose energy deposition is localized, charge carriers from 662 keV γ can scatter and deposit energy in wider regions of the detector. Spectra obtained from ^{137}Cs was used to validate our prediction of charge trapping which was made based on the results obtained from the α spectrum. Energy deposited by the α was recorded for each temperature (5.2 K, 5.7 K, 6.4 K, 6.8 K, 7.6 K, 9.06 K, 11.02 K, and 77.8 K) as a function of bias voltage in the 4 modes of operation. Energy deposited by the 661.7 keV γ was only recorded for the positive and negative polarity of bias voltage at 5.2 K and 77.8 K since taking the ^{137}Cs spectrum took a lot longer time. ^{137}Cs source was placed outside the cryostat whereas the ^{241}Am source was placed inside the cryostat.

Alpha spectra

Left two plots of Figure 6.5 and the right two plots of the same Figure 6.5 are the energy deposited by α s at temperatures 5.2 K and 77.8 K. The upper two plots are obtained for operation mode #3 and the bottom two plots are obtained for operation mode #4. The behaviors observed in the right two plots of Figure 6.5 are fairly well understood. In mode #3, the detector starts to deplete from the bottom surface of the detector. The ^{241}Am source is facing the top surface of the detector, hence the α s deposit energy in the undepleted region of the detector. Without the electric field in the undepleted region, charge carriers recombine and do not contribute to the charge signal. Positive charge carriers drift towards the bottom electrode. When mode #4 is in operation, the detector starts to deplete from the top surface, hence even with a small thickness of the depleted region charge carriers can induce the signal, however, the detection efficiency is low since charge

Table 6.1: Shown are the properties of three detectors used for the study of charge trapping and C-V characteristics.

Detector	Dimensions (l×b×h)	Impurity (/cm ³)	*V _d (V)	Type	a-Ge (nm)
USD-RL	1.88×1.79×1.07	6.2×10 ⁹	400	p-type	1200
USD-R09-02	1.17×1.15×0.55	7.02×10 ¹⁰	1200	n-type	600
USD-R11	1.18×1.16×0.39	5.81×10 ¹⁰	500	n-type	360

* V_d Full depletion voltage for the detector.

carriers encounter neutral impurities of the undepleted region. As shown in the C-V characteristics curve in Figure 6.3, the detector is already free of free charge carriers, therefore the α spectrum is expected to obtain with a few ten's of bias voltage for both the polarity of bias voltage. However, as shown in Figure 6.5, the energy deposited by the α s is less than that of 77.8 K. In addition, mode #3 of the operation results in a severe decrease in detection efficiency compared to mode #4. As shown in Figure 6.5 to see a clear signal from mode #3, the detector needs to be biased \sim 1200 V. Even with the small bias voltage applied, mode #4 operation resulted in a clear signal of α s, however, the charge collection efficiency is much smaller than expected and also less than the same mode of operation at 77.8 K. This arises the question of charge trapping phenomena at low temperatures. The charge trapping model at low temperature is described in the section Cluster Dipole Formation.

Similarly, a p-type detector was used to study the charge trapping phenomena at around LHe temperature. The energy deposited by a 5.3 MeV α particle is shown in Figure 6.6 for the p-type detector operated at 5.2 K and 77.8 K. Similar behavior of the detector was observed at 77.8 K and 5.2 K to that of the n-type detector. Primarily, there were two differences observed between these two n and p-type detectors. First, the difference is with the polarity of bias voltage. As shown in Figure 6.5, when positive bias was applied to an n-type detector signal can be seen more clearly, however, for the p-type detector negative bias resulted in a clear signal than when the detector was positively biased. Another difference is the applied bias voltage required to achieve the same CCE. The former is explained in the model of cluster dipole formation; Later, is due to the difference in a-Ge thickness and the impurity concentration between two detectors which is

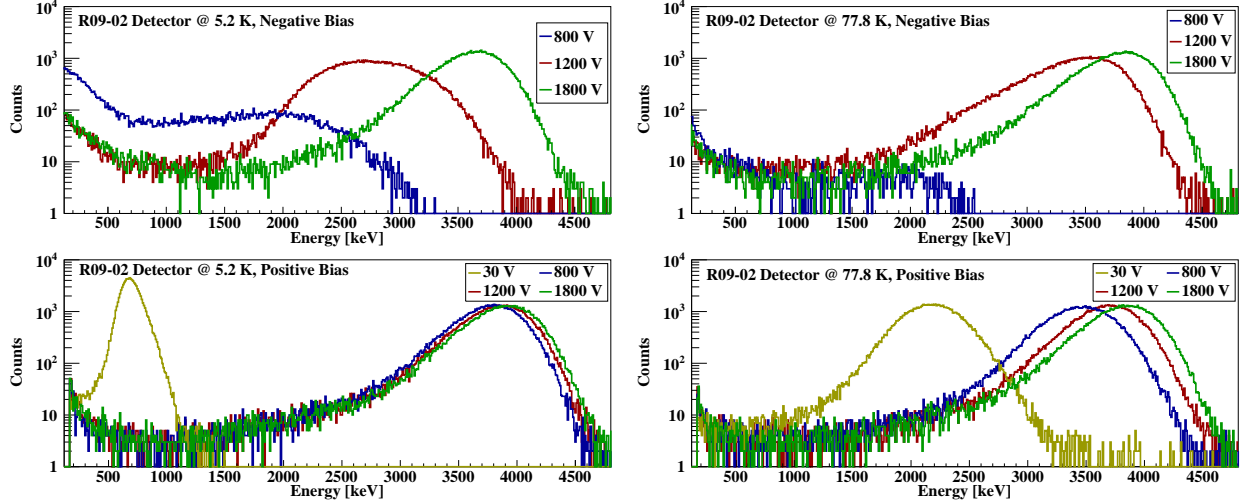


FIGURE 6.5: Shown is the energy deposited from the 5.3 MeV α s in an n-type detector, R09-02. The plots shown on the left and right are for the detector operated at 5.2 K and 77.8 K respectively. The top plot on both sides was taken when negative bias was applied at the bottom surface whereas the bottom plots on both sides were taken when positive bias was applied at the bottom surface.

shown in Table 6.1. The variation of energy deposition in a Ge detector by the 5.3 MeV α s as a function of a-Ge thickness was studied using several detectors having a-Ge thickness of the range of ~ 300 nm - 1200 nm and such behavior is well understood.

The normalized CCE as a function of bias voltage (both polarity) for both the detectors with α source is summarized and shown in Figure 6.7. The plots in Figure 6.7 shows CCE at 5.2 K and 77.8 K.

Gamma Spectra

To validate our theory of cluster dipole formation, 661.7 keV γ spectra was taken from ^{137}Cs source for both the detectors, USD-R09-02 and USD-RL. The spectra were obtained by exposing the γ source to the n and p-type detector, the spectra are shown in Figures 6.8 and 6.9, respectively. As seen in the figure, there is no dependency on the polarity of bias voltage. This is because the gamma energy deposits, unlike α deposits, are not localized. However, the CCE at 5.2 K has significantly reduced for both the detectors compared to that of 77.8 K for the lower bias voltage.

The normalized CCE as a function of bias voltage (both polarity) for both the detectors using a γ source is summarized and shown in Figure 6.10. In addition, these plots in the Figure 6.10 has

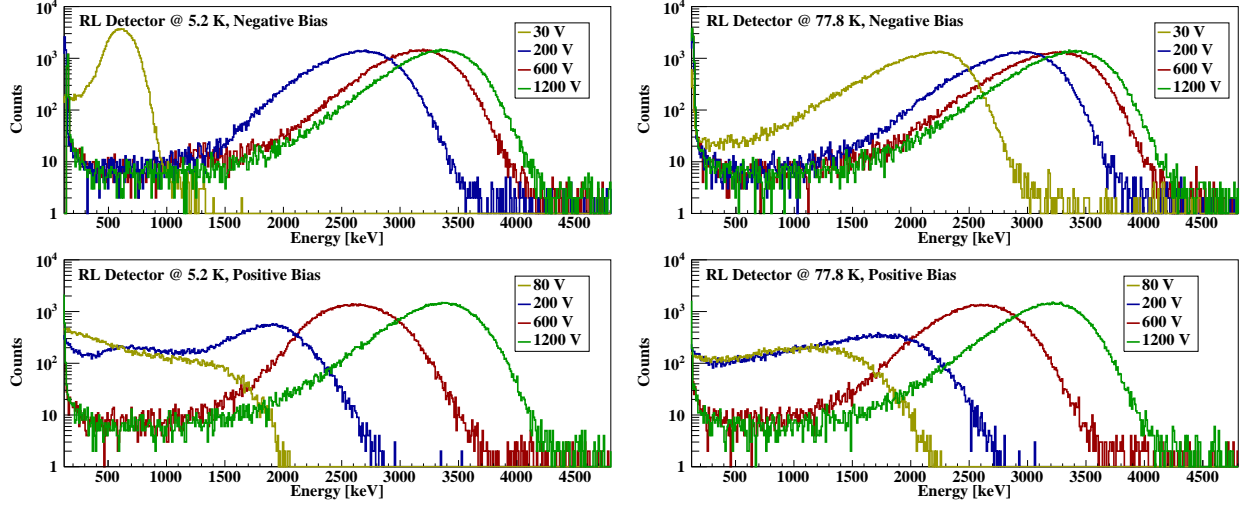


FIGURE 6.6: Shown is the energy deposited from the 5.3 MeV α s in a p-type detector, RL. The plots shown on the left and right are for the detector operated at 5.2 K and 77.8 K, respectively. The top plot on both sides was taken when negative bias was applied at the bottom surface whereas the bottom plots on both sides were taken when positive bias was applied at the bottom surface.

normalized CCE information at 5.2 K and 77.8 K.

6.2.4 Trapping Length of the Charge Carriers

The CCE of a detector is the fraction of energy deposited that is detected. The current setup at USD is not sufficient to find out the absolute CCE of a detector. Hence, the charge trapping is studied with the relative CCE data. CCE data was normalized with respect to the energy of 77.8 K at a

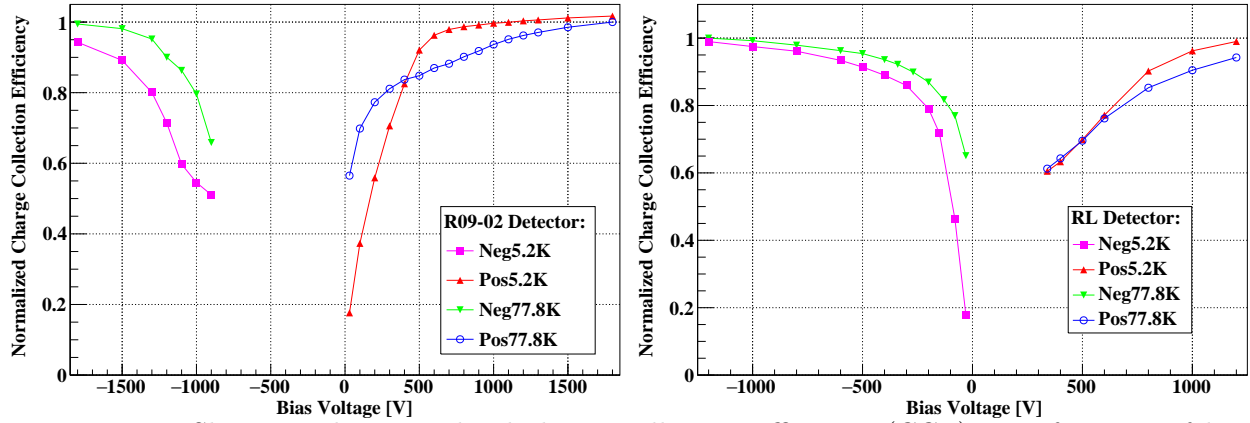


FIGURE 6.7: Shown is the normalized charge collection efficiency (CCE) as a function of bias voltage at temperatures 5.2 K and 77.8 K using an alpha source. Left: normalized CCE for a n-type detector; Right: normalized CCE for a p-type detector.

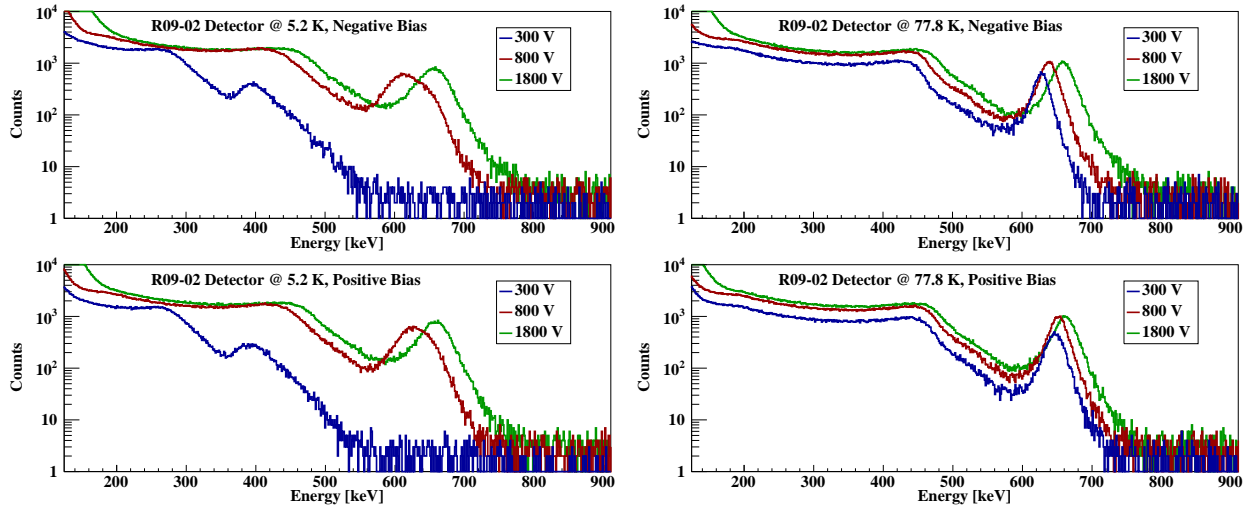


FIGURE 6.8: Shown is the energy deposited from the 661.7 keV γ -rays in a n-type detector, R09-02. Plots shown on the left and right are for the detector operated at 5.2 K and 77.8 K respectively. The top plot on both sides were taken when negative bias was applied at the bottom surface whereas the bottom plots on both sides were taken when positive bias was applied at the bottom surface.

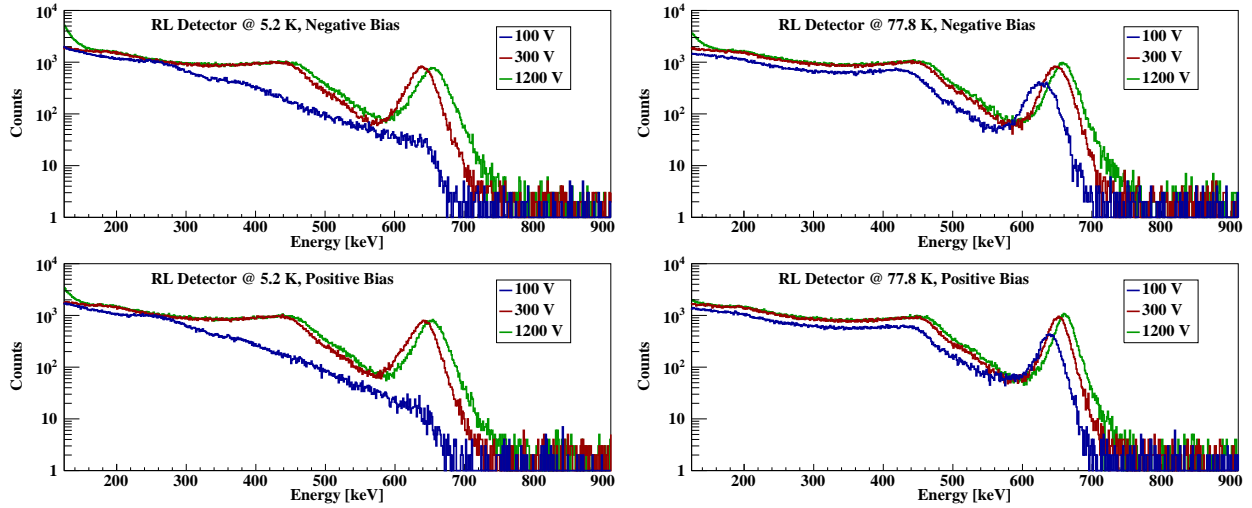


FIGURE 6.9: Shown is the energy deposited from the 661.7 keV γ -rays in a p-type detector, RL. The plots shown on the left and right are for the detector operated at 5.2 K and 77.8 K respectively. The top plots on both sides was taken when negative bias was applied at the bottom surface whereas the bottom plots on both sides was taken when positive bias was applied at the bottom surface.

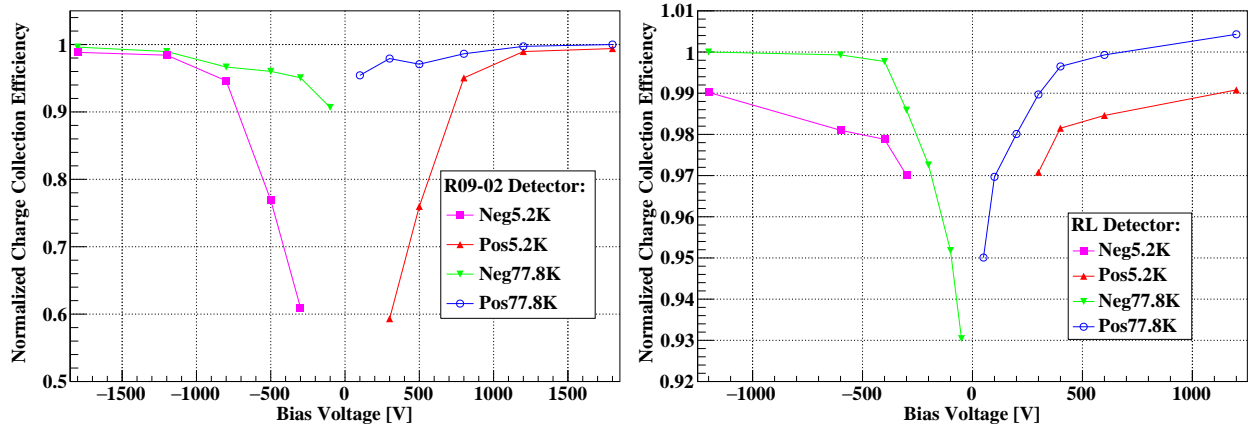


FIGURE 6.10: Shown is the normalized charge collection efficiency (CCE) as a function of bias voltage using a gamma source at temperatures 5.2 K and 77.8 K. Left: normalized CCE for a n-type detector; Right: normalized CCE for a p-type detector.

higher bias voltage data, where the CCE saturates with the bias voltage. The CCE improves with increasing the bias voltage as the charge carriers acquire high drift velocity at higher bias voltages. The trapping length depends on the trapping cross-section and the impurity concentration of the Ge detector. For a given detector, a shorter trapping length implies the charge carrier trapping is significant while the larger trapping length indicates smaller charge trapping in comparison.

To calculate the trapping length for holes and electrons for USD-R09-02 (n-type) detector, first, the relative CCE was determined at 1200 V with respect to that of 1800 V at both polarity of bias voltage. The relative CCE extracted from the observed data is 75.74 % for holes and 98.68 % for electrons. The Equation 6.12 gives the trapping length for the holes and electrons 0.94 cm and 20.8 cm, respectively. Similarly, the trapping length calculated for USD-RL (p-type) detector at 600 V were 9.25 cm and 2.05 cm, for the holes and electrons, respectively. Identifying the interaction position of the 661.7 keV γ within the detector is not straightforward since gamma energy depositions are not localized but spread out. Hence, no effort was made to find out the trapping length using the energy deposition data from γ . However, the interaction position was obtained using the information of trapping length from the *alpha* data. The CCE depends on the interaction position where electron-hole pairs are created which is shown in Figure 6.11. Since n-type (p-type) detectors trap electron (hole) more, the CCE depends on the distance each type of

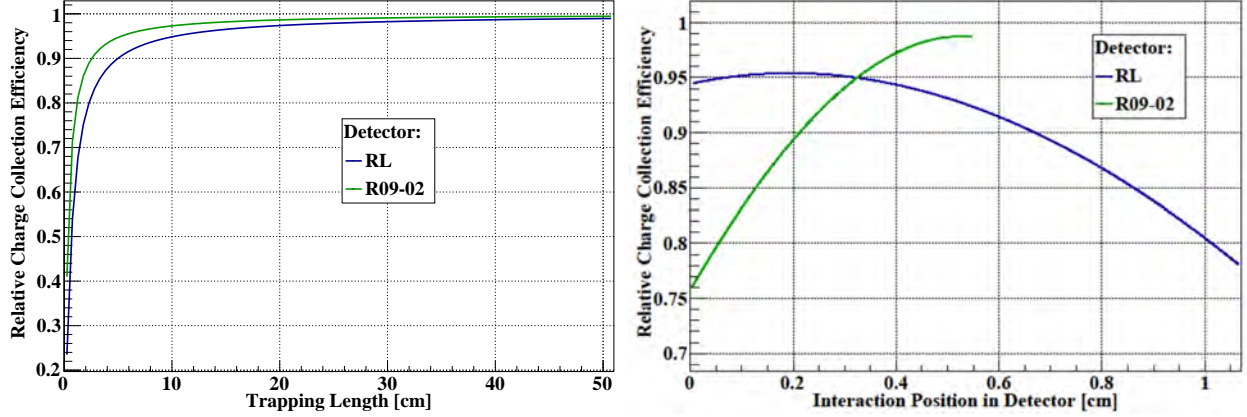


FIGURE 6.11: Left: shown is the relation between charge collection efficiency and trapping length of charge carriers for two detectors. The detector thickness of R09-02 and RL detector is 1.07 cm and 0.55 cm respectively; Right: shown is the plot of charge collection efficiency as a function of interaction position of γ . The trapping length for this plot was obtained from the alpha data.

charge carrier traverse in the detector. However, γ interactions create spatially separated charge clusters, so it is difficult to distinguish CCE between two different polarities of bias voltage.

The relation between CCE and trapping length of the charge carriers for R09-02 (n-type) and RL (p-type) detector is illustrated in Figure 6.11.

6.2.5 Impact Ionization in Ge at Low-temperature

The electric field in the detector determines the kinetic energy of charge carriers. It might be possible for these energetic charge carriers to produce more free charge carriers. The electric field required to produce the additional free charges (impact ionization) is ~ 15000 V/cm at around 79 K [135]. However, at mK temperature, impact ionization may occur from the interaction of charge carriers with the neutral impurities or crystal lattice as reported in the SuperCDMS publication [157]. At around LHe temperature there is the evidence of the formation of excited cluster dipoles as reported in this study. We have also observed the similar feature as of impact ionization. The increase in CCE for a USD-R09-02 detector as a function of time is shown in Figure 6.12. It was observed that the CCE increases with time at first up to several hundred seconds, then it becomes stabilized thereafter. The rate of gain/loss in energy due to impact

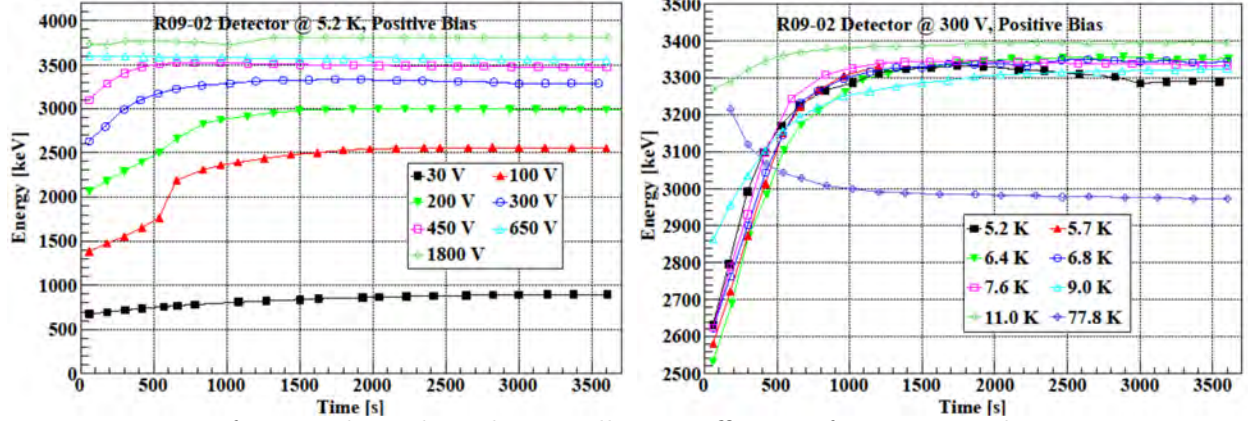


FIGURE 6.12: Left: time-dependent charge collection efficiency for a R09-02 detector at 5.2 K as a function of bias voltage; Right: time-dependent charge collection efficiency for a R09-02 detector at positive 300 V as a function of temperature.

ionization is given as [158];

$$\left(\frac{dE}{dt}\right)_i = (N_D - N_A)(2E/m^*)^{1/2}\sigma_i(E)(E_i) \quad (6.15)$$

where, $\sigma_i(E)$ is the cross-section for impact ionization to occur, m^* is the effective mass of the electron, $N_D - N_A$ is the net impurity concentration.

The following model was developed and used to explain the time-dependent charge collection efficiency;

$$P_0 + \frac{P_1}{P_2}[1 - \exp(-P_2t)] \quad (6.16)$$

where, P_0 , P_1 , P_2 are the fitting parameters which are related to charge collection efficiency at $t=0$, rate of energy released due to impact ionization, and inverse of time required to reach the plateau, respectively. The time-dependent CCE and the fitting model are shown in Figures 6.12 and 6.13.

Using the fitting parameters for 30 V, in Equation 6.15, the binding energy of the excited cluster dipole states was ~ 0.4 meV. The dependence of the scattering cross-section on the electric field should be considered for the calculation of binding energy. Such a detailed study was not pursued. The scattering cross-section for this calculation was assumed to be 5×10^{-13} cm² taking references from the SuperCDMS publications [157].

The time to reach the plateau is longer for the low voltage (30 V) compared to that of high

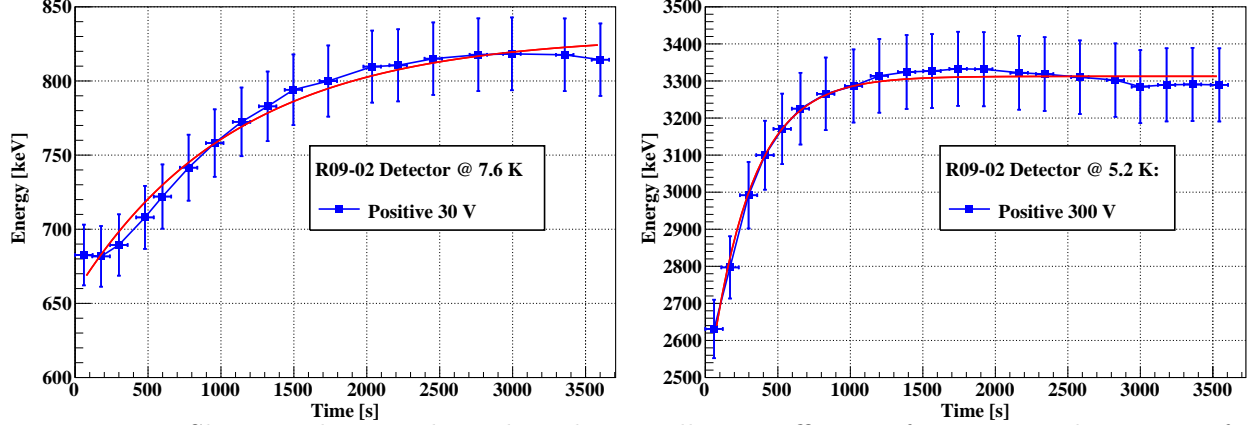


FIGURE 6.13: Shown is the time-dependent charge collection efficiency for a R09-02 detector. Left: positive 30 V at 7.6 K; Right: positive 300 V at 5.2 K

voltage (300 V) for a given temperature.

6.3 Charge Carrier Capture Cross-Section

The charge trapping was studied using the model developed by Melvin Lax [159]. This model was further extended by the Cryogenic Dark Matter Search (CDMS) collaborators. Charge trapping was studied in a fully depleted detector, hence, the cross-section calculation shown here refers to the deep trapping of impurities. The Onsager radius determines how large the effective volume of the sphere can be for the charge carrier to be bound with the impurity state. Outside the effective volume of the sphere, charge carriers are free and are not trapped anymore. The cross-section of the charge carrier capture cross-section is defined as [159];

$$\sigma_{eff}(E) = \frac{4\pi}{3} \frac{R_c^3}{\lambda_c(E)} \quad (6.17)$$

where $\sigma_{eff}(E)$, $\lambda_c(E)$, R_c are the effective capture cross section, the mean free scattering length, and critical radius, respectively. The mean free scattering length in Equation 6.17 is given as;

$$\lambda_c E = v_d \times \tau_c \quad (6.18)$$

where v_d and τ_c are the drift velocity of charge carriers and average scattering time of charge carriers within the effective sphere, respectively. The drift velocity depends on the mobility of

charge carriers and the electric field. Drift velocity increases linearly at first as a function of electric field and saturates for a high enough electric field, which can be expressed as;

$$v_d = \mu(E)E \quad (6.19)$$

where $\mu(E)$ is the mobility of charge carriers in a crystal, which depends on the type of charge carriers (electrons and holes) and the magnitude of the electric field. Hence the saturation drift velocity acquired by charge carriers can be given as;

$$v_{sat} = \mu(0)E_{sat} \quad (6.20)$$

where $\mu(0)$ is the mobility of charge carriers at zero electric field. It can be expressed in terms of Hall mobility ($\mu_0(H)$) through the following relation;

$$\mu(0) = \frac{\mu_0(H)}{r} \quad (6.21)$$

The magnitude of $\mu_0(H)$ and r are 36000 cm²/Vs (42000 cm²/Vs) and 0.83 (1.03), respectively for electrons (holes) for germanium at room temperature [160]. The empirical model of drift velocity and saturation drift velocity is stated as;

$$v_d = \frac{\mu(0)E}{1 + \frac{E}{v_{sat}}} \quad (6.22)$$

$$v_{sat} = \frac{v_{sat}^{300}}{1 - A_v + A_v \frac{T}{300}} \quad (6.23)$$

where v_{sat}^{300} and A_v are the constants and equal to 0.7×10^7 (0.63×10^7) and 0.55 (0.61) for electrons (holes), respectively. Using Equation 6.23, the saturation drift velocity calculated at 5.2 K for electrons and holes are 1.52×10^7 cm/s and 1.57×10^7 cm/s respectively. The mobility depends on temperature and the electric field. The field-dependent mobility is given as;

$$\mu(E) = \frac{\mu(0)E}{1 + \frac{\mu(0)E}{v_{sat}}} \quad (6.24)$$

Combining Equations 6.24 and 6.20, drift velocity can be expressed as;

$$v_d = \frac{\mu(0)E}{1 + \frac{\mu(0)E}{E_{sat}}} \quad (6.25)$$

The average scattering time for charge carriers with the impurity atoms is given as;

$$\tau_c = \frac{m^* \mu(E)}{e} \quad (6.26)$$

where m^* is the effective mass of charge carriers. Using drift velocity and scattering time, the scattering length for the charge carriers can be calculated. The mobility ($\mu(0)$) of electrons and holes at ~ 5.2 K was assumed to be 2×10^5 cm²/Vs and 1×10^5 cm²/Vs, respectively. The plot of mean scattering length and effective capture cross-section as a function of the electric field is shown in Figure 6.14. The effective capture cross-section was calculated using the information of critical radius and scattering length. The large difference in capture cross-section in the plot shown for 5.2 K suggests a similar charge trapping model to that of 77 K may not work, the cluster dipole states might be formed at this low temperature with a different charge trapping mechanism. In addition, the critical radius defined in this case is for the dipole states, hence the effective volume of the sphere (where charge carriers are considered to be trapped for the excited cluster dipole states) needs to be investigated.

The implication of charge trapping in a Ge detector at 77 K has been discussed in this Ref. [161].

6.4 Conclusions

Several planar Ge detectors were characterized in a PTR at \sim LHe temperature. The freeze-out of impurities \sim LHe temperature was observed experimentally. The spectral analysis using a ¹³⁷Cs and ²⁴¹Am source was performed. The significant charge trapping at LHe temperature may be attributed to the formation of excited cluster dipole states. Dipole formation was studied in both the n-type and p-type Ge detectors. Charge trapping length for the electrons and holes was obtained using the ²⁴¹Am data. In addition, the binding energy of the cluster dipoles was investigated using a charge trapping model. The binding energy was ~ 0.4 meV.

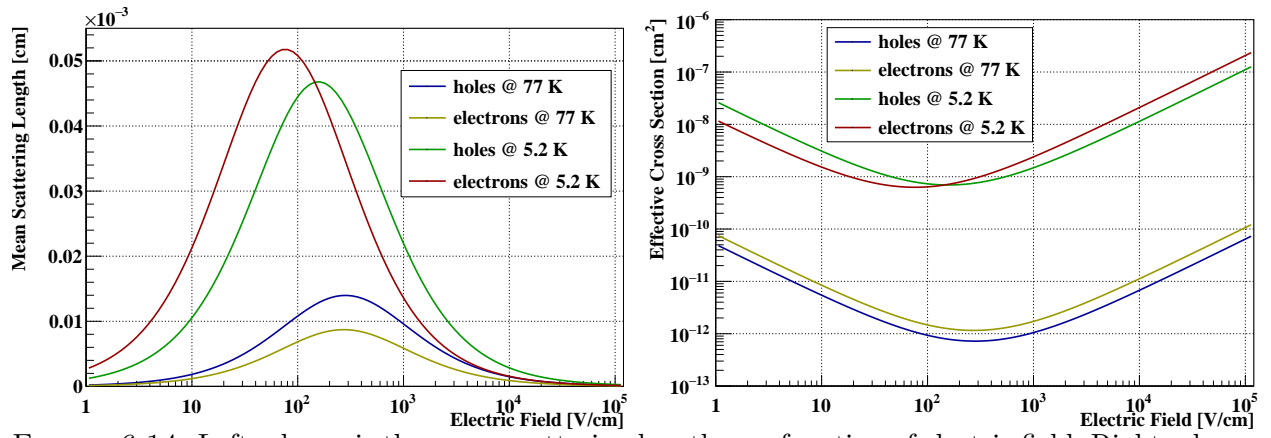


FIGURE 6.14: Left: shown is the mean scattering length as a function of electric field; Right: shown is the effective charge carrier capture cross-section as a function of electric field.

Summary and Perspectives

Ge detectors are widely used in rare event searches including dark matter and neutrinoless double beta ($0\nu\beta\beta$) decay searches. Some properties of the germanium (detector), particularly, high atomic mass (A), good energy and position resolution, and low energy threshold are ideal for such searches. Also, an advantage of a germanium (Ge) detector is it can act as both target and detector in particle detection. Investigating the Ge detector properties at a wide temperature is of further interest to enhance its applicability in dark matter and neutrino experiments. Ge is a good target to search for a low or intermediate mass WIMP-like dark matter. ^{76}Ge is predicted to undergo $0\nu\beta\beta$ decay. Ge-based experiments can also carry out $0\nu\beta\beta$ decay searches that can elucidate better the nature of neutrinos. Proper understanding of the detector response and enhancing the Ge detector abilities at a low energy regime can be crucial to improving the sensitivity of such rare-event searches.

In this dissertation, I present my work on the fabrication and characterization of amorphous Ge (a-Ge) contact Ge detectors at a wide temperature range.

- Ge has a wide range of applications including nuclear proliferation detection and rare-event searches. Growing a large-size single crystal of Ge and turning it into a detector is highly demanding for large-scale experiments. In this dissertation, I report the work I was involved in: procurement of single-crystalline Ge, its characterization, and the fabrication process to

form a-Ge contact in high purity Ge detector. It also discusses the challenges that exist in detector fabrication.

- In Chapter 4 of this dissertation, I discuss the work on the characterization of the Ge detector at liquid nitrogen (LN_2) and liquid argon (LAr) temperature. I fabricated about 15 Ge detectors (planar/guard-ring structure, point-contact) using the homegrown crystal at the University of South Dakota (USD). To investigate the detector performance at low temperatures, detectors were characterized in a LN_2 vacuum cryostat provided by the Lawrence Berkeley National Laboratory (LBNL). Current-Voltage, Capacitance-Voltage characteristics and energy spectroscopy measurements were carried out at a wide range of temperatures. Some of the detector properties were studied as a group and the findings were published in Journals [124, 136, 162]. Three detectors were brought to MPI for further characterization in cryogenic liquids (LAr and LN_2). For the first time, a-Ge contact Ge detector was directly immersed in those cryogenic liquids in Max-Planck-Institut (MPI) für Physik (MPI) in Munich and investigated. The results of this research have been already published in a Journal [42] and cover a significant part of Chapter 4 in this dissertation. a-Ge contact properties were tested in a Gerdalinen II cryostat. Detectors survived multiple thermal cycling without no sign of deteriorating the detector properties.
- In Chapter 5 of this dissertation, a-Ge barrier height measurements are presented. A new approach to calculating the inhomogeneity of the interface created by the a-Ge and crystalline Ge surface is introduced. Bulk leakage current from three guard-ring style Ge detectors was measured at a wide temperature range and this data was used to find out the inhomogeneity level of the interface. Though the recipe and techniques to fabricate the germanium detector are the same, there is a difference in the level of inhomogeneity for the three detectors suggests that the fabrication process can be optimized in order to achieve a homogeneous interface. The results of this analysis have been published in a Journal [163].
- In Chapter 6, a model is introduced to explain the charge trapping at liquid helium temperature. There are only a few studies of Ge properties at around liquid helium (LHe) temperature.

In our work, we characterize several detectors in a Pulse Tube Refrigerator (PTR) developed by our group. The freeze-out temperature is determined for the Ge crystal. Impurities start to freeze-out at around 11 K and are completely frozen at less than ~ 6.4 K. In addition, the spectral analysis was performed using the radioactive sources ^{241}Am and ^{137}Cs at a temperature range of 5.2 - 80 K. It was observed that the Ge detector turns into an ideal capacitor without the application of bias voltage at around 5.2 K, however, to achieve a good charge collection efficiency detector needs to operate at a significantly large voltage. Similar findings were published by other researchers [164], however, no clear physics explanation was given. A cluster dipole formation model developed by Mei was applied to explain such behavior. The requirement for the large bias voltage at low temperature was attributed to the formation of cluster dipole states. A paper has been published on these findings by our group [156].

Several improvements can be done in a future study. The process parameters can be optimized in order to achieve a more homogeneous interface between a-Ge and crystalline Ge surfaces. Barrier height can be optimized and leakage current minimized. Large-size detector with a-Ge contacts can be fabricated to test the robustness of a-Ge contact. The spectral analysis of energy resolution of the detector can be made at around LHe temperature with optimized electronic noise. With a guard-ring structure detector, both bulk leakage current and surface leakage current characteristics can be studied. A study of leakage current at a wide temperature range might help to understand the surface properties of the detector better. In the future, freeze-out temperature dependence on the impurity concentration of the crystal can be studied. Also, cluster dipole formation can be investigated and its relationship with the impurity concentration of the crystal and bias voltage. Further, time-dependent charge collection efficiency dependence on the net impurity concentration of the crystal can be studied. From our work, a net impurity concentration greater than the order of a few times 10^{10} cm^{-3} is needed to observe such phenomena. Another avenue of study can be a study based on the pulse shape analysis at around LHe temperature. This can also help develop a model to find out the mobility of charge carrier dependence on temperature. Currently, available mobility data have large uncertainties at lower temperatures.

Bibliography

- [1] C. Lederer and V. Shirley, Table of Isotopes, 7th Ed., John Wiley & Sons Inc., NY (1978).
- [2] G. Yang, Y. Guan, F. Jian, M. Wagner, H. Mei, G. Wang, S. Howard, D. Mei, A. Nelson, J. Marshal, *et al.*, in *Journal of Physics: Conference Series*, Vol. 606 (IOP Publishing, 2015) p. 012014.
- [3] G. Wang, Y. Sun, G. Yang, W. Xiang, Y. Guan, D. Mei, C. Keller, and Y.-D. Chan, *Journal of Crystal Growth* **352**, 27 (2012).
- [4] G. Wang, M. Amman, H. Mei, D. Mei, K. Irmscher, Y. Guan, and G. Yang, *Materials Science in Semiconductor Processing* **39**, 54 (2015).
- [5] G. Wang, H. Mei, D. Mei, Y. Guan, and G. Yang, in *Journal of Physics: Conference Series*, Vol. 606 (IOP Publishing, 2015) p. 012012.
- [6] S. Sakaguchi and S.-i. Todoroki, *Applied optics* **36**, 6809 (1997).
- [7] C. Kittel, *Introduction to solid state physics*, John Wiley & Sons Inc., Sixth edition, (New York, 1986) (2005).
- [8] M. L. Handbook Series on Semiconductor Parameters, S. Rumyantsev, and M. S. Shur (1996).
- [9] E. Pell, *Journal of Applied Physics* **31**, 291 (1960).
- [10] D. Freck and J. Wakefield, *Nature* **193**, 669 (1962).
- [11] R. N. Hall and T. J. Soltys, *IEEE Transactions on Nuclear Science* **18**, 160 (1971).

- [12] K. Benourhazi and J. Ponpon, Nuclear Instruments and Methods in Physics Research Section B: Beam Interactions with Materials and Atoms **71**, 406 (1992).
- [13] R. Grigorovici, N. Croitoru, A. Devenyi, and E. Teleman, Proceedings of the Seventh International Conference on the Physics of Semiconductors, Paris, France, July , 423 (1964).
- [14] J. England and V. W. Hammer, Nuclear Instruments and Methods **96**, 81 (1971).
- [15] W. L. Hansen and E. E. Haller, IEEE Trans. Nucl. Sci. **24**, 61 (1977).
- [16] P. Luke, C. Cork, N. Madden, C. Rossington, and M. Wesela, IEEE Trans. Nucl. Sci. **39**, 590 (1992).
- [17] P. Luke, R. Pehl, and F. Dilmanian, IEEE Trans. Nucl. Sci. **41**, 976 (1994).
- [18] P. Luke, M. Amman, B. Philips, W. Johnson, and R. Kroeger, IEEE Trans. Nucl. Sci. **47**, 1360 (2000).
- [19] M. S. Amman and P. N. Luke, in *Hard X-Ray, Gamma-Ray, and Neutron Detector Physics II*, Vol. 4141 (International Society for Optics and Photonics, 2000) pp. 144–156.
- [20] M. Amman and P. Luke, Nuclear Instruments and Methods in Physics Research Section A: Accelerators, Spectrometers, Detectors and Associated Equipment **452**, 155 (2000).
- [21] P. N. Luke, C. S. Tindall, and M. Amman, IEEE Transactions on Nuclear Science **56**, 808 (2009).
- [22] M. Amman, A. Priest, P. N. Luke, S. Asztalos, K. Sabourov, and K. Vetter, IEEE Transactions on Nuclear Science **60**, 1213 (2013).
- [23] Q. Looker, M. Amman, and K. Vetter, Nucl. Instrum. Meth. A **777**, 138 (2015).
- [24] M. Amman, “Optimization of amorphous germanium electrical contacts and surface coatings on high purity germanium radiation detectors,” (2018), arXiv:1809.03046.
- [25] M. Amman, arXiv preprint arXiv:2006.05471 (2020).

- [26] R. H. Pehl, *Phys. Today* **30N11**, 50 (1977).
- [27] A. Tavendale, *IEEE Trans. Nucl. Sci.* **12**, 255 (1965).
- [28] A. Muggleton, *J. Phys. E* **5**, 390 (1972).
- [29] M. Agostini, A. Bakalyarov, M. Balata, I. Barabanov, L. Baudis, C. Bauer, E. Bellotti, S. Belogurov, A. Bettini, L. Bezrukov, *et al.*, in *Journal of Physics: Conference Series*, Vol. 1342 (IOP Publishing, 2020) p. 012005.
- [30] S. Alvis, I. Arnquist, F. Avignone III, A. Barabash, C. Barton, V. Basu, F. Bertrand, B. Bos, M. Busch, M. Buuck, *et al.*, *Phys. Rev. C* **100**, 025501 (2019).
- [31] N. Abgrall *et al.*, in *AIP Conf. Proc.*, Vol. 1894 (2017) p. 020027.
- [32] C. E. Aalseth, P. S. Barbeau, J. Colaresi, J. Collar, J. D. Leon, J. E. Fast, N. Fields, T. W. Hossbach, A. Knecht, M. S. Kos, *et al.*, *Phys. Rev. D* **88**, 012002 (2013).
- [33] Y. Wang, Q. Yue, S. Liu, K. Kang, Y. Li, H. An, J. Chang, J. Chen, Y. Chen, J. Cheng, *et al.*, *Physical Review D* **101**, 052003 (2020).
- [34] R. Agnese, T. Aramaki, I. Arnquist, W. Baker, D. Balakishiyeva, S. Banik, D. Barker, R. B. Thakur, D. Bauer, T. Binder, *et al.*, *Physical review letters* **120**, 061802 (2018).
- [35] D.-M. Mei, G.-J. Wang, H. Mei, G. Yang, J. Liu, M. Wagner, R. Panth, K. Kooi, Y.-Y. Yang, and W.-Z. Wei, *The European Physical Journal C* **78**, 1 (2018).
- [36] C. E. Aalseth, M. Amman, F. Avignone III, H. O. Back, A. S. Barabash, P. Barbeau, M. Bergevin, F. Bertrand, M. Boswell, V. Brudanin, *et al.*, *Nuclear Instruments and Methods in Physics Research Section A: Accelerators, Spectrometers, Detectors and Associated Equipment* **652**, 692 (2011).
- [37] B. H. Hasegawa, B. Stebler, B. K. Rutt, A. Martinez, E. L. Gingold, C. S. Barker, K. G. Faulkner, C. E. Cann, and D. P. Boyd, *Medical physics* **18**, 900 (1991).

- [38] J. Uyttenhove, in *Radioactivity in the environment*, Vol. 7 (Elsevier, 2005) pp. 45–55.
- [39] S. Stave, in *Journal of Physics: Conference Series*, Vol. 606 (IOP Publishing, 2015) p. 012018.
- [40] N. Demir and Z. N. Kuluöztürk, *Nuclear Engineering and Technology* **53**, 3759 (2021).
- [41] Y. Eisen and A. Shor, *Journal of crystal growth* **184**, 1302 (1998).
- [42] R. Panth, J. Liu, I. Abt, X. Liu, O. Schulz, W.-Z. Wei, H. Mei, D.-M. Mei, and G.-J. Wang, *The European Physical Journal C* **80**, 1 (2020).
- [43] S. Paschalis, I. Lee, A. Macchiavelli, C. Campbell, M. Cromaz, S. Gros, J. Pavan, J. Qian, R. Clark, H. Crawford, *et al.*, *Nuclear Instruments and Methods in Physics Research Section A: Accelerators, Spectrometers, Detectors and Associated Equipment* **709**, 44 (2013).
- [44] W. Korten, A. Atac, D. Beaumel, P. Bednarczyk, M. Bentley, G. Benzoni, A. Boston, A. Bracco, J. Cederkäll, B. Cederwall, *et al.*, *The European Physical Journal A* **56**, 1 (2020).
- [45] L. C. Johnson, O. Ovchinnikov, S. Shokouhi, and T. E. Peterson, *IEEE transactions on nuclear science* **62**, 2036 (2015).
- [46] N. Fourches, M. Zielińska, and G. Charles, in *Use of Gamma Radiation Techniques in Peaceful Applications* (IntechOpen, 2019) p. 67.
- [47] P. Barton, M. Amman, R. Martin, and K. Vetter, *Nuclear Instruments and Methods in Physics Research Section A: Accelerators, Spectrometers, Detectors and Associated Equipment* **812**, 17 (2016).
- [48] N. Abgrall, I. Abt, M. Agostini, A. Alexander, C. Andreoiu, G. Araujo, F. Avignone III, W. Bae, A. Bakalyarov, M. Balata, *et al.*, arXiv preprint arXiv:2107.11462 (2021).
- [49] M. Albakry, I. Alkhatib, D. Amaral, T. Aralis, T. Aramaki, I. Arnquist, I. A. Langroudy, E. Azadbakht, S. Banik, C. Bathurst, *et al.*, *Physical Review D* **105**, 112006 (2022).
- [50] Z. Liu, Q. Yue, L. Yang, K. Kang, Y. Li, H. Wong, M. Agartioglu, H. An, J. Chang, J. Chen, *et al.*, *Physical Review Letters* **123**, 161301 (2019).

- [51] E. Armengaud, C. Augier, A. Benoît, A. Benoit, L. Bergé, J. Billard, A. Broniatowski, P. Camus, A. Cazes, M. Chapellier, *et al.*, Physical Review D **99**, 082003 (2019).
- [52] B. Pontecorvo, Zh. Eksp. Teor. Fiz. **34**, 247 (1957).
- [53] M. Goeppert-Mayer, Physical Review **48**, 512 (1935).
- [54] E. Majorana and L. Maiani, in *Ettore Majorana Scientific Papers* (Springer, 2006) pp. 201–233.
- [55] W. H. Furry, Physical Review **56**, 1184 (1939).
- [56] A. Giuliani and A. Poves, Advances in High Energy Physics **2012** (2012).
- [57] B. J. Mount, M. Redshaw, and E. G. Myers, Physical Review C **81**, 032501 (2010).
- [58] O. Panella, M. Cannoni, C. Carimalo, and Y. Srivastava, Phys. Rev. D **65**, 035005 (2002).
- [59] F. Almeida Jr, Y. Coutinho, J. M. Simoes, and M. Do Vale, Phys. Rev. D **62**, 075004 (2000).
- [60] A. Das, N. Okada, and D. Raut, Eur. Phys. J. C **78**, 696 (2018).
- [61] W. Rodejohann, J. Phys. G **28**, 1477 (2002).
- [62] T. Asaka, S. Blanchet, and M. Shaposhnikov, Phys. Lett. B **631**, 151 (2005).
- [63] T. Asaka and M. Shaposhnikov, Phys. Lett. B **620**, 17 (2005).
- [64] C. S. Fong, E. Nardi, and A. Riotto, Adv. High Ene. Phys. **2012**, 158303 (2012).
- [65] S. Davidson and A. Ibarra, Phys. Lett. B **535**, 25 (2002).
- [66] R. Foot, H. Lew, X.-G. He, and G. C. Joshi, Zeit. Phys. C **44**, 441 (1989).
- [67] R. N. Mohapatra and G. Senjanović, Phys. Rev. Lett. **44**, 912 (1980).
- [68] Y. Cai, T. Han, T. Li, and R. Ruiz, Front. Phys. **6**, 40 (2018).
- [69] M. J. Dolinski, A. W. Poon, and W. Rodejohann, Ann. Rev. Nucl. Part. Sci. **69**, 219 (2019).

- [70] A. Giuliani, *Acta Phys. Polon.* **41**, 1447 (2010).
- [71] I. Nutini, D. Adams, C. Alduino, K. Alfonso, F. Avignone III, O. Azzolini, G. Bari, F. Bellini, G. Benato, M. Beretta, *et al.*, *International Journal of Modern Physics A* **37**, 2240014 (2022).
- [72] V. Lozza, S. Collaboration, *et al.*, *Nuclear and particle physics proceedings* **273**, 1836 (2016).
- [73] Y. Gando, A. Gando, T. Hachiya, S. Hayashida, K. Hosokawa, H. Ikeda, T. Mitsui, T. Nakada, S. Obara, H. Ozaki, *et al.*, *Journal of Instrumentation* **16**, P08023 (2021).
- [74] G. Adhikari, S. Al Kharusi, E. Angelico, G. Anton, I. Arnquist, I. Badhrees, J. Bane, V. Belov, E. Bernard, T. Bhatta, *et al.*, *Journal of Physics G: Nuclear and Particle Physics* **49**, 015104 (2021).
- [75] C. Romo-Luque, arXiv preprint arXiv:2201.10907 (2022).
- [76] M. Agostini, A. Bakalyarov, M. Balata, I. Barabanov, L. Baudis, C. Bauer, E. Bellotti, S. Belogurov, A. Bettini, L. Bezrukov, *et al.*, *Phys. Rev. Lett.* **120**, 132503 (2018).
- [77] M. Agostini, A. Bakalyarov, M. Balata, I. Barabanov, L. Baudis, C. Bauer, E. Bellotti, S. Belogurov, S. Belyaev, G. Benato, *et al.*, *Eur. Phys. J. C* **78**, 388 (2018).
- [78] Gerda Collaboration, M. Agostini, *et al.*, *Science* **365**, 1445 (2019).
- [79] M. Agostini, G. Araujo, A. Bakalyarov, M. Balata, I. Barabanov, L. Baudis, C. Bauer, E. Bellotti, S. Belogurov, A. Bettini, *et al.*, *The European Physical Journal C* **81**, 1 (2021).
- [80] I. Arnquist, F. Avignone, A. Barabash, C. Barton, F. Bertrand, E. Blalock, B. Bos, M. Busch, M. Buuck, T. Caldwell, *et al.*, *The European Physical Journal C* **82**, 1 (2022).
- [81] C. Aalseth, N. Abgrall, E. Aguayo, S. Alvis, M. Amman, I. Arnquist, F. Avignone III, H. Back, A. Barabash, P. Barbeau, *et al.*, *Phys. Rev. Lett.* **120**, 132502 (2018).
- [82] Majorana Collaboration, S. I. Alvis, *et al.*, *Phys. Rev. C* **100**, 025501 (2019).

- [83] G. Giovanetti, *P-type point contact germanium detectors and their application in rare-event searches*, Ph.D. thesis, University of North Carolina, Chapel Hill (2015).
- [84] S. Mertens, A. Hegai, D. Radford, N. Abgrall, Y.-D. Chan, R. Martin, A. Poon, and C. Schmitt, *Nucl. Instrum. Meth. A* **921**, 81 (2019).
- [85] D. Barrientos, A. Boston, H. Boston, B. Quintana, I. Sagrado, C. Unsworth, S. Moon, and J. Cresswell, *Nucl. Instrum. Meth. A* **648**, S228 (2011).
- [86] M. Agostini, E. Bellotti, R. Brugnera, C. Cattadori, A. D’Andragora, A. Di Vacri, A. Garfagnini, M. Laubenstein, L. Pandola, and C. Ur, *J. Instrum.* **6**, P04005 (2011).
- [87] A. de Kock, F. Beeftink, and K. Schell, *Appl. Phys. Lett.* **20**, 81 (1972).
- [88] Padraic Seamus Finnerty, *A Direct Dark Matter Search with the Majorana Low-Background Broad Energy Germanium Detector*, Ph.D. thesis, University of North Carolina, Chapel Hill (2013).
- [89] E. Aguayo *et al.*, *Nucl. Instrum. Meth. A* **701**, 176 (2013).
- [90] H. Jiang *et al.*, *Chin. Phys. C* **40**, 096001 (2016).
- [91] A. Lubashevskiy, M. Agostini, D. Budjáš, A. Gangapshev, K. Gusev, M. Heisel, A. Klimenko, A. Lazzaro, B. Lehnert, K. Pelczar, *et al.*, *The European Physical Journal C* **78**, 1 (2018).
- [92] C. Zhang and D.-M. Mei, *Astroparticle Physics*, 102733 (2022).
- [93] J. Llacer, E. Haller, and R. Cordi, *IEEE Trans. Nucl. Sci.* **24**, 53 (1977).
- [94] T. Alexander, H. O. Back, W. Bonivento, M. Boulay, P. Collon, Z. Feng, M. Foxe, P. G. Abia, P. Giampa, C. Jackson, *et al.*, “The Low-Radioactivity Underground Argon Workshop: A Workshop Synopsis,” (2019), arXiv:1901.10108.
- [95] J.-L. Chiu, S. Boggs, H.-K. Chang, J. Tomsick, A. Zoglauer, M. Amman, Y.-H. Chang, Y. Chou, P. Jean, C. Kierans, *et al.*, *Nucl. Instrum. Meth. A* **784**, 359 (2015).

- [96] C. A. Kierans, S. E. Boggs, *et al.*, “The 2016 super pressure balloon flight of the compton spectrometer and imager,” (2017), arXiv:1701.05558.
- [97] F. Zwicky, *Helvetica physica acta* **6**, 110 (1933).
- [98] F. Zwicky, *The Astrophysical Journal* **86**, 217 (1937).
- [99] V. C. Rubin, *Scientific American* **248**, 96 (1983).
- [100] D. Clowe, M. Bradač, A. H. Gonzalez, M. Markevitch, S. W. Randall, C. Jones, and D. Zaritsky, *The Astrophysical Journal* **648**, L109 (2006).
- [101] M. Bradač, D. Clowe, A. H. Gonzalez, P. Marshall, W. Forman, C. Jones, M. Markevitch, S. Randall, T. Schrabback, and D. Zaritsky, *The Astrophysical Journal* **652**, 937 (2006).
- [102] P. A. Ade, N. Aghanim, M. Alves, C. Armitage-Caplan, M. Arnaud, M. Ashdown, F. Atriobarandela, J. Aumont, H. Aussel, C. Baccigalupi, *et al.*, *Astronomy & Astrophysics* **571**, A1 (2014).
- [103] J. C. Mather, E. Cheng, D. A. Cottingham, R. Eplee Jr, D. J. Fixsen, T. Hewagama, R. Isaacman, K. Jensen, S. S. Meyer, P. D. Noerdlinger, *et al.*, *The Astrophysical Journal* **420**, 439 (1994).
- [104] R. J. Gaitskell, *Annual Review of Nuclear and Particle Science* **54**, 315 (2004).
- [105] P. Cushman, C. Galbiati, D. McKinsey, H. Robertson, T. Tait, D. Bauer, A. Borgland, B. Cabrera, F. Calaprice, J. Cooley, *et al.*, arXiv preprint arXiv:1310.8327 (2013).
- [106] S. Böser, C. Buck, C. Giunti, J. Lesgourgues, L. Ludhova, S. Mertens, A. Schukraft, and M. Wurm, *Progress in particle and nuclear physics* **111**, 103736 (2020).
- [107] K. Abazajian, G. M. Fuller, and M. Patel, *Physical Review D* **64**, 023501 (2001).
- [108] R. D. Peccei and H. R. Quinn, *Physical Review D* **16**, 1791 (1977).
- [109] F. Wilczek, *Physical Review Letters* **40**, 279 (1978).

- [110] S. Weinberg, *Physical Review Letters* **40**, 223 (1978).
- [111] R. Essig, J. Mardon, and T. Volansky, *Physical Review D* **85**, 076007 (2012).
- [112] D. R. Tovey, R. Gaitskell, P. Gondolo, Y. Ramachers, and L. Roszkowski, *Physics Letters B* **488**, 17 (2000).
- [113] J. Aalbers, D. Akerib, C. Akerlof, A. Al Musalhi, F. Alder, A. Alqahtani, S. Alsum, C. Amarasinghe, A. Ames, T. Anderson, *et al.*, arXiv preprint arXiv:2207.03764 (2022).
- [114] R. Essig, *Physics* **13**, 172 (2020).
- [115] Y. Chen, M.-Y. Cui, J. Shu, X. Xue, G.-W. Yuan, and Q. Yuan, *Journal of High Energy Physics* **2021**, 1 (2021).
- [116] A. Abdelhameed, G. Angloher, P. Bauer, A. Bento, E. Bertoldo, C. Bucci, L. Canonica, A. D’Addabbo, X. Defay, S. Di Lorenzo, *et al.*, *The European Physical Journal C* **79**, 1 (2019).
- [117] A. Castoldi, C. Guazzoni, S. Maffessanti, and T. Krings, in *2018 IEEE Nuclear Science Symposium and Medical Imaging Conference Proceedings (NSS/MIC)* (IEEE, 2018) pp. 1–4.
- [118] H. Bonet, A. Bonhomme, C. Buck, K. Fülber, J. Hakenmüller, G. Heusser, T. Hugle, J. Legras, M. Lindner, W. Maneschg, *et al.*, *The European Physical Journal C* **81**, 1 (2021).
- [119] J. Colaresi, J. Collar, T. Hossbach, A. Kavner, C. Lewis, A. Robinson, and K. Yocum, *Physical Review D* **104**, 072003 (2021).
- [120] J. P. Wright, L. Harkness-Brennan, A. Boston, D. Judson, M. Labiche, P. Nolan, R. Page, F. Pearce, D. C. Radford, J. Simpson, *et al.*, *Nuclear Instruments and Methods in Physics Research Section A: Accelerators, Spectrometers, Detectors and Associated Equipment* **892**, 84 (2018).
- [121] M. Raut, H. Mei, D. Mei, S. Bhattarai, W. Wei, R. Panth, P. Acharya, and G. Wang, *JINST* **15**, T10010 (2020), arXiv:2002.07706 [physics.ins-det] .

- [122] M. H. Brodsky and G. H. Döhler, *Crit. Rev. Sol. Stat. Mater. Sci.* **5**, 591 (1975).
- [123] T. Shutt, J. Emes, E. E. Haller, J. Hellmig, B. Sadoulet, D. Seitz, B. A. Young, and S. White, *Nuclear Instruments and Methods in Physics Research Section A: Accelerators, Spectrometers, Detectors and Associated Equipment* **444**, 340 (2000).
- [124] S. Bhattarai, R. Panth, W.-Z. Wei, H. Mei, D.-M. Mei, M.-S. Raut, P. Acharya, and G.-J. Wang, *The European Physical Journal C* **80**, 1 (2020).
- [125] W.-Z. Wei, X.-H. Meng, Y.-Y. Li, J. Liu, G.-J. Wang, H. Mei, G. Yang, D.-M. Mei, and C. Zhang, *J. Instrum.* **13**, P12026 (2018).
- [126] W.-Z. Wei, R. Panth, J. Liu, H. Mei, D.-M. Mei, and G.-J. Wang, “The Impact of the Charge Barrier Height on Germanium (Ge) Detectors with Amorphous-Ge Contacts for Light Dark Matter Searches,” (2020), arXiv: 2002.04462.
- [127] I. Abt, A. Caldwell, D. Lenz, J. Janicsko, J. Liu, X. Liu, B. Majorovits, and F. Stelzer, *J. Phys. Conf. Series* **203**, 012135 (2010).
- [128] S. M. Sze and K. K. Ng, *Physics of Semiconductor Devices* (John Wiley & Sons, Inc., 1981).
- [129] X.-H. Meng, G.-J. Wang, M.-D. Wagner, H. Mei, W.-Z. Wei, J. Liu, G. Yang, and D.-M. Mei, *J. Instrum.* **14**, P02019 (2019).
- [130] G. H. Döhler and M. H. Brodsky, *Proc. Inter. Conf. Tetrahedrally Bonded Amorphous Semiconductors*, 351 (1974).
- [131] M. H. Brodsky, G. H. Döhler, and P. J. Steinhardt, *Phys. Stat. Sol.* **72**, 761 (1975).
- [132] E. Hull and R. Pehl, *Nucl. Instr. and Meth. A* **538**, 651 (2005).
- [133] M. Barnabe Heider, C. Cattadori, O. Chkvorets, A. Di Vacri, K. Gusev, S. Schönert, and M. Shirchenko, in *IEEE Nucl. Sci. Symp. Med. Imag. Conf., 16th Inter. Workshop on Room-Temp. Semicond. X-Ray and Gamma-Ray Detectors* (2008) pp. 3513–3516, arXiv:0812.1907.

- [134] D. Palioselitis, G. collaboration, *et al.*, in *J. Phys. Conf. Ser.*, Vol. 606 (2015) p. 012007.
- [135] W.-Z. Wei, H. Mei, K. Kooi, D.-M. Mei, J. Liu, J.-C. Li, R. Panth, and G.-J. Wang, *The European Physical Journal C* **82**, 1 (2022).
- [136] W. Wei, R. Panth, J. Liu, H. Mei, D. Mei, and G. Wang, *European Physical Journal C* **80**, 1 (2020).
- [137] S. Tripathi and M. Sharma, *Journal of Applied Physics* **111**, 074513 (2012).
- [138] T. Zhang, C. Raynaud, and D. Planson, *The European Physical Journal Applied Physics* **85**, 10102 (2019).
- [139] H. Sheoran, B. R. Tak, N. Manikanthababu, and R. Singh, *ECS Journal of Solid State Science and Technology* (2020).
- [140] R. Nouchi, *Journal of Applied Physics* **116**, 184505 (2014).
- [141] A. Di Bartolomeo, F. Giubileo, G. Luongo, L. Iemmo, N. Martucciello, G. Niu, M. Fraschke, O. Skibitzki, T. Schroeder, and G. Lupina, *2D Materials* **4**, 015024 (2016).
- [142] S. Zeyrek, M. Bülbül, Ş. Altındal, M. Baykul, and H. Yüzer, *Brazilian Journal of Physics* **38**, 591 (2008).
- [143] S. Toumi, A. Ferhat-Hamida, L. Boussouar, A. Sellai, Z. Ouennoughi, and H. Ryssel, *Micro-electronic Engineering* **86**, 303 (2009).
- [144] S. Sil, R. Jana, A. Biswas, D. Das, A. Dey, J. Datta, D. Sanyal, and P. P. Ray, *IEEE Transactions on Electron Devices* **67**, 2082 (2020).
- [145] J. Nicholls, S. Dimitrijević, P. Tanner, and J. Han, *Scientific reports* **9**, 1 (2019).
- [146] W. C. Huang, T.-C. Lin, C.-T. Horng, and C.-C. Chen, *Microelectronic engineering* **107**, 200 (2013).

- [147] K. Zeghdar, L. Dehimi, A. Saadoune, and N. Sengouga, *Journal of Semiconductors* **36**, 124002 (2015).
- [148] S. Karboyan, J.-G. Tartarin, and B. Lambert, in *2013 European Microwave Integrated Circuit Conference* (IEEE, 2013) pp. 240–243.
- [149] J. H. Werner and H. H. Güttler, *Journal of applied physics* **69**, 1522 (1991).
- [150] W. Mtangi, F. Auret, C. Nyamhere, P. J. Van Rensburg, M. Diale, and A. Chawanda, *Physica B: Condensed Matter* **404**, 1092 (2009).
- [151] H. Spieler, *Semiconductor detector systems*, Vol. 12 (Oxford university press, 2005).
- [152] J. Li, J. Liu, and K. Kooi, *The European Physical Journal C* **80**, 1 (2020).
- [153] W. Shockley, *Journal of applied physics* **9**, 635 (1938).
- [154] S. Ramo, *Proceedings of the IRE* **27**, 584 (1939).
- [155] A. Rose, *Physical Review* **97**, 1538 (1955).
- [156] D.-M. Mei, R. Panth, K. Kooi, H. Mei, S. Bhattarai, M. Raut, P. Acharya, and G.-J. Wang, *AIP Advances* **12**, 065113 (2022), <https://doi.org/10.1063/5.0094194> .
- [157] K. M. Sundqvist, *Carrier transport and related effects in detectors of the cryogenic dark matter search* (University of California, Berkeley, 2012).
- [158] A. Zylbersztein, *Physical Review* **127**, 744 (1962).
- [159] M. Lax, *Physical Review* **119**, 1502 (1960).
- [160] S. Wagner *et al.*, *IEEE Std 1160* **1993**, 1 (1993).
- [161] D. Mei, M. R. Bharadwaj, W. Wei, R. Panth, J. Liu, H. Mei, Y. Li, P. Acharya, S. Bhattarai, K. Kooi, *et al.*, *Journal of Physics G: Nuclear and Particle Physics* (2020).

- [162] D.-M. Mei, R. Mukund, W.-Z. Wei, R. Panth, J. Liu, H. Mei, Y.-Y. Li, P. Acharya, S. Bhattarai, K. Kooi, *et al.*, “Impact of charge trapping on the energy resolution of ge detectors for rare-event physics searches,” (2019), arXiv:1909.05806.
- [163] R. Panth, W. Wei, D. Mei, J. Liu, S. Bhattarai, H. Mei, M. Raut, P. Acharya, K. Kooi, and G. Wang, Nuclear Instruments and Methods in Physics Research. Section A, Accelerators, Spectrometers, Detectors and Associated Equipment **1035** (2022).
- [164] D. Vénos, A. Van Assche-Van Geert, N. Severijns, D. Srnka, and D. Zákoucký, Nuclear Instruments and Methods in Physics Research Section A: Accelerators, Spectrometers, Detectors and Associated Equipment **454**, 403 (2000).